COPPE
Instituto Alberto Luiz Coimbra de
Pós-Graduação e Pesquisa de Engenharia
UFRJ

MODULATIONAL INSTABILITY ON NONLINEAR WATER WAVES: EXPERIMENTAL STUDY

Uggo Ferreira de Pinho

Tese de Doutorado apresentada ao Programa de Pós-graduação em Engenharia Oceânica, COPPE, da Universidade Federal do Rio de Janeiro, como parte dos requisitos necessários à obtenção do título de Doutor em Engenharia Oceânica.

Orientadores: Nelson Violante-Carvalho
Wilton Zumpichiatti Arruda
Alexander Babanin

Rio de Janeiro
Junho de 2018

MODULATIONAL INSTABILITY ON NONLINEAR WATER WAVES: EXPERIMENTAL STUDY

Uggo Ferreira de Pinho

TESE SUBMETIDA AO CORPO DOCENTE DO INSTITUTO ALBERTO LUIZ COIMBRA DE PÓS-GRADUAÇÃO E PESQUISA DE ENGENHARIA (COPPE) DA UNIVERSIDADE FEDERAL DO RIO DE JANEIRO COMO PARTE DOS REQUISITOS NECESSÁRIOS PARA A OBTENÇÃO DO GRAU DE DOUTOR EM CIÊNCIAS EM ENGENHARIA OCEÂNICA.

Examinada por:

Prof. Nelson Violante-Carvalho, Ph.D.

Prof. Wilton Zumpichiatti Arruda, Ph.D.

Prof. Alexander Babanin, Ph.D.

Prof. Carlos Eduardo Parente Ribeiro, D.Sc.

Prof. Leandro Farina, Ph.D.

Prof. Roger Matsumoto Moreira, Ph.D.

Prof. Rogério Neder Candella, D.Sc.

Prof. Victor de Amorim D'Ávila, D.Sc.

RIO DE JANEIRO, RJ – BRASIL
JUNHO DE 2018

Pinho, Uggo Ferreira de

Modulational Instability on Nonlinear Water Waves: Experimental study/Uggo Ferreira de Pinho. – Rio de Janeiro: UFRJ/COPPE, 2018.

XIX, 105 p.: il.; 29, 7cm.

Orientadores: Nelson Violante-Carvalho
Wilton Zumpichiatti Arruda
Alexander Babanin

Tese (doutorado) – UFRJ/COPPE/Programa de Engenharia Oceânica, 2018.

Referncias Bibliogrficas: p. 75 – 78.

1. Modulation Instability. 2. Nonlinear Waves. 3. Gravity Waves. I. Violante-Carvalho, Nelson *et al.* II. Universidade Federal do Rio de Janeiro, COPPE, Programa de Engenharia Oceânica. III. Título.

‘Experiment is the only means of knowledge at our disposal. Everything else is poetry, imagination.’

— *Max Planck*

‘True Laws of Nature cannot be linear.’

— *Albert Einstein*

Acknowledgements

Firstly and foremost, I would like to express my sincere gratitude to my advisor Prof. Nelson Violante-Carvalho, my co-advisors Wilton Zumpichiatti Arruda and Alexander V. Babanin, for the continuous support, for their patience, motivation, and knowledge and for the meticulous suggestions and astute criticism. I was very lucky for having them as supervisors for my Ph.D study. A special sincere gratitude to Prof. Alexander V. Babanin, for introducing me to the theme of this thesis and for whom I am very grateful in my career as physical oceanographer.

I am also very grateful to Prof. Carlos Eduardo Parente and Prof. Victor de Amorim D'Ávila for the very valuable insightful comments, encouragement and suggestions to the present research and for the immense contribution in my professional life in so many years of mentoring and friendship.

I would like also to thank my thesis committee members: Prof. Leandro Farina, Prof. Roger Matsumoto Moreira, Dr. Rogério Neder Candella, Prof. Victor D'Avila e Prof. Carlos Parente for kindly accepting the invitation to be part of my examiner committee.

I thank also Prof. Paulo de Tarso Themistocles Esperança and his team at LabOceano, UFRJ. Prof. Paulo have shown great competence and professionalism managing LabOceano and making possible to effectively conduct the complex tests presented in this thesis providing reliable data sets.

Faculty of the Program of Naval and Oceanic Engineering - PENO/-COPPE/UFRJ have provided me with a formidable graduate education and I am very grateful for the years dedicated for the MSc and DSc at COPPE/UFRJ. Several individuals from Faculty and Staff made their direct or indirect contributions to this thesis, but I would like to mention specially: Marise Santos for all the support and prompt help whenever it was needed, thank you so much, Marise. Special thanks also to Prof. Claudio Neves, for teaching me a lot about waves and Prof. Luiz Galiza -Lula- for all support and knowledge, both have had an enormous impact on the present research.

I would also like to express my thanks to Eric Firing and Jules Hummon from University of Hawaii for all the support, allowing me to finish my thesis, and also to my colleagues Thomas Roc and Toby Martin for the friendly support.

Many friends also supported one way or another along these three and a half years, but I will mention a few that contribute more closely; many thanks to Saulo Meirelles, Augusto Sepp Neves, Cesar Ribeiro and Diogo Peregrino, either scientific talks or "tea time" have inspired me a lot.

Thanks also to my brother Felipe, sister Christine and mom Leila for the encouragements in my life.

I would like to thank my dearest darling wife Cecilia Mauriel, for her constant love, encouragement and for all support throughout writing this thesis and in my life.

Resumo da Tese apresentada à COPPE/UFRJ como parte dos requisitos necessários para a obtenção do grau de Doutor em Ciências (D.Sc.)

INSTABILIDADE MODULACIONAL EM ONDAS NÃO LINEARES NA ÁGUA: ESTUDO EXPERIMENTAL

Uggo Ferreira de Pinho

Junho/2018

Orientadores: Nelson Violante-Carvalho
Wilton Zumpichiatti Arruda
Alexander Babanin

Programa: Engenharia Oceânica

Ondas oceânicas geradas pelo vento são multi-direcionais, mesmo se a direção do vento é constante. Direcionalidade pode ocorrer devido a superposição de ondas de cristas longas se propagando com um ângulo entre elas. Modulação lateral das cristas, porém, desempenha um papel importante em ondas estritamente unidirecionais devido a efeitos não-lineares. Na presente tese, investiga-se a direcionalidade e evolução de ondas de cristas-curtas, inicialmente unidirecionais. Para tal propósito, foram elaborados dois experimentos sobre instabilidade lateral de ondas monocromáticas, propagando em águas profundas. Nestes, ondas de cristas longas foram geradas com um ampla faixa de esbeltez e o surgimento da instabilidade modulacional foi analizado e quantificado. A modulação transversal das cristas foi evidente, sua magnitude mostrou-se dependente da esbeltez na direção de principal propagação e do número de ciclos propagados e sua escala espacial comparável ao comprimento de ondas da onda principal. Assim, o fenômeno de ondas de cristas-curtas é uma característica inerente às ondas não-lineares e devem ser levada em conta quando da estimativa das propriedades direcionais das ondas oceânicas.

Os resultados das análises do grande conjunto de dados gerado é apresentado quantificando parâmetros de ondas relacionados a instabilidade modulacional, a saber: 1) razão entre maximos e mínimos de cristas; 2) razão entre máximos de cristas e crista média inicial; 3) comprimento de ondas transversal da modulação foram calculados e comparados com comprimento de ondas logitudinal. É apresentada também uma análise estatistica dos parâmetros de ondas relacionados aos efeitos não-lineares em ondas com grande esbeltez.

Abstract of Thesis presented to COPPE/UFRJ as a partial fulfillment of the requirements for the degree of Doctor of Science (D.Sc.)

MODULATIONAL INSTABILITY ON NONLINEAR WATER WAVES: EXPERIMENTAL STUDY

Uggo Ferreira de Pinho

June/2018

Advisors: Nelson Violante-Carvalho
Wilton Zumpichiatti Arruda
Alexander Babanin

Department: Ocean Engineering

Ocean waves forced by the wind are multi-directional, even if the wind direction is steady. Directionality can occur due to the superposition of long-crested waves propagating at an angle to each other. Lateral modulation of the wave crests, however, also takes place for strictly unidirectional waves, due to nonlinear effects. In this research, the short-crestedness of unidirectional waves is investigated; for this purpose, two experiments on the lateral instability of monochromatic, deep water waves were performed in a large wave basin. In these two tests, long-crested waves were generated with a variety of wave steepnesses, and the emergence and evolution of the modulational instability was quantified and analyzed. The cross-modulation of wave crests was clearly visible, its magnitude depending on the wave steepness in the wave propagation direction and on how many wave cycles the waves travelled. Its spatial scale is comparable with the wavelength. Thus, short-crestedness is an inherent feature of nonlinear waves and should be taken into account when estimating directional properties of ocean waves.

The results of the analysis of the set of nonlinear waves generated is presented by quantifying special wave characteristics and parameters related to the modulational instability, namely: 1) the ratio between maximum and minimum amplitude in a single wave crest, 2) the ratio of maximum crest versus mean initial wave crest, and 3) transversal length of the crest modulation were calculated and compared with longitudinal wavelength. It is presented statistics analysis on wave parameters related with nonlinear effects on steep waves, such as wave height and period distributions, and breaking limit and spectral analysis of nonlinear waves.

Contents

List of Figures

List of Tables

Glossary

Sign	Description	unit
Ac	wave crest amplitude	m
Ac_0	mean wave crest measured at WP1, closest wave probe to the wavemaker	m
At	wave trough amplitude	m
C_g	wave group velocity, $\delta\omega/\delta k$	m/s
H	wave height, $H = 2a$	m
L_0	initial wavelength, measured at WP1	m
S_N	normalized energy of the sidebands (S_N = Energy spectrum/m0)	—
S_{spat}	spatial spectrum calculated at CSs	$m^2 s^{-2} Hz^{-1}$
T	wave period	s
$\boldsymbol{L}$	vector wavelength, $L = \|\boldsymbol{L}\|$	m
$\boldsymbol{k}$	initial vector wavenumber, measured at WP1 $k_0 = \|\boldsymbol{k}_0\|$, $k_0 = 2\pi/L_0$	m^{-1}
$\boldsymbol{k}$	vector wavenumber, $k = \|\boldsymbol{k}\|$, $k = 2\pi/L$	m^{-1}
δ	nondimensional frequency $\hat{\delta} \equiv \delta\omega/\epsilon\omega_0$ where $\delta\omega = \omega_{sb} - \omega_0$, ω_{sb} is the frequency of the sideband and ω_0 the frequency of the main carrier.	—
δ	normalized wave frequency differential $\delta = \Delta f/f0 = (f_0 - f)/f_0$	—
ϵ	wave steepness, $\epsilon = ak$	—
$\eta(t)$	water surface elevation	m
λ_b	transversal or lateral wavelenght of the modulation (perturbation)	m
ω	angular frequency, $\omega = 2\pi/T$	$rad.s^{-1}$
τ	small constant time	s
a	wave amplitude, $a = H/2$	m

Sign	Description	unit
a_0	initial wave amplitude, measured at WP1, $a_0 = H_0/2$	m
c_0	wave phase velocity, $c_0 = gT_0/(2\pi)$	m/s
f	wave frequency, $f = 1/T$	Hz
f_1	main carrier wave frequency	Hz
f_{sb}	sideband frequency	Hz
$m0$	order zero spectral momentum	m^2/Hz
CS	cross-section of wave probes, 8 WP in the first test and 15 WP in the second	—
D	distance from the wavemaker to the waveprobe	m
R	ratio $R = max(A_c)/min(A_c)$	—
S	ratio $R = max(A_c)/mean(Ac_0)$	—
WP	wave probe: conductivity-based liquid level detectors wave gauges	—

Chapter 1

Introduction

The linear wave theory of Airy (1841) provides very good approximations for mathematical relationships describing the wave form and wave motion when the waves have a small amplitude relative to their wavelength. It assumes that the fluid is inviscid and the flow is irrotational, so there is a velocity potential, that greatly simplifies the equations of motion. The linear theory accounts for a substantial part of our understanding of surface gravity water waves physics in the ocean, but it is unable to deal with nonlinear observed phenomena.

The assumptions taken in order to solve analytically Laplace's equation have been shown insufficient to explain important phenomena observed in nature, as we will see in this research. In 1847, Stokes [1] introduced some new and interesting properties of waves with finite amplitude, extending the Airy theory for weakly nonlinear wave motions. Their speed are larger than small amplitude waves of the same wavelength, and the wave speed increases when their wave heights increase. Considering that a wave steepness is the small parameter in the Stokes theory, the wave heights have a limit: when the ratio ak (a is the wave amplitude and k the wavenumber, where $k = 2\pi/L$, and L is the wavelength) reaches the limit of 0.4 ($H \approx 13\%$ of the wavelength). At this steepness limit, the wave becomes unstable and breaks, even in deep water. For a long time, it was thought that Stokes waves could propagate indefinitely without changing their shape or, in other words, it was thought that the Stokes wave was a stable solution. In 1967, however, two British physicists, T. Brooke Benjamin and Jim E. Feir, discovered by accident that a train of Stokes waves may become unstable after traveling some distance in a wave tank. This important discovery is known as the Benjamin-Feir Instability.

The two researchers intended to generate a train of waves with constant frequency and amplitude, but unexpectedly, their wave generator imposed a slow variation of amplitude along the length of the train. The wave train moved down the tank until two new wave frequencies suddenly appeared in the train. One frequency was slightly higher than the primary wave's frequency, and the other was slightly lower,

called *sidebands*. The details about their experiment was published in Jim E. Feir's PhD thesis, but the author couldn't have access to this publication.

These sidebands grew exponentially in height at the expense of the primary wave (carrier), which eventually disintegrated. After eliminating all possible sources of equipment vibrations and imprecision, Benjamin and Feir determined that this nonlinear phenomenon was indeed real: the slight amplitude deviation was reinforced nonlinearly, leading to this sideband instability.

Water waves with finite amplitudes (Stokes waves) are, therefore, nonlinear and are subjected to modulational, or Benjamin-Feir, instability. In order to examine the effects of the modulational instability on mechanically-generated water waves, initially long-crested (monochromatic) and propagating in deep water, two sets of experiments were carried out in a wave tank with large dimensions, taking very detailed measurements in many points along its length. All the waves were generated as long-crested waves and were allowed to propagate freely along the deep water wave tank, with no external forces acting as wind and currents. The first set explored the emergence of directionality on initially unidirectional steep waves. The second was conceived in a way to cover questions raised in the first one, in order to explore the growth of sideband and lateral modulation on a broader range of wave steepness in waves with finite amplitude.

The wave steepness ($\epsilon = ak$) range generated was from $\epsilon = 0.05$ (linear waves) up to values close to the wave breaking limit, usually referred in the literature as $\epsilon = 0.4$. Based on data analysis in the frequency and time domain, it was possible to investigate spectral sideband growth, wave group and wave packets (breathers) generation with large amplitudes, as well as the emergence of directionality on initially long-crested waves. The results found are compared to the literature.

The goal of this study is to contribute to the study of modulational instability effects on Stokes waves and the outline of this thesis is the following. As an introduction to the main subject, the experimental approach and a bibliographic review is presented in Chapter 2 in which some of the main publications in the subject are listed briefly. A description of the wave facility, data acquisition, and the data analysis methodology is given in Chapter 3.

Chapter 4 presents the experimental results of an investigation of directionality effects on mechanically-generated, initially monochromatic Stokes waves in a large and deep wave basin. All the waves were generated as long-crested waves and were allowed to propagate freely along the deep water wave tank, with no external forces acting as wind and currents. It highlights how initially long-crested steep waves, with wavelengths short enough, become short crested and acquire directional characteristics, as a result of modulational instability effects. This Chapter is based on a data set collected in a first wave tank test, planned in such a way to generate

spatial and temporal data sets relevant to the study of two dimensional modulational instability effects. As briefly presented in Chapter 4, crest transformations can be quantified by calculating the ratio between the maximum and minimum crest height measured in an aligned array of wave probes.

From Chapter 5 onward, the data set used on the analysis was measured in a second experiment. Compared to the first one presented in Chapter 4, the second test have substantially more wave samples (total of 84 compared to the 10 of the first test) and more than double of wave probes (32 against 12 in the first one).

Weakly nonlinear Stokes waves are known to be unstable under small perturbations in specific frequencies. Sidebands in the spectrum grow exponentially as those perturbations interact with the main carrier. This phenomena is explored in Chapter 5. These waves are subjected to many transformations while propagating along the tank, due to nonlinear effects and wave-wave interactions driven by modulational instability. A statistical approach is used in Chapter 7 to investigate the main changes on wave parameters: wave crest and height, wavelength and period, and related wave characteristics (steepness among others).

It was also demonstrated in chapter 6 that weak nonlinear waves can become a chaotic system beyond certain critical initial wave steepness. In order to demonstrate this assertion time and frequency domain analysis were carried out following usual techniques for qualitative analysis of chaotic motions described in the literature.

The main results and contributions to the subject of modulational instability of finite amplitudes waves are summarized in Chapter 8, and suggestions for future research are presented.

Chapter 2

Literature Review

2.1 Literature Review

Since Stokes presented the nonlinear theory in 1847, it was thought that finite amplitude waves (or Stokes waves) could propagate indefinitely without change of shape. About one hundred years later, in the 1960's researchers in the UK and in Soviet Union, almost independently have shown that Stokes waves are actually unstable to small perturbations in the media. First, Zakharov published a paper in 1966 ([2]) describing mathematically the instability of waves in nonlinear dispersive media, but because the publication was writen in Russian. One year after, in 1967, two British physicists, T. Brooke Benjamin and his student Jim E. Feir [3], discovered accidentally that a train of Stokes waves can become unstable after traveling some distance in a wave tank. This important discovery about the effect of modulational instability on unstable finite amplitude waves is known as the Benjamin-Feir Instability. They showed that weakly nonlinear Stokes free-surface waves have unstable behavior due to the sideband instabilities. In other words, when generating "monochromatic" Stokes waves in the laboratory, infinitesimal perturbations (or background noise) in special frequencies (sideband), in relation to the main Stokes wave (carrier wave), interact with its sideband as follows: The modulational instability arises as a nonlinear coupling (interaction) between the strong carrier harmonic and unperturbed primary wave, at a frequency ω and small sideband perturbations with frequencies $w+$ and $w-$, producing modulation in the wave envelope. As a consequence of coupling the nonlinear boundary conditions, energy is transferred from the primary motion to the sideband at a rate that can increase exponentially as the interaction proceeds [3]. Independently, using a Hamiltonian approach, Zakharov [4] derived the same instability result. Furthermore, in the context of modulated water waves, he obtained the famous Nonlinear Schrödinger equation.

As pointed out by Phillips, (1966) [5], it is remarkable the weakness of the

property of mutual interaction of deep water gravity waves. In a system of interacting waves, the magnitude of the non-linear terms is always small compared with the dominant linear terms (being relatively of the order of the root means square slope - or wave steepness squared). He also highlight that the method suggested by Stokes 1847 [1] has on its first and second order motion small influence of a small perturbation and resonance cannot occur up to second-order. For the next approximation, the third-order, from three primary wave interaction, three components will be generated and from many combinations possible to the interaction from primary waves with the components, there is one set that the resonance condition is satisfied, namely:

$$\begin{aligned} \mathbf{k_1} + \mathbf{k_2} &= \mathbf{k_3} + \mathbf{k_4} \\ \omega_1 + \omega_2 &= \omega_3 + \omega_4 \end{aligned} \tag{2.1}$$

where $\mathbf{k}$ is the wave vector (for details refer to [6]).

If four wave components are such that 2.1 is satisfied, then there exists the possibility of resonance and energy interchange. Phillips (1966) [5] mentioned also that the interaction is best described as *very weak*; weak because non-linear terms represent small perturbation to the linear wave (Laplace) equation, *very weak* because a higher order perturbation is involved. And, finally, he points that: *"Yet this appears to be the dominant mechanism for energy interchange among wave components"*. In other words, the growth of the sideband can be treated in terms of amplification of weak modulations imposed on a harmonic wave [7]. The most unstable mode has the maximum growth rate that has the wavenumber $2a_0k_0^2$, in the direction of the primary waves [8].

The Benjamin-Feir instability is often cited as the first step in a nonlinear process that spreads energy from an initially narrow bandwidth to a broader bandwidth, as mentioned above. In this process, sidebands grow exponentially until nonlinear interactions eventually bound their growth. The instability is a finite-amplitude effect, in the sense that the unperturbed wavetrain (the carrier wave) must have finite amplitude, and the growth rate of the instability is proportional to the square of that amplitude, at least for small amplitudes [9]. When Benjamin and Feir published their results [3] doubt was expressed about the originality of their analysis. There had been earlier publications on resonant wave-wave interactions by Phillips, 1960 [10], on the general nonlinear analysis of interactions between waves of different frequency and wavelength by Hasselmann, (1962) [6], and on other specific wave-wave interactions. But, as Hasselmann recognized, he had not applied his analysis to study the basic questions about the stability of Stokes waves. So it is now generally accepted that Hasselmann is credited with the first general nonlinear wave analysis and Benjamin with the stability analysis. Also, the nonlinear transition in the

behavior of waves at the critical slope had been pointed out earlier by Whitham, (1966) [11].

The necessary conditions for the instability are that waves should have finite amplitude, should be dispersive (i.e., waves of different frequencies have different group velocities in the linearized limit) and that dissipation should be weak enough that it can be ignored at this order of approximation [9]. It is also known now that there exists at least two qualitatively different types of instability of surface gravity waves on deep water:

1. The first type discovered by Benjamin and Feir [3] is horizontal two-dimensional (2D) in general (one dimension in the direction of propagation of the carrier and the other dimension in other directions), but usually only the most unstable horizontal one-dimensional (1D) mode manifests itself in the evolution of initially uniform wave trains, in a way that this instability is essentially one-dimensional [12]. This type of instability was first denominated by McLean et al. [13] as instability type I. It was subsequently analyzed in detail by Longuet-Higgins [14], McLean [15] and Yuen and Lake [16].

2. McLean *et al.* [13] and Longuet-Higgins [14, 17] discovered theoretically, through independent efforts, a second type of instability denominated by McLean *et al. [13] as type II. This type of instability has the important features:*

    a *This instability is both two- and one-dimensional, but its most unstable mode with maximum growth rate for perturbations is always two-dimensional, with the most unstable perturbation wavenumber equal to* $1/2k_0$*, or the half of the primary wave;*

    b *Its growth rate is small for small* a_0k_0*, and about equal to the growth rate of the first type when* $a_0k_0 \approx 0.26$ *(Su and Green, 1984 [8]);*

    c *The one-dimensional manifestation of the second type occurs only for* $a_0k_0 \approx 0.41$*, so it is predominantly two-dimensional when the waves have steepness lower than* $a_0k_0 \leq 0.4$ *[12]. Longuet-Higgins [14, 17] used normal-mode analysis to study strongly nonlinear waves instability to small (linear) perturbations. It showed that for those very strong instabilities at* $\epsilon \approx 0.41$*, a plunging breaker is initiated [18].*

Longuet-Higgings [14] has classified "subharmonic" instabilities as those with low rates of growth at low wave steepness type I, and, at high wave steepness type II, local "superharmonics" instabilities leading to the wave breaking. Between these

two types of instability, he considered an intermediate range of wave steepness where the unperturbed wave train is neutrally stable.

Following his description, the subharmonic instabilities of the Benjamin-Feir, or type I, would be confined to waves with steepness ak within a certain finite range, with the upper limit being at $\epsilon \approx 0.37$ and maximum growth-rate at $\epsilon \approx 0.32$. The wavelengths of the subharmonics are greater than that of the unperturbed wave [14]. Secondly, the "superharmonic" (McLean type II) instabilities would be stronger when $\epsilon \approx 0.41$ and would have much higher rates of growth, and it is suggested that they lead directly to the overturning of the free surface (breaking) [14].

Most of the experimental research on modulational instability were carried out from 1960's to 1980's. Benjamin-Feir 1967, [3], as cited above, was the first and one of the most important work on the subject, and they analyzed waves with wave steepness in the range $\epsilon = 0.07 - 0.16$ [19], the experiment was carried out at Ship Division of the National Physical Laboratory, at Feltham, but no much detail on the experiment itself was published.

Lake *et al.* 1977 [20], also presented a research based on the evolution of a nonlinear wave train on deep water and they found that at an initial stage of evolution was characterized by exponential growth of the modulational instability. But at later stages the instability did not result in wave-train disintegration as pointed out by Benjamin-Feir, instead they reported an increase and decrease of the modulation or a Fermi-Pasta-Ulam recurrence phenomenon. Their experiment was taken in a wave tank with 1m x 1m x 12m, and they positioned wave probes at 1.5m, 3m, 4.5m, 6m, 7.5m and 9m from the wavemaker. The waves generated in this experiment had wave heights varying from 0.0254cm (0.01in) to 5cm (2in) and period from 0.2 to 1s, and typically initial wave steepness $\epsilon = 0.1 - 0.35$. Lake's experiment, however, have a fundamental difference to the present thesis, each wave train was generated with an amplitude modulation imposed initially in the wavemaker, this will be refered as "seeded" experiment. Another important result reported at first by Lake *et al.* (1977), was the frequency downshift in the evolution of Stokes waves, where the peak of the spectrum is downshifted along the wave train propagation.

The evolution of a nonlinear deep-water wave train to breaking was reported by Melville, 1982 [18]. His experiment was conducted in a glass channel with dimensions 28m long, 50cm wide and 60cm of water depth. The wave frequency was $w_0 = 2Hz$ ($T_0 = 0.5s$, $k_0 = 0.161cm^{-1}$) and he varied the amplitude in order to have wave steepness varying in the range $\epsilon = 0.16 - 0.29$. His measurements were based on wave gauges (spatial positioning was not described in their paper) and 500 frames/s film. Their main motivation was to study wave breaking relation to the modulational instability. They found a qualitative agreement with Lake *et al.* (1977) [20] on the

evolution of the side-band growth, but a remarkable asymmetry between the upper and lower side bands leading to the lower side band to increase up to an amplitude greater than that of the primary wave, and he pointed out that the increase of the asymmetry corresponds to the onset of wave breaking. The reason is that higher frequency modes have their energy dissipated by wave breaking. He also found that their observations were in agreement with McLean *et al.* (1981) [13] in regard that class I instability had the larger maximum growth rates for $\epsilon \leq 0.28$, meaning the evolution of the wave train was essentially two-dimensional, and class II dominated for larger steepness, meaning fully three-dimensional.

Su and Green (1984) [8] show the results of an experimental investigation by analyzing waves mechanically generated with initial steepness in the range $\epsilon = 0.09 - 0.20$ in a wave tank 167m long, 3.7m wide and 3.7m deep. They investigated experimentally the coupling of the one- (type I) and two-dimensional (type II) instabilities of free surface gravity waves on deep water with initial steepness of $0.09 \leq \epsilon \leq 0.20$. They found that essentially one-dimensional instabilities (type I) caused sufficient wave train modulation to trigger the predominantly two-dimensional instabilities (type II). The type II, in turn, limits the growth of type I, and leads to wave breaking and the directional spreading of the wave energy. The authors concluded that the type I and type II instabilities interact strongly during the evolution of wave trains with moderate initial steepness. Still, according to these authors, type I and type II instabilities have been treated as independent physical processes, but it could be the case only in two special situations: when ϵ is small ($\epsilon \leq 0.10$) or when it is large ($a_0 k_0 \geq 0.25$). But, for intermediate range of steepness $0.10 \leq a_0 k_0 \leq 0.25$, type I and type II have comparable strength. They highlight that this range ($0.12 \leq \epsilon \leq 0.20$) is approximately the most pertinent for ocean wind wave growth stages.

More recently, Tulin and Waseda (1999) [21] reported important results on the evolution of nonlinear wave groups in a "seeded" experiment (side-bands generated in the wavemaker) performed in a wave tank 50m long, 4.2m wide and 2.1m deep. The waves generated were 1.0-4.0m long ($T = 0.8 - 1.6s$) and wave steepness in the rage $\epsilon = 0.1 - 0.28$ and normalized sideband frequency differences $\delta\omega/\epsilon\omega = 0.2 - 1.4$. They used an array of 8 wave probes along the wave tank at the distances from the wavemaker: 3.6m, 9.0m, 14.4m, 19.8m, 25.2m, 30.6m and 41.4m. Their study was not concerned with transversal component of the modulational instability. One of the important outcomes from their research was related to a simple direct relationship between rate of downshifting and breaking. As described in the next chapters, both phenomena were observed here.

2.2 Theoretical Review

A brief mathematical review is presented below. It will merely highlight the results here and refer to the excellent treatments of the details in the books by Osborne [22], Mei *et al.* [23] and Kharif *et al.* [24].

2.2.1 Perturbation Method

When Benjamin and Feir ([3], [19]) discovered modulational instability for nonlinear Stokes waves on the water surface, it was actually a surprise since the existence of stationary nonlinear (Stokes) waves had been mathematically proven decades earlier, and suddenly it was found that although such solutions exist mathematically, they are unstable.

In their first work on this matter, Benjamin and Feir [3] performed a perturbation analysis of the uniform wave train on the Euler equations. They demonstrated experimentally and explained theoretically by using a spectral approach, starting from potential equations and boundary conditions for the one dimensional potential, $\phi(x, z, t)$, and the surface displacement, $Z = \eta(x, z, t)$ in the form for deep water:

$$\nabla^2\phi = 0 \quad , \quad -\infty < z \leq \eta, \tag{2.2}$$

$$\phi_{xx} + \phi_{zz} = 0. \tag{2.3}$$

$$\nabla\phi \to 0 \quad , \quad z \to -\infty \tag{2.4}$$

$$\eta_t + \eta_x\phi_x + \eta_y\phi_y - \phi_z = 0 \quad , \quad z = \eta \tag{2.5}$$

$$g\eta + \phi_t + \frac{1}{2}\left(\phi_x^2 + \phi_y^2 + \phi_z^2\right) = 0 \quad , \quad z = \eta \tag{2.6}$$

where g is gravity acceleration; $z = 0$ corresponding to a non-perturbed surface. A known solution of these equations is a progressive (Stokes) water wave, in which only the basic (first) and the second harmonics are retained:

$$\eta = H \approx a\Big(cos\zeta + \frac{1}{2}akcos2\zeta\Big), \tag{2.7}$$

$$\phi = \Phi \approx \omega k^{-1} a e^{kz} sin\zeta,$$

$$\omega^2 \approx gk(1 + k^2a^2),$$

where $\zeta = kx - \omega t$, and a is the wave amplitude. Then small perturbations are added to this solution, each being represented as a sum of spectral components at frequencies $\omega \pm \Omega$, where Ω is a modulational frequency and $\Omega \ll \omega$. In other words, the wave is now represented in the form $\eta = H + \eta_1 + \eta_2$, $\phi = \Phi + \theta_1 + \theta_2$. The

sideband waves η_1 and η_2 have amplitudes $\epsilon_{1,2}$ and phases:

$\zeta_{1,2} = k(1 \pm \kappa)\chi - \omega(1 \pm \delta)t - \gamma_{1,2}$

where κ and $\delta = \Omega/\omega$ are small fractions satisfying the relation $\delta\omega = c_g \kappa k$, and $c_g = g/(2\omega)$ is the linear group velocity at the main frequency. The parameters $\gamma_{1,2}$ are corrections that arise due to dispersion (i.e., a difference of group velocities at the main wave and the side components) and to nonlinearity. If $\theta = \gamma_1 + \gamma_2$, the four-wave resonance occurs when $2\zeta = \zeta_1 + \zeta_2 + const$, resulting in the possibility of perturbation growth. Zakharov & Ostrovsky [7], presented in his research the normalized sideband frequencies (x-axis) with respect to the main carrier frequency ($x = 0$) and its amplitudes (Growth rate of the sideband amplitudes dependency on the frequency, Figure 4. of Zakharov, [7]).

Substituting perturbed η and ϕ with slowly varying $\epsilon_{1,2}(t)$ and $\theta(t)$ into equation 2.3 and keeping only the resonant terms, after some transformations we have:

$$\frac{d\epsilon\pm}{dt} = \frac{1}{2}(\omega k^2 a^2 sin\theta)\epsilon\mp, \tag{2.8}$$

$$\frac{d\theta}{dt} = \omega k^2 a^2 \Big(1 + \frac{\epsilon_1^2 + \epsilon_2^2}{2\epsilon_1\epsilon_2} cos\theta\Big) - \Omega^2/\omega$$

For Stokes waves, this yields instability with growth rate

$$\gamma = \frac{1}{2}\delta(2k^2a^2 - \delta^2)^{1/2}. \tag{2.9}$$

From 2.9 it can be noticed that instability exists in a limited range of frequencies:

$$\Omega < \Omega_S = \omega ka\sqrt{2}. \tag{2.10}$$

The maximum growth rate is achieved at $\Omega = \Omega_S/\sqrt{2} = \omega ka$. A wave train with initial amplitude a_0, wavenumber k_0 and frequency ω_0 is unstable under perturbations with frequency $\delta\omega$, when the following conditions are satisfied (Tulin and Waseda [21]):

$$0 < \hat{\delta} \leq \sqrt{2}, \tag{2.11}$$

following their definition $\hat{\delta} \equiv \delta\omega/\epsilon\omega_0$ and $\epsilon \equiv a_0 k_0$. These authors pointed out also that modulational instability should be considered as an interaction of three monochromatic wave trains: the carrier wave with initial frequency ω_0, the upper sideband (ω_+), and lower sideband (ω_-). They should satisfy the following conditions:

$$\left.\begin{aligned} 2\omega_0 &= \omega_+ + \omega_-, \\ \omega_\pm &= \omega_0 \pm \delta\omega, \\ 2k_0 &= k_+ + k_- + \Delta k \end{aligned}\right\} \tag{2.12}$$

where Δk is a slight mismatch of the wavenumber from Phillips' four wave resonance condition ([10]) for infinitesimal waves [21]. These authors found the same expression for sideband growth expressed in equation 2.9, due to cancellation of the resonant de-tunning when amplitude dispersion is present. The sideband grows exponentially and the growth rate $\mathrm{d}(\ln a)/\mathrm{d}(kx)$ is

$$\beta = \epsilon^2 \hat{\delta}(2 - \hat{\delta}^2)^{1/2} \tag{2.13}$$

The maximum growth of the sideband is produced when $\hat{\delta} = 1.0$ (Zakharov & Ostrovsky, 2009 [7]).

2.2.2 Schrödinger Equation

It was shown by Zakharov [4] that equations of the type 2.3, 2.5 and 2.6 for the weakly nonlinear waves on the surface of deep fluid can be reduced to a Hamiltonian form

$$\frac{\partial \eta}{\partial t} = \frac{\delta E}{\delta \phi_S}, \frac{\partial \phi_S}{\partial t} = -\frac{\delta E}{\delta \eta}. \tag{2.14}$$

where ϕ_S is the potential at the surface, $z = \eta$, and E is energy (Hamiltonian). The dynamic equations are expressed in terms of Fourier components $a(k)$, considered as new complex canonical variables:

$$\eta(\mathbf{k}) = \sqrt{\frac{|\mathbf{k}|}{2\omega(\mathbf{k})}}[\mathbf{a}(\mathbf{k}) + \mathbf{a}^*(-\mathbf{k})]. \tag{2.15}$$

$$\phi_S(\mathbf{k}) = -\mathbf{i}\sqrt{\frac{\omega(\mathbf{k})}{2(|\mathbf{k}|}}[\mathbf{a}(\mathbf{k}) - \mathbf{a}^*(-\mathbf{k})].$$

The Hamiltonian equation becomes:

$$\frac{\partial a(\mathbf{k})}{\partial t} = -i\frac{\delta E}{\delta a^*(\mathbf{k})}. \tag{2.16}$$

The energy E is then represented as a series in powers of $a(k)$ and a^*k up to quadratic term, integrated over all ranges of wave vectors. For weakly nonlinear waves, the complex amplitudes can be presented in the form $a(k) \approx A(k,t)\exp[-i\omega(\mathbf{k})\mathbf{t}]$, where A is a slowly varying function.

For a wave packet with a narrow spectrum, the nonlinear Schrödinger equation

(NSE) follows from here for the wave envelope; in one-dimensional case it has the form

$$\frac{\partial \phi_S}{\partial t} - \frac{\lambda}{2}\frac{\partial^2 \phi_S}{\partial \xi^2} = -w|\phi_S|^2\phi_S, \tag{2.17}$$

where $\xi = \chi - v_{gr}t$, $v_{gr} = d\omega/dk$, $\lambda d^2\omega/dk^2$. This equation has a solution of a constant-amplitude harmonic wave, the phase velocity of which depends on the amplitude. Namely, at given $k = k_0$, the frequency is $\omega = w_0 b_0^2$, where b_0 is proportional to the wave amplitude. Adding a perturbation so that $\phi_S = e^{-iw|b_0|^2 t}(b_0 + \alpha e^{-i\Omega t + ik\xi} + \alpha^* e^{i\Omega t - ik\xi})$ and linearizing Eq. 2.17, we have

$$\Omega^2 = w\lambda\kappa^2|b_0|^2 + \lambda^2\kappa^2/4. \tag{2.18}$$

The instability is possible in this case if $w\lambda < 0$.

Chapter 3

The wave tank and data analysis methodology

3.1 Wave tank facility - LabOceano

The two experiments described in this thesis were performed in the Brazilian Ocean Basin LabOceano of the Ocean Engineering Department at the Rio de Janeiro Federal University, which is a wave tank with dimensions $L = 40$ m, $W = 30m$ (wave-tank width will be also referred with the letter b, i.e. $b = 30$) and 15 m deep. All waves were generated by 76 identical rectangular flap type plungers with individual motion control, driven by a sinusoidal signal generator (see Figure 3.1). The wave generator is capable to generate regular waves with periods ranging from 0.5 to 5 seconds and wave heights up to 50 cm. No wind or current was generated.

The wave tank was designed to have a energy dissipation beach located in the opposite side of the wavemakers (the beach began 35 m from the wavemakers) to provide energy dissipation. One of the sides of the tank has a vertical wall, and the opposite side has a lateral beach with the same slope and design as the one at the end of the tank.

3.1.1 Wave measurement devices

The water surface displacements is measured with conductivity-based liquid level detectors (wave gauges), referenced here as wave probes (WP). The precision of the measurements was 1.5 mm and 60Hz of sample frequency. The sets of wave probes can be seen on Figure 4.1 and 5.1.

Figure 3.1: Wavemaker: 76 paddles.

3.2 Data analysis methodology

In order to calculate the main wave parameters in the time and frequency domains, as well as conduct spatial analysis, a wide sort of statistical and spectral tools were used along with this thesis. The next sections present the main tools and descriptions of these analysis.

3.2.1 Time domain analysis

A zero up- and down-crossing time series analysis was performed by using the WAFO Matlab Toolbox (http://www.maths.lth.se/matstat/wafo/). The individual wave period, wave amplitude and wave height were obtained by this analysis and the wavelength ($L \approx gT^2/2\pi$ for linear waves in deep water and $k = 2\pi/L$) was ascertained.

3.2.2 Spectral analysis *S(f)* - frequency domain

The spectral analysis was made using WAFO Matlab Toolbox (http://www.maths.lth.se/matstat/wafo)). For longer waves (wave period of

one second ($1s$) or higher) 2048 points was used for spectral analysis and for the shorter waves 1024 points were used for the spectral calculation.

3.2.3 Spectral analysis *S(k)* - spatial domain

The spatial spectral analysis $S(k)$ was performed using the function Spectf.m (Appendix C). The spatial resolution was 0.5m in the first experiment and 1 meter in the second, which is the distance between the wave probes on cross sections 1 and 2 (Figures 4.1 and 5.1). The cross sections have 8 wave probes in the first test and 15 wave probes for each section in the second test.

3.3 Wave definitions

The main wave characteristics and wave parameters can be summarized in Figure 3.2.

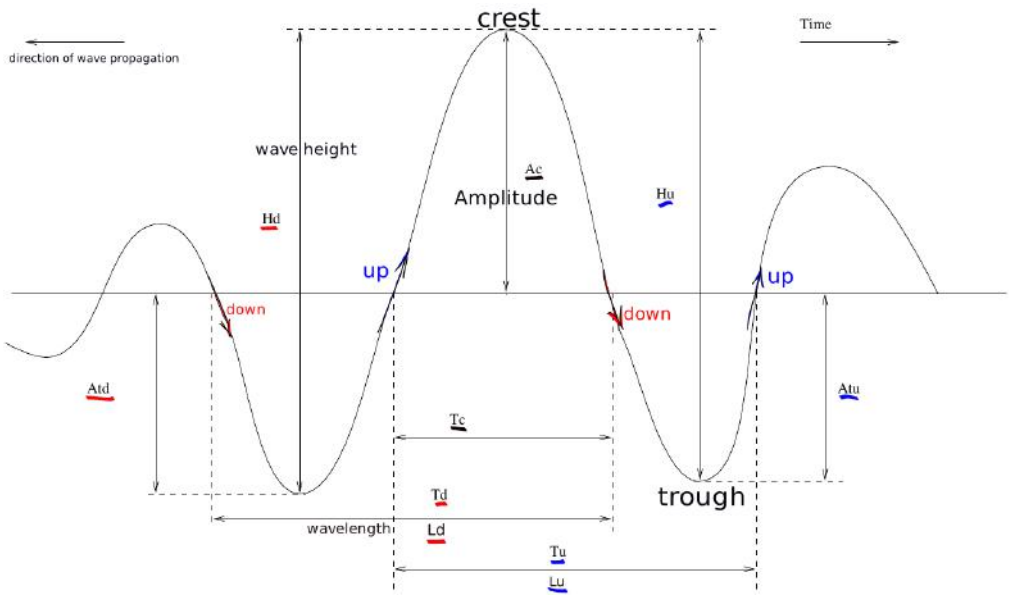

Figure 3.2: Wave parameters and definitions.

3.3.1 Wave amplitude

Small amplitude (linear) waves:

The wave amplitude a can be defined as the vertical distance from the still water level to the top of the crest (A_c) or the bottom of the trough A_t (A_{td} for zero down-crossing wave definition, marked with red color or A_{tu} for zero up-crossing wave definition marked with blue) (Figure 3.2). The wave height H can be defined as

the vertical distance from the top of the crest to the bottom of the following trough (zero up-crossing wave definition), or from the previous trough (zero down-crossing wave). For small wave amplitudes $H = 2a$.

Finite amplitude (Stokes) waves:

However, for the nonlinear case, the *crest amplitudes* (A_c) are bigger than the *trough amplitudes* (A_t) (Figure 3.3)

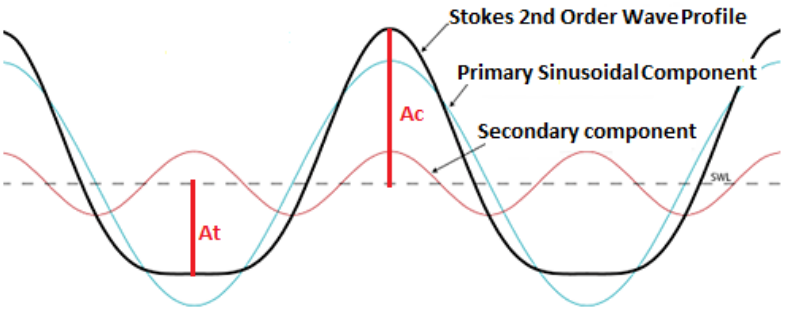

Figure 3.3: Stokes' wave amplitude.

3.3.2 Wave steepness (ϵ)

The wave steepness (ϵ) can be defined as $\epsilon = \frac{H}{2}k$, where k is the wave number $k = 2\pi/L$ for small amplitude (linear) waves or, for Stokes waves, $\epsilon = A_c k$, where A_c is the *crest amplitude* (Figure 3.3).

Most of the studies on modulational instability ([3], [19],[13] and [25]) use the definition $\epsilon = \frac{H_0}{2}k$, where H_0 is the wave height of the unmodulated wave.

Melville [18] defined the wave amplitude as:

$$a = \frac{1}{2}(\overline{Ac}_{max} - \overline{Ac}_{min})_{xk_0},$$

where $xk_0 = 41.9$ is the position of the first measuring station, and $\overline{Ac}_{max}$ and $\overline{Ac}_{min}$ are the averaged crest and trough elevation over about 100 waves.

Following the definition presented by Melville ([18]), it was used:

$$a = \frac{1}{2}(\overline{a}_{max} - \overline{a}_{min})_{WP_1}, \tag{3.1}$$

where the subscript WP_1 is regarded as the measurements taken at wave probe 1, located 7.5 meters from the wavemaker (Figure 4.1 and 5.1).

Chapter 4

Emergence of Short-Crestedness in Originally Unidirectional Nonlinear Waves

4.1 Introduction

The evolution of progressive long crested finite amplitude waves initially unidirectional and the emergency of directionality as a result of nonlinear modulational effects is the main subject of the present chapter and was also published recently by Pinho and Babanin [26]. Experimental results are presented without appealing to any suitable theory and assumptions on the nature of such modulation. Properties of the modulation, as shown, are measured by the cross-array of nine wave probes (see chapter 3). The experiments were conducted for mechanically-generated waves, not necessarily very steep, which were initially produced long-crested and monochromatic. Therefore the short-crestedness observed were developed within initially unidirectional wave trains and is a result of their nonlinear evolution. Note that we discuss this mechanism as such, without putting this in context of its relative importance by comparison with the traditional definition of short-crestedness through superposition of directional waves.

4.2 Experiment description

In order to observe the evolution of wave crests along the tank and their modulation across the tank, 12 wave probes were distributed as shown in Figure 4.1. The main characteristics of the wave tank, the Brazilian Ocean Basin LabOceano, was described in section 3.1. Along the direction of wave propagation, surface elevations were recorded as time series at wave probes (WP) WP1, WP2, WP3 and cross-tank

array (CWS hereinafter) of WP4 to WP12 probes. CWS was situated 30 meters away from the wavemaker (closer to the beach), and provided detailed account of lateral features of the wave crest and their evolution in time at this location. In CWS, the distance between the probes (wave probes #4 to #12) was 50 cm. Note that initially the waves were generated long-crested and their lateral cross-section was uniform. The wave probe sampling frequency was 60Hz (dt= 0.0167s).

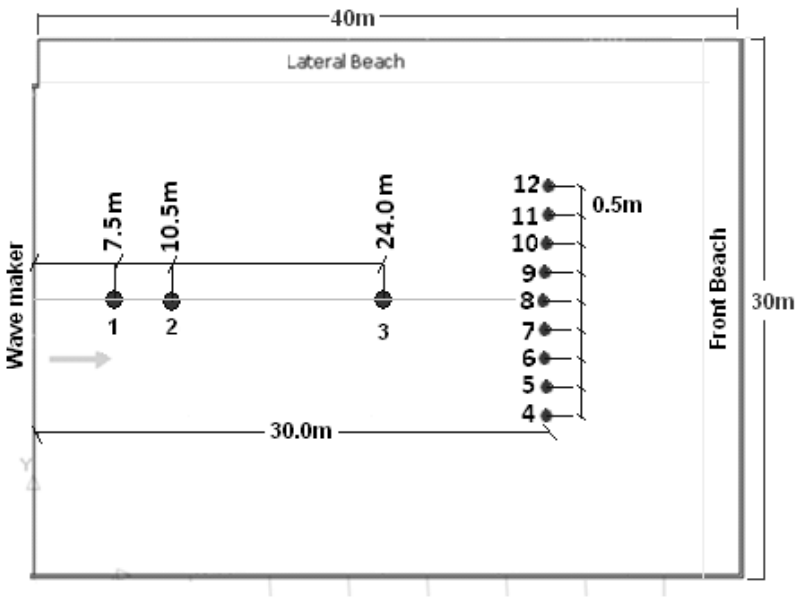

Figure 4.1: Wave probe layout. Black dots are locations of the probes.

In this experiment, uniform long-crested wave trains were mechanically generated with heights of 5 and 10 cm and wave periods of 0.6, 0.8 and 1.0 seconds, corresponding to wavelengths of 0.56, $\approx$ 1 and 1.56 meters, respectively, as shown in Table 4.1. This table shows the waves parameters inputted through the wavemaker and the corresponding wave steepness $\epsilon = ak$ actually measured at WP1. Here, a is wave amplitude, and k is wavenumber obtained from the input period through dispersion relationship, $k = \frac{2\pi}{L}$, L is wavelength. Every setup was repeated twice and every new run was conducted after the water completely settled.

The wave trains were produced in such a way that, once the waves reached the Front Beach (Figure 4.1), at the end of the tank, the generation of new waves was paused and recording was stopped in order to avoid the interaction of incoming wave trains with reflection from the beach and the development of sloshing motion of the tank. As a result, for shorter waves there was a greater number of individual waves in the train, since such waves propagate slower. Note also that there are more waves recorded by the wave probes closer to the wavemaker. For waves with period of 0.6 seconds, for example, 146 waves were measured by WP1 and 68 waves by WPs close

to the Beach (WP4-WP12), while for the longer waves with 1 second period, the number of waves at WP1 was 132, and 103 waves at WP4 to WP12.

Here, nonlinear wave evolution that leads to the cross-wave modulational is the subject of this chapter, but it is that subharmonics of the forcing frequency for the sloshing motion can also cause cross-wave modulational in a rectangular tank [27]. The frequencies used here (Table 4.1) are not such subharmonics, and with the wavemaker amplitude being of the order $s \sim 0.1m$, the small parameter of [27] is $s/b \sim 0.01$, where b is the tank width (see 3.1). Hence their slow time is of the order of 10^{-4} of the cross-tank time scale ($1.75s$) and the sloshing subharmonics could not have developed. As described above, the wavemaker was stopped as soon as the wave train reached the beach, which would take 25 seconds maximum depending on the wave frequency.

Table 4.1: Summary of the wave parameters inputted and the steepness measured at WP1.

Wave height	**Wave Period**	**Wave Length**	**Steepness** $\epsilon = ak$
5 cm	0.6 s	0.56 m	$0.20 < \epsilon < 0.26$
5 cm	0.8 s	0.99 m	$0.14 < \epsilon < 0.15$
5 cm	1.0 s	1.56 m	$\epsilon = 0.093$
10 cm	0.8 s	0.99 m	$0.26 < \epsilon < 0.28$
10 cm	1.0 s	1.56 m	$0.17 < \epsilon < 0.19$

4.3 Results

Nonlinear evolution of the wave trains is now analysed based on the measurements along and across the tank. Figure 4.2 shows the extent of the lateral modulation found at CWS, plotted versus the mean steepness of wave trains as measured close to the wavemaker at WP1. Vertical scale is ratio R of maximal amplitude of a wave crest A_c to its minimal amplitude, across the tank. For a given mean steepness, each point corresponds to a single wave crest that is if there are 20 points at steepness of 0.09, this means that 20 crests were measured on the cross section CWS and the value of R calculated and plotted on y-axis.

When the wave is generated long-crested, there is no cross-crest modulational, that is initially $R = Ac_{max}/Ac_{min} = 1$. Clearly, for every wave at each mean steepness R is greater than the unity ($R > 1$) at CWS. This means that by the time the waves traveled the 30m, they develop a cross-crest structure. For waves of lower steepnesses, on average $R \approx 1.2$. This means lateral modulational of wave crests of the order of 10% of their magnitude, i.e. even weakly nonlinear unidirectional

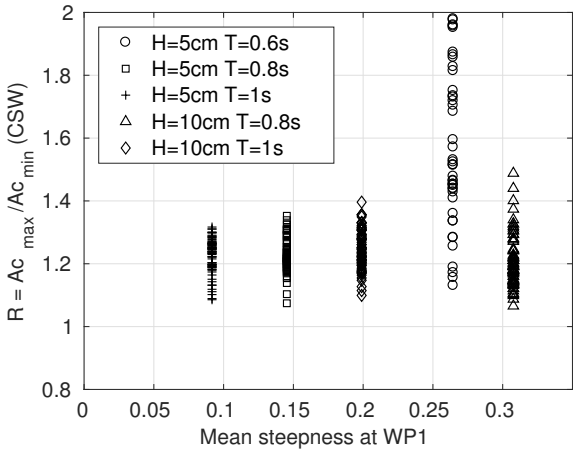

Figure 4.2: Cross-crest modulational over the CWS versus mean wave steepness at WP1. Each symbol corresponds to an individual wave crest.

longcrested waves become shortcrested. For larger steepnesses, ratio R grows, reaching up maxima being almost twice as high as minima at the steepness of $\epsilon = 0.26$. For higher mean steepness, this ratio drops down again (see discussion of Figure 4.4 below).

As the variation among highest crests and the lower ones is high and the figure 4.2 has shown a large values spreading, another way of quantifying the non-linear effects along the wave propagation from the generation field is by comparing the highest crest measured in the CWS with mean crests closest to the wavemaker, at WP1. Figure 4.3 shows these values.

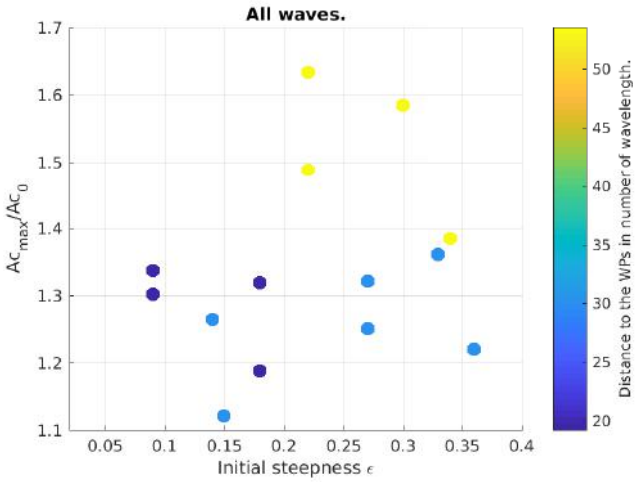

Figure 4.3: Maximum ratio S measured at CWS over mean wave steepness at WP1.

The maximum values of the ratio $S = Ac_{max}/mean(Ac_0)$ were found for initial wave steepness $0.2 < a_0k_0 < 0.3$. As pointed out by Su and Green 1984 [8] the growth rate of both instability class I and II is small for small a_0k_0, and about equal

to the growth rate for both the first and second type when $a_0k_0 \approx 0.26$. So, this amplification could be explained by both first and second type of instability having compatible growth rate.

Figures 4.4 a,b,c compare wave records with $a_0k_0 = 0.14$ (right, $H = 5$ cm and $T = 0.8$ s) and $a_0k_0 = 0.26$ (left, $H = 5$ cm $T = 0.6$ s).

In Figure 4.4a, individual lines correspond to subsequent individual wave crests as they arrive at the cross-array CWS WP4-WP12 (note that this is a simultaneous measurement at WP4 to WP12 probes), and Figure 4.4b shows their interpolated time evolution at CWS. Difference in the magnitude of the cross-modulational for the two cases is clearly demonstrated.

The reason for the apparent strong amplification of the cross-modulational at $\epsilon = 0.26$ is analyzed in Figure 4.4c. Here, heights of subsequent waves crests at probes WP1, WP2, WP3 and WP8, i.e. along the tank, are plotted. The wave train with mean steepness around $a_0k_0 = 0.26$ develops a strong modulation and the values of R reach values higher than 1.5. This modulational is seen at WP3 and grows significantly towards CWS. When the maximum crest steepness is still relatively low at WP3, the long-tank modulational is also seen (black triangles in Figure 4.4c(left)), but it forms longer groups. These are typical features for wave trains subject to Benjamin-Feir (BF) instability (e.g. [28]). Explicitly, sideband growth of such instability for our record is shown in Figure 4.5a (see e.g. [21] for the expected sideband behavior). It should be mentioned that the large undulations in Figures 4.4a and 4.4c (right) are the propagating front of the new wave group, and have no physical meaning in the context of the current paper.

Thus, it appears that magnitudes of modulational along the wave propagation (due to BF instability) and crest modulational across the propagation direction are connected. The latter reaches maximum in Figure 4.2, once the former reaches maximum in Figure 4.4. The maximal wave height caused by BF mechanism is reached faster for steeper waves (e.g. [28], and after it is reached the maximal wave height subsides either due to breaking or due to recurrence of the wave train to its original uniform shape (e.g. [16]). This may be reason for waves with $\epsilon = 0.31$ in Figure 4.2 having a smaller cross-modulational ratio R, but note that in this case Type II instability is also strong [15]

Figures 4.5b, c are an attempt to quantify properties of the cross-modulational, with respect to properties of the propagating wave train.

Since the cross-array only consists of 9 wave probes, its spatial resolution is low and the comparison of cross- and long-wave scales is only approximate. Figure 4.5b presents an instantaneous (no time averaging) one-dimensional spatial power spectrum based on Fourier Transform of the space series of 9 probes evenly distributed over the 8m distance of the CWS array (i.e. in the transversal direction over the

1-D segment covered by CWS), with Blackman-Harris window used. Based on the spatial spectrum of cross-modulational for incoming waves with 1 m wavelength L (L was calculated from the dispersion relationship in deep water, $L \approx gT^2/2\pi$, g is the constant of gravity.) (Figure 4.5b), we can conclude that the cross-modulational scale λ_b is between 1.3 m and 2 m ($2.3 \geq \lambda_b/L_0 \leq 4$). Note that this wavelength is much smaller than the longest transverse standing mode which was discussed by [29] and would be 60 m in our case. Since it is apparently a result of nonlinear wave behavior, it can be expected that this scale may depend on steepness of the individual wave crests as the main indicator of the nonlinearity. Indeed, as it can be seen in Figure 4.5c, ratio of the cross-scale λ_b to wavelength L is between 1 and 7 for low-steepness wave trains and is between 2 and 4 for higher steepness. [13] and [29], in similar terms, discussed conditions for Type I and Type II instabilities to trigger the transversal modulational. These conditions are plotted in Figure 4.5c (dashed and solid lines, respectively).

4.4 Summary of the results

This chapter presents an experimental investigation of lateral modulational of long-crested mechanically-generated waves. In this experiment, attempt is made to quantify properties of the lateral wave modulational. Minimal ratio of the maxima and minima across the modulated long wave crests is 1.1, while the maximum ratio can be as large as 4. Length of the lateral modulation ranges from being comparable with the wavelength to being four times the wavelength of carrier wave, depending on the steepness. The results presented above in this chapter were also published in Pinho and Babanin [26]. When comparing the maximum wave crest measured at the cross section CSW with the mean initial crest measured at WP1, the maximum ratio $S = Ac_{max}/mean(Ac_0)$ measured was $S \approx 1.7$ and this maximum occurred when the carrier waves were in the range $0.2 < \epsilon_0 < 0.3$ and have propagated over 45 wave cycles from the wavemaker to the wave probe where were measured.

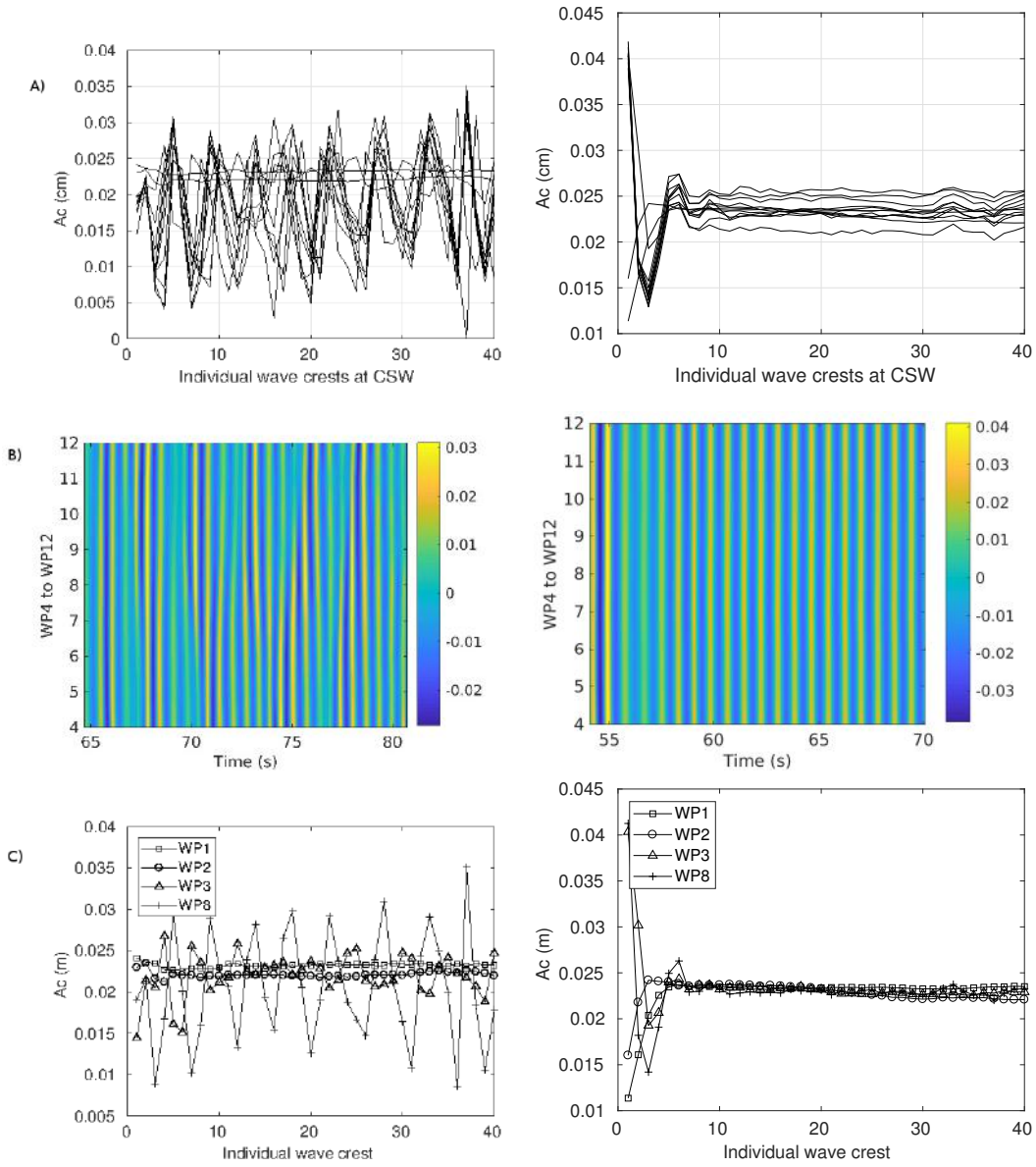

Figure 4.4: An unstable wave set on the left ($H = 5$ cm and $T = 0.6$ s) is compared to a stable set on the right ($H = 5$ cm $T = 0.8$ s). Horizontal axes in Figures 4.4a and 4.4c represents time in terms of incoming individual wave crests measured at the WP's. Vertical axis in Figure 4.4b is distance in terms of WP numbers in the CWS array (see Figure 4.1). (a) Time series of subsequent crest heights, as measured by probes WP 4-12 of CWS. (b) Contour plots of time evolution (horiz. axis is in sec) of water surface elevation measured at CWS. Vertical scale is in probe numbers (WP 4-12). (c) Time series of the wave crests amplitude at four WP's along the tank. WP1 is the closest to the wave maker and WP8 is the farthest (close to the beach) as shown at Figure 4.1

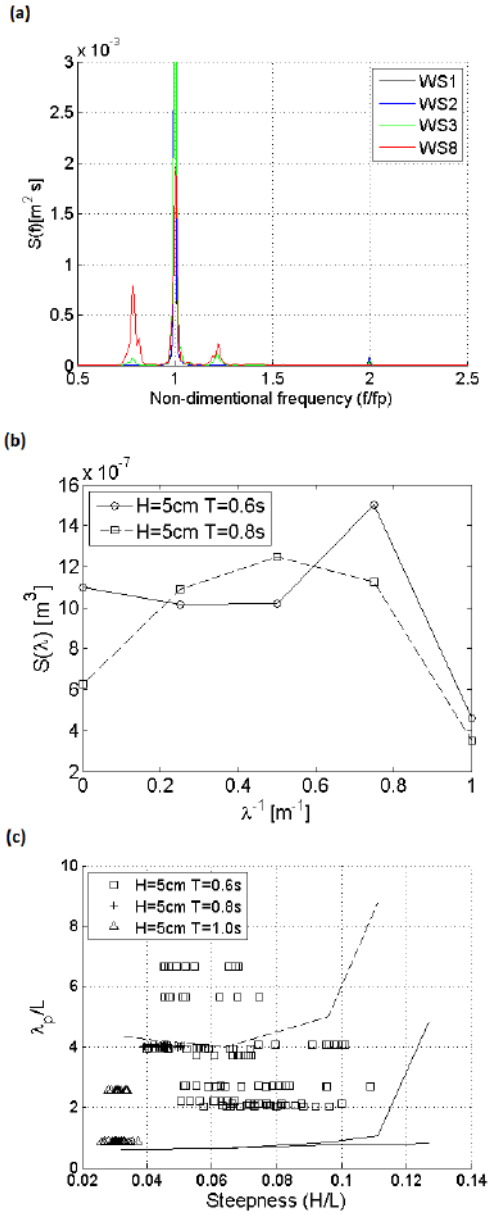

Figure 4.5: Growth of sidebands for the wave train in Figure 4.4b(left), the frequency axis is normalized by the peak frequency 1.667 Hz ($f_1 = 1/0.6$ s). (b) Spatial spectrum of the cross-modulational. Solid line with circles corresponds to $H = 5$ cm $T = 0.6$ s and dashed line with squares to $H = 5$ cm T=0.8 s (c) Ratio of the cross-wave modulational λ_b to the wavelength, for different steepnesses. Symbols are as shown in the caption, dashed and solid lines indicate regions of Type I and Type II maximal instability

Chapter 5

Transversal Modulation and Sidebands Growth on Modulated Nonlinear Wave Trains

5.1 Introduction

When finite amplitude monochromatic steep water waves are generated in a deep water wave tank, it is well known that due to the nonlinear character of such waves, they become unstable due to small background random perturbations in the media [3]. In order to study such effect, a set of two experiments in which initially monochromatic finite amplitude wave trains were generated mechanically with a wide range of wave steepnesses and the evolution along a large wave tank was observed and recorded by 32 wave probes.

This chapter presents the results of the second experiment. The new experiment was conceived to cover some details that were not possible to address in the previous one, due to either a lack of data or a lack of spatial coverage. In this new test, a set of two cross-arrays, each of them with 15 wave probes and 1 meter between wave probes was used, instead of the single cross-array with 8 wave probes, 0.5 meters apart, used in the first test. A detailed description of the new experiment is given in the next section.

5.2 The experiment

The second experiment at LabOceano (section 3.1) was planned to provide more details on the major topics on the modulational instability addressed on the first test. Compared to the first test, more cases (each case composed typically by one hundreds of individual waves) were generated and the number of wave probes was

doubled regarding the first experiment. It also included a second transverse section of wave probes closer to the wavemaker.

Differently of the first experiment, in order to avoid the discontinuity caused between the corner of the wavemaker at one side of the wave tank (upper right side in Figure 5.1) and a lateral beach on the same side, it was decided to use only the half of the tank where there is a vertical wall instead of a lateral beach. This way, small perturbations generated by the wavemaker corner would be negligible at the points of measurements. However, all waves were generated along the whole extension of the wavemakers on the full width of the tank, not only on the half side where the wave probes were positioned.

Figure 5.1 shows the position of the 32 wave probes in the wave tank. The first wave probe (WP1) was placed at a distance of 7.5 m from the wavemaker in order to avoid possible transients caused by mechanical paddles. It was followed by wave gauges placed at 15 m, 22.5 m and 30 m from the wavemaker.

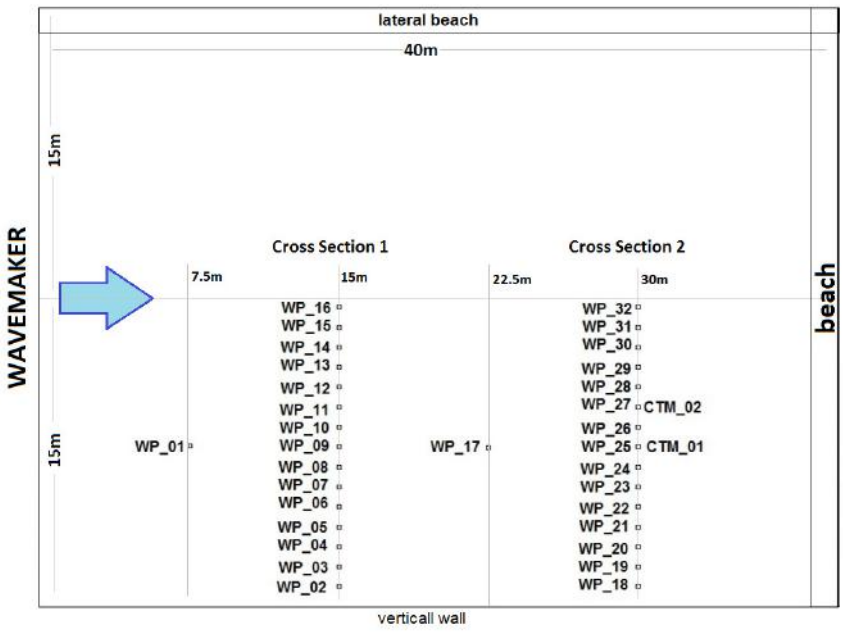

Figure 5.1: Wave probe layout. Black dots are locations of the probes. Two transversal sections of wave probes were placed at 15m and 30m from the wavemaker.

Two sets of wave probes were positioned transversally to the wave propagation at 15 m and 30 m from the wavemaker, named Cross Section 1 (CS1) and Cross Section 2 (CS2), respectively. The distance between consecutive wave probes in CS1 and CS2 was 1 m, so that the total length of each coss section was 15 m. The data was continuously sampled by the 32 wave probes with a 60 Hz sample rate.

The experiment consists of generating a large number of sinusoidal deep water waves with wave heights ($H = 2a$, where a is the wave amplitude) ranging from 0.05

m to 0.10 m and wavelengths (L_0) of 0.56 m ($T = 0.6$ s), 0.76 m ($T = 0.7$ s), 1.0 m ($T = 0.8$ s), 1.26 m ($T = 0.9$ s), 1.56 m ($T = 1.0$ s), 2.25 m ($T = 1.2$ s) and 3.1 m ($T = 1.4$ s) and steepnesses ranging from $\epsilon = 0.05$ to $\epsilon = 0.41$. All waves can be regarded as deep water waves, since the tank depth is $h = 15m$ and $20 \leq k_0 h \leq 111$, so that $k_0 h \gg 1$. The significant parameters of the generated waves are listed in Table 5.1.

Table 5.1: Waves generated: The values in the table corresponds to the steepness values.

H \ T	**0.6s** 1.67Hz	**0.7s** 1.43Hz	**0.8s** 1.25Hz	**0.9s** 1.11Hz	**1.0s** 1.0Hz	**1.2s** 0.83Hz	**1.4s** 0.71Hz
5cm	0.28	0.21	0.16	0.12	0.10	0.07	0.05
7cm	0.39	0.29	0.22	0.17	0.14	0.10	0.07
8 cm	–	0.33	0.25	0.20	0.16	0.11	0.08
9 cm	–	0.37	0.28	0.22	0.18	0.13	0.09
10 cm	–	0.41	0.31	0.25	0.20	0.14	0.10

The wavemaker was programmed to generate waves during approximately 3 minutes (180s). When the leading waves reached the end of the tank, the wave maker was turned off, a 10 minutes of rest of interval was taken, in order to allow the water to become still again before the next wave generation. Each set of waves will be called "case".

Denoting by D as the distance from the wavemaker to wave probes, the possible maximum values of D/L_0 (L_0 is the initial wavelength at WP1) for the wave probes at CS2 (at $D = 30$m), are accordingly with the initial wave periods: 53.4 ($T = 0.6$ s), 39.2 ($T = 0.7$ s), 30.0 ($T = 0.8$ s), 23.7 ($T = 0.9$ s), 19.2 ($T = 1$ s), 13.4 ($T = 1.2$ s) and 9.8 ($T = 1.4$ s), considering $L_0 \approx 1.56T^2$ from linear wave theory.

5.3 Results

5.3.1 Crest transversal deformation by modulational instability: Ratio $R = Ac_{max}/Ac_{min}$

Initially long-crested finite amplitude waves mechanically generated propagate freely from the wavemaker with small or no change on their main characteristics as wave period, height, amplitude for a few wave cycles. However, due to nonlinear effects, the long and flat crest observed close to the wavemaker becomes irregular as the waves propagate away from the generation area. The modulational instability on

such waves can be quantified by observing the crest deformation as the waves propagate along the tank.

One of the first and more remarkable features of the long-crested wave transformation when they become modulated by nonlinear effects is the wave crest bending, or waving. It can be quantified by comparing the highest point measured in the cross-section with the lowest point in the same cross section (or the same wave phase). Because of that, the first results presented in the previous chapter (4.3) were an attempt to quantify the lateral modulational instability by calculating the ratio $R = Ac_{max}/Ac_{min}$ (where the maximum crest is denoted by Ac_{max} and the minimum by Ac_{min}) values measured along the cross-tank array (CWP) were plotted against the initial mean steepness at WP1 in Figure 4.2.

In the second experiment, initially, along CS1 (just a few wavelengths from the generation point), the waves were expected to be weakly modulated, so that the crests were almost flat and $R \approx 1$. For higher the wave steepness of the initial wave, a higher modulation is expected as it propagates away from the wavemaker. So, the farther the waves traveled from the wavemaker, more wave cycles would be covered and stronger the nonlinear effects would be acting on the waves and $R \gg 1$ is expected. On the other hand, for small steepness linear waves, not much deformation was expected along the wave propagation toward the end of the wave tank and values of the ratio R measured either close to the wavemaker or farther (close to the beach) are expected to be close to 1.

Lower values of wave steepness are mostly related to large values of wave periods (top right of Table 5.1). This means that these waves have longer wavelengths and, consequently, a smaller number of wave cycles as compared to the waves with short periods (wavelengths), i.e., these waves travel less cycles from the wavemaker to the wave probes than shorter ones.

At the wave probes closer to the wavemaker, most of the waves didn't propagate enough to become laterally modulated and the majority of the values of R are closer to 1, meaning that the crests are almost uniform (the maximum and minimum values of wave amplitude at the crest are very similar in magnitude).

It is clear that the farther the waves travel, the larger is the crest deformation (see the spread of points on right hand side of Figure 5.2). This can be also related to the short-crestedness behavior (directionality) of steep waves as they propagate enough distance from the source, as shown in the previous chapter.

It is important to notice that in Figure 5.2, instead of plotting all waves, it was decided to neglect waves that became too modulated laterally (short crested) along their path. This decision was based on the fact that waves strongly modulated after breaking events were no longer long-crested, rather they became mostly random and short-crested. It means that when calculating R, it could lead to values as high as

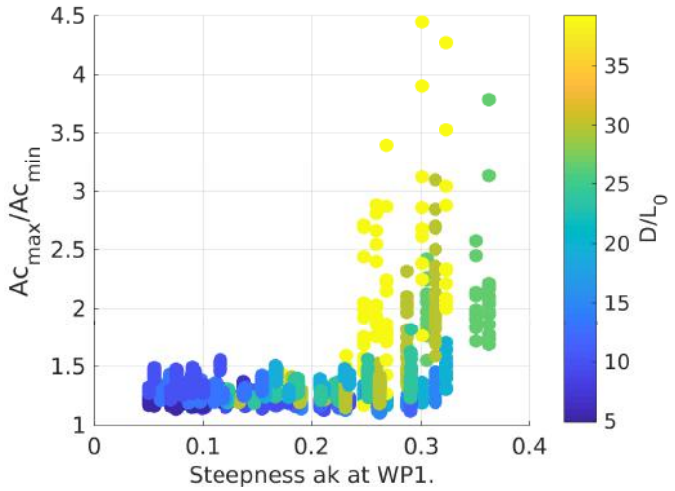

Figure 5.2: Ratio between maximum to the minimum values of wave amplitude ($R = Ac_{max}/Ac_{min}$) measured at CS1 and CS2.

$R > 100$, since the minimum value of wave crest may become close to zero (mean water level). Only waves with $R < 5$ (on the previous test presented in chapter 4, the maximum value found for R was 4) were plotted. This restriction discards less than 3% of the total data set (values).

Through the high quality videos acquired during the experiment, it was possible to identify cases where breaking events occurred widespread when short waves with high steepnesses propagate for a long distance ($D/L_0 > 30$) and then the waves became extremely short-crested (5.3).

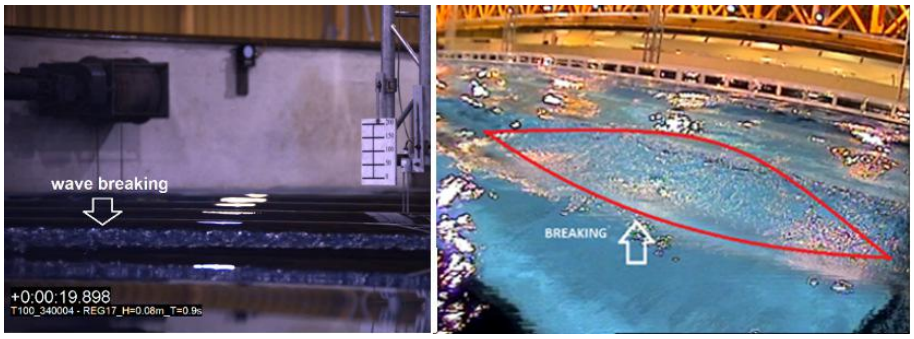

Figure 5.3: Breaking waves images taken by the video cameras during the test.

It is possible to observe what happens with the shorter and steeper waves as they propagate along the wave tank, by comparing contour plots of the water elevation along CS1 and CS2 (Figure 5.4). As a matter of illustration, it was chosen to take the same case as shown in Figure 5.3, i.e., a case where breaking events happened. Waves were generated long-crested, with a periods of 0.6 s, wave heights of 0.04 m and wavelengths estimated by linear theory of 0.56 m. The initial wave steepness at

WP1 was $\epsilon_0 = 0.22$. Although these waves were long-crested when passing through CS1, they completely changed their shape when reached CS2. Their crests became short and the wave height was not constant along CS2 (Figure 5.4).

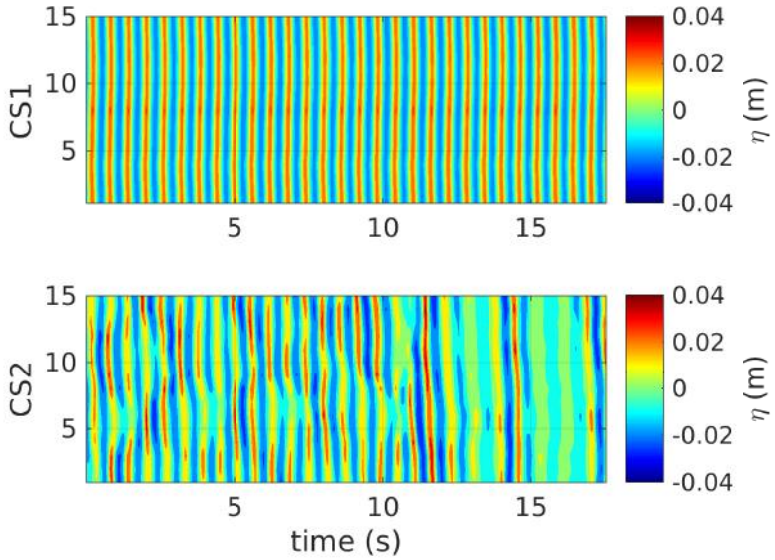

Figure 5.4: Contour of the water surface elevation. Axis y represent the number of the wave probes on CS1 and CS2. ($\epsilon = 0.22$

Figure 5.2 shows also that the waves were modulated even for low values of initial wave steepness (the left side of both figures), the values of R were significantly higher than 1. Waves with low steepness were still modulated while propagating from the generation zone and at a wave steepness of $\epsilon_0 = 0.1$ they reached values of $R < 1.4$ at CS1 and at CS2 reached values close to $R = 1.6$.

Therefore, when the waves become very modulated, after propagating enough wave cycles, they are already short-crested and bi-dimensional and R values could become meaningless. At the same phase (in this case, at the crest) one value of the crest could be numerically close to zero (i.e., close to still water level) and as high as about the double of the initial wave height at the generation (see Figure 5.7b). In order to illustrate one of these discarded cases, by plotting these individual maximum and minimum wave crest values one against the other, this trend becomes more clear (Figure 5.5).

The red line in Figure 5.5 represents the line for values $Ac_{max} = Ac_{min}$ or $R = 1$ and in this experiment, the values of R were always greater than 1 at CS1 and CS2; however, it was close to the unity for waves with low steepness ϵ_0. On the left hand side of the Figure it is possible to notice values of Ac_{min} close to zero (still water level), while the values of Ac_{max} remain positive and ranging from $0.02 < Ac_{max} < 0.07$, which makes R reach very high values.

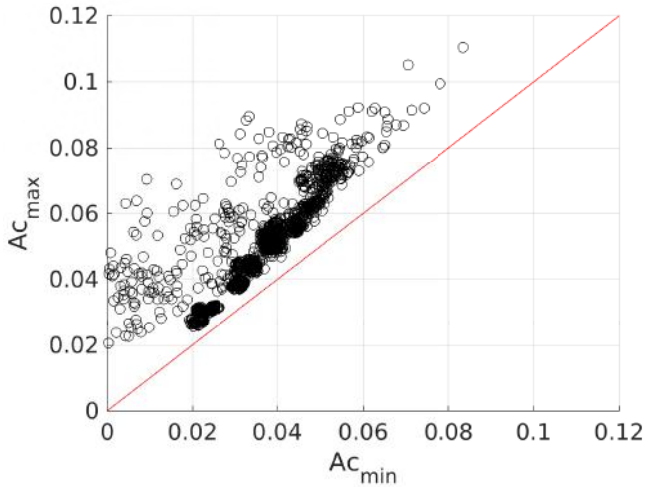

Figure 5.5: Maximum values of wave amplitude (Ac_{max}) compared to the minimum wave amplitude (Ac_{min}) measured on the CS1 and CS2.

5.3.2 Crest transformation along the wave train propagation: Ratio $S = Ac_{max}/Ac_0$

As a matter of finding how much directionality and deformation of the crests was observed along the waves propagation, in Figure 5.6 we compute the ratio between the maximum wave amplitude measured at WP25 (CS2) and the mean amplitude measured at WP1. In this figure, all 84 cases generated in the second experiment (the circles in the figure) are shown along with the cases from the first test presented in chapter 4 (shown as triangles). The results found in both experiments agree very well despite the two odd points (the triangles), with low $S = Ac_{max}/Ac_0$ in the interval $0.25 < \epsilon_0 < 0.3$ [1].

As shown in Figure 4.2, for values of wave steepness $\epsilon_0 \approx 0.26$ a wider spreading of the ratio S can be observed. On the other hand, by analyzing Figure 5.6, one can note that for $\epsilon_0 \approx 0.26$, the ratio S reaches its maximum value of $S \approx 2$. Su and Green (1984) [8], showed that the associated growth rate in the modulational instability type I and type II are about equal when $\epsilon_0 \approx 0.26$, summing up the effects of nonlinearity and what may explain our results indicating a maxima at this values. Also, as pointed out by Su and Green (1984) [8], the range of wave steepnesses at the sea is mostly in the range $0.12 < \epsilon < 0.20$. So, according to the Figure 5.6, most of the waves at sea would lie in the region of low modulational instability, where $R < 1.4$.

Su and Green (1984) [8] compares the maximum amplitude of the modulation, denoted by them as a_m (calculated from the power spectra of the water surface

[1] (note that $S = Ac_{max}/Ac_0$ and $R = Ac_{max}/Ac_{min}$

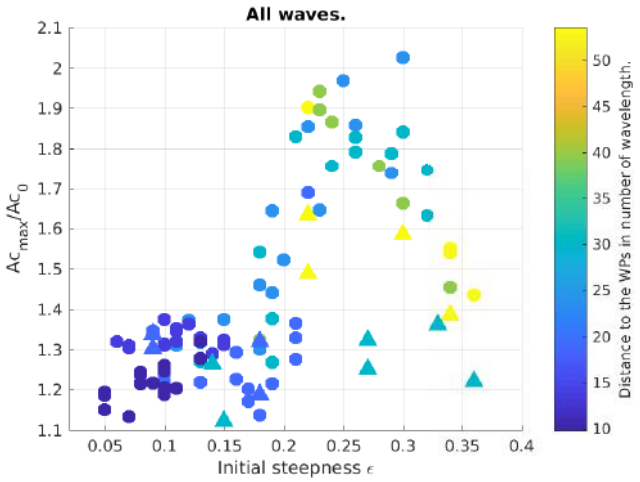

Figure 5.6: Ratio between maximum wave amplitude (Ac_{max}), measured on CS2 (WP18-WP32) and average wave amplitude at WP1 Ac_0, shown as circles, while the results from test 1 (Figure 4.3) are shown as triangles. The colorbar indicates the distance in wavelengths to the wavemaker.

displacement time series) with initial amplitude Ac_0. They found that there is a rapid increase of a_m/Ac_0 for $\epsilon < 0.14$ corresponding to type I modulation (Figure 5 of [8]) and they reported that for values of $\epsilon > 0.12$, type II modulation grow rapidly and suppress type I. Note that in Figure 5.6, however, it is shown the maximum crest measured (Ac_{max}), not the maximum amplitude modulation a_m, as presented in Su and Green (1984) [8], but the peak of the distribution of values of Ac_{max}/Ac_0 can also be seen in the range of $\epsilon = 0.05 - 0.2$, in agreement with value of $\epsilon = 0.14$ found by Su and Green (1984) [8], indicating direct relationship between higher values of the amplitude modulation and high wave crest Ac values. In the cases where the initial wave steepness was $\epsilon_0 < 0.15$, the ratio S is low (between 1.1 and 1.4) indicating no significant modulation. When $0.20 < \epsilon_0 < 0.25$, the ratio S varies $1.4 < S < 2.0$, indicating strong modulation and for $\epsilon_0 > 0.26$, S decreases, possibly because of breaking events.

In Figure 5.7, it is shown the evolution of ratio S along the two cross-tank sections CS1 and CS2. For a specific case, in order to illustrate the effect of directionality noted in most cases where modulation effects were relevant. At section CS1, the waves propagated fewer cycles and the maximum values of S were close to unity, as shown in Figure 5.7a where the waves at CS1 have crests relatively uniform. However, at CS2, the waves became short-crested and irregular. Therefore, most of the irregularities and directionality along the wave propagation is due to the modulation as a result of more cycles of nonlinear interactions.

In CS1 (5.7a) the ratio between the individual wave crests over the mean crest on WP1 ranged between 1 and 1.4, while in CS2 this ratio ranged between just

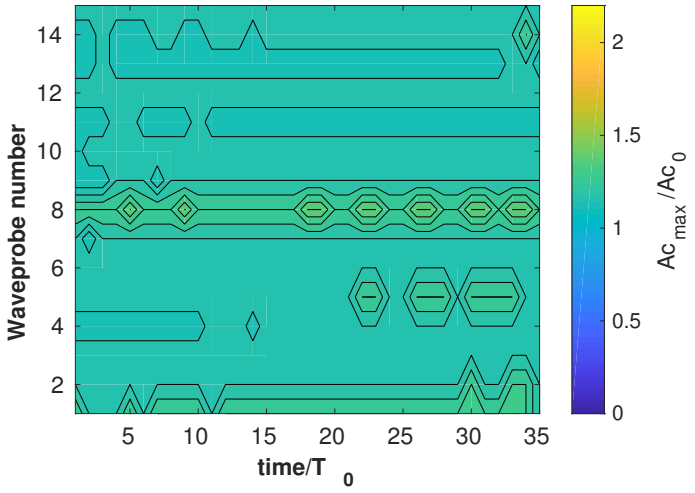

(a) Cross section 1.

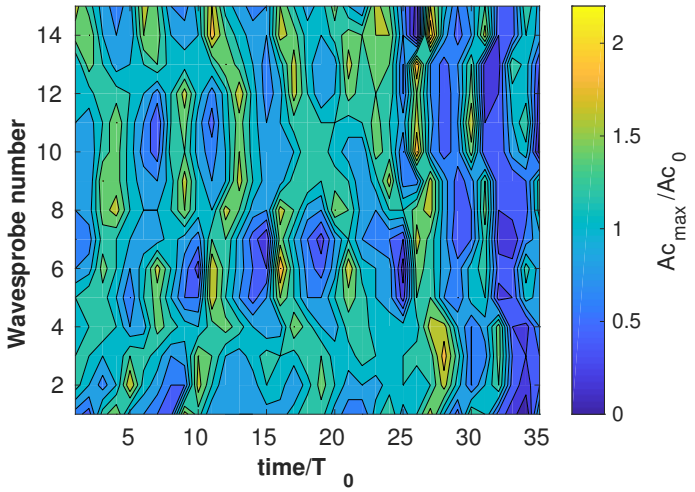

(b) Cross section 2.

Figure 5.7: Contour of the maximum wave amplitude measured per wave cycle in each WP of the CS1 and CS2, divided by the mean wave amplitude on the control wave probe 1 (WP1), T_0 is the wave period of the carrier wave measured at WP1.

above zero to values as high as over 2.0. It is also possible to see that at the same phase (cycle) on CS2 (any vertical line on Figure 5.7a is in the same phase), the range of the values went from close to zero to higher than 2. This means that due to nonlinearity only (no other sources of energy input in the system as wind and currents), waves initially having all about the same normalized crest S could reach now crests as high as two times the initial one and also as low as the mean water level, indicating short-crestedness characteristics.

5.4 Transversal modulation- λ_b

In order to quantify the crests' transformation in the transversal direction to the main direction of propagation, while the waves travel along the tank, the spatial spectrum of the water elevation was calculated for every instant along CS1 and CS2 (5.1). From the spatial wave spectra, the lateral wavelength λ_b can be estimated.

The spatial spectra was calculated by taking water surface elevation (η) values at every time interval of measurement in all 15 wave probes of CS1 and CS2. Therefore, from these 15 points one spatial spectra was calculated (the sample frequency was 60Hz, so 60 spatial spectra every second).

As an example, Figure 5.8 shows the evolution of the spatial spectrum for a specific case. The maximum energy of the spectrum is not stationary in time and the peak of energy of the lateral spectrum varies changing the peak wavenumber.

By calculating the momentum of order zero (i.e. sum of the energies in all wavenumbers, or the vertical lines in Figure 5.8 for every instant), represented by the following expression:

$$\sum_{k=0}^{k_1} S_{spat} = m_0$$

where S_{spat} is the spatial spectra and comparing to the water surface elevation (Figure 5.9), it can be seen that the most energetic spatial (lateral) spectra taken at CS2 is almost in phase with the water surface elevation η, matching with the crests of the waves. It means that the bending, or the modulation, of the water surface occurs mostly at the crest, but it can be seen happening at the trough as well. In other words, the crest and troughs seems to be more wavy laterally than other wave phases of the waves.

To quantify the lateral modulation and to measure the lateral wavelength of the modulation, the lateral spectrum for each crest was calculated and then the peak wavenumber of the spatial spectra was used to calculate the lateral wavelength (λ_b).

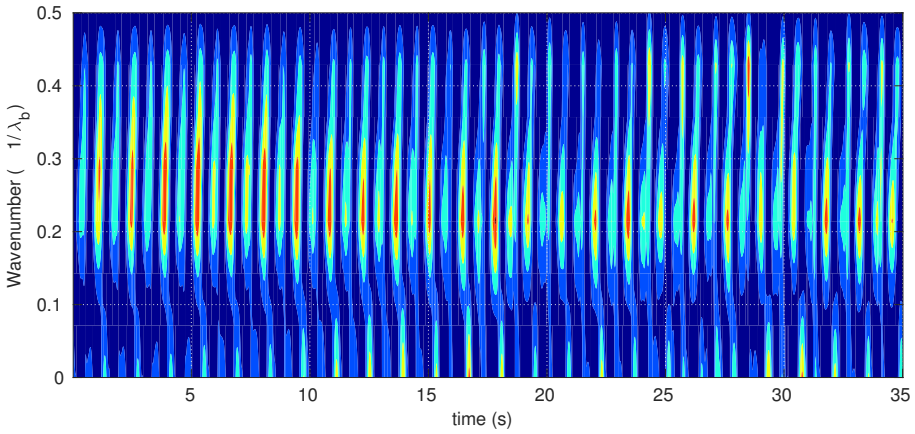

Figure 5.8: Spatial spectrum calculated for every instant of the time series calculated at CS2.

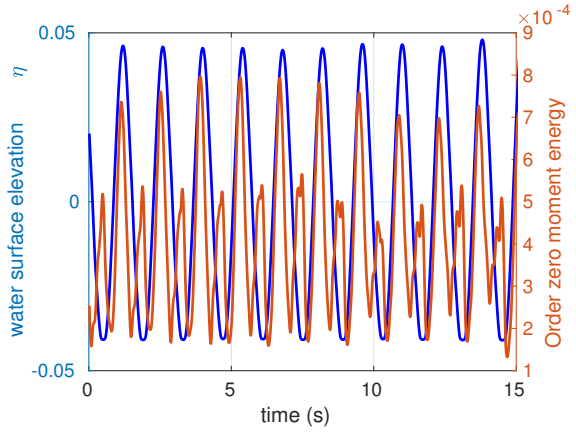

Figure 5.9: Time series of the water surface elevation, η and zero order momentum of the lateral spectrum.

5.4.1 λ_b/L_0 as a function of ϵ

The modulational instability is a direct function of the degree of nonlinearity of the waves which is dependent of the wave steepness. The relationship between the lateral modulation wavelength, normalized by the initial wavelength of the main carrier in the main direction of the wave train propagation is analyzed next. The values of the normalized lateral (or transversal) wavelength of the modulation λ_b/L_0 relative to the initial wave steepness ϵ at CS1 and CS2 are shown on Figure 5.10.

The values found for λ_b/L_0 at CS1 were very spread over the range of $\lambda_b/L_0 = 1.5 - 18$, with a trend to be higher for higher values of steepness. Most the values however were concentrated on the range from $\lambda_b/L_0 = 1.5 - 2.5$, specially for low values of initial wave steepness (x axis), which is in agreement with the results found in the first experiment, presented in Chapter 4.

At CS2 the same general pattern found in CS1 can be observed, but much less

spreading and a much more defined trend for high values of initial wave steepness resulting in higher values of λ_b/L_0. It can be noticed that for values from $\epsilon = 0.05$ to values just above $\epsilon > 0.2$ the values of λ_b/L_0 stays in the range $\lambda_b/L_0 = 1.5 - 4$, also in agreement with the results found in Chapter 4.

Melville 1982 [18] also found the predominant wavelength of the transversal perturbation about two primary wavelength, but for initial wave steepness $\epsilon > 3.1$ and cited that for that values of wave steepness the three-dimensional effects appeared to dominate the Benjamin-Feir instability. Brandini, 2002 [30] carried out numerical modelling simulations using Higher Order Spectral (HOS) model and a three-dimensional (3D) fully nonlinear Numerical Wave Tank (NWT), found also

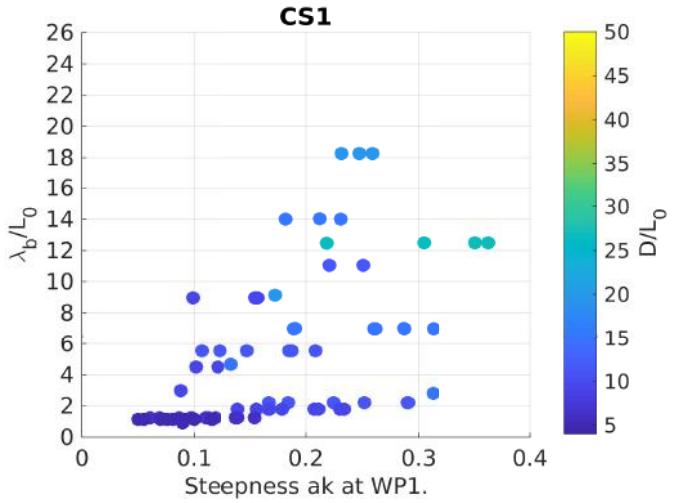

(a) λ_b/L_0 calculated at cross section 1.

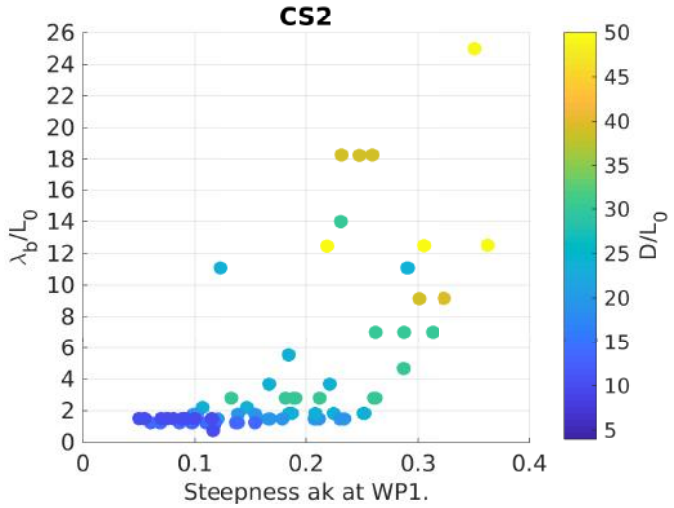

(b) λ_b/L_0 calculated at cross section 2.

Figure 5.10: Lateral modulational instability λ_b/L_0 calculated in two cross sections along the tank, CS1 and CS2 (see 5.1).

$\lambda_b/L_0 = 2$.

As mentioned previously in this chapter, for low values of initial wave steepness one could expect relatively longer wavelengths of the transversal perturbations since the crest are intended to be mostly flat close to the wavemaker, but it was not seen in the results found for both CS1 and CS2, but the values of λ_b/L_0 were mostly in the range $\lambda_b/L_0 \approx 2$, as cited above.

It is important to point out that since the crest is very weakly perturbed close to the wavemaker, as well as for small values of initial wave steepness or, in other words, small values of ratio R, the energy of the lateral spectra is up to three orders smaller than the energy of lateral spatial spectra for higher values of initial wave steepness. It can be easily seen at Figure 5.11, along with Figures 5.2 and 5.6, that there is one regime of transversal energy and related perturbation amplitude at low wave steepnesses ($0.05 < \epsilon < 0.2$) and other one for higher initial wave steepnesses ($\epsilon > 0.2$). These two regimes are manifests of McLean type I and II instability ([13], [15] and [31]), or as pointed out Melville 1982 ([18]), Benjamin-Feir instability up to wave steepness values of ($\epsilon \approx 0.2$) and bi-dimensional (three-dimensional as referring to x, y and z dimensions, we chose refer it as bi-dimensional x and y) instability for values higher than that. Melville actually found that Benjamin-Feir instability was present at values of $\epsilon < 0.29$ and bi-dimensional for $\epsilon > 0.31$.

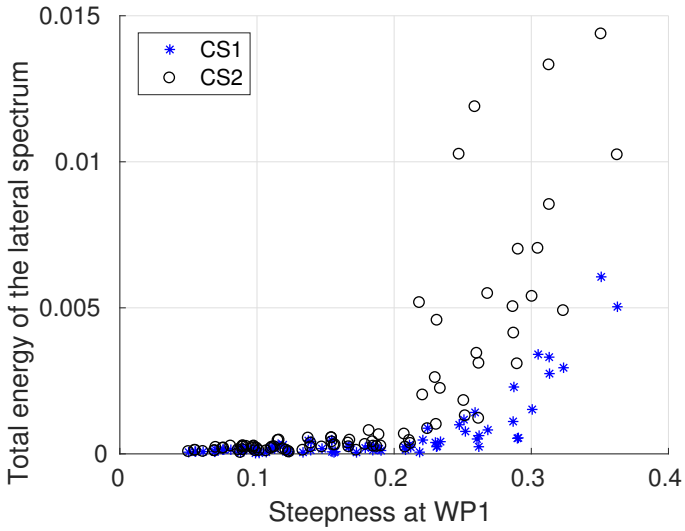

Figure 5.11: Total energy of the transversal spatial spectra vs. initial wave steepness.

By plotting Figure 5.11 with y axis in logarithm scale we obtain 5.12, which is easier to observe the exponential growth of the total energy of the lateral spectra as the values of wave steepness increases. For the whole range of wave steepness the energy at CS1 is one or two orders lower than at CS2, specially above wave steepness values corresponding to $\epsilon > 0.2$.

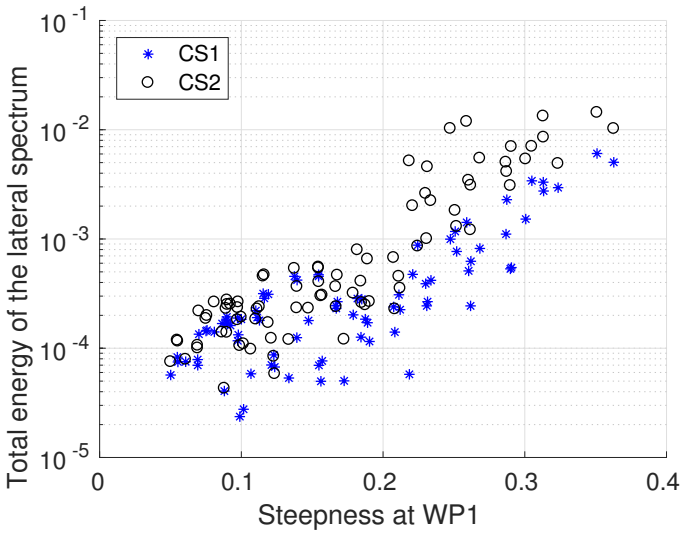

Figure 5.12: Total energy of the transversal spatial spectra vs. initial wave steepness.

The rapidly increase of wave energy for wave steepness above 0.2 is also related with short-crestedness, since high crests and low crests are in phase (as we will see below), so the amplitudes of the harmonics of the lateral wave spectra are also higher when compared with relatively flat crests found for low values of wave steepness ($\epsilon < 0.2$).

5.5 Sidebands Evolution on Modulated Nonlinear Waves

5.5.1 Introduction

As demonstrated by Benjamin and Feir [3], weakly nonlinear periodic wave train with initially uniform, finite amplitude is unstable to infinitesimal periodic sideband frequency in the range $0 < \delta \leq 2^{1/2}ka$, where $\delta = \Delta f / f_0$ measures the frequency separation of the side-band and the fundamental components. In the wave energy spectrum, those frequencies appear as "sidebands", on both sides of the carrier wave frequency. In a wave tank, close to the wavemaker, the perturbations have infinitesimal energy in the wave spectrum, but as the waves propagate further along the wave tank, it is possible to detect an exponential growth of the sidebands at a rate that follows an expression found in equations 2.9 and 2.13. A graphical interpretation of the relationships between the normalized frequency of the sideband, its energy (curves of growth) and steepness are shown in Figure 1 of Tulin and Waseda [21], showing the initial growth rate (named by them as β_x) of the sideband disturbance, based on Krasitskii's reduced four-wave interaction equation (Krasitskii

[32]).

Lake $ Yuen [20] performed a controlled laboratory experiment comparing the characteristics of the evolution of the nonlinear wave train with the numerical solution of the nonlinear Schrödinger equation. The results indicated that the growth rate required a correction of the Nonlinear Schrödinger Equation (NSE). Dyshe [33] derived a correction term for the NSE, in a way to be valid for a broader bandwidth, but the steepness range was still limited to $\epsilon < 0.01$. Krasitskii [32] improved some calculations on Zakharov's integral equation [4] and derived a very useful expression for the sidebands' growth rate calculation. Benjamin and Feir (1967) [3] have shown that the sidebands grow as a function of the initial wave steepness $\epsilon = a_0 k_0$. It is easy to find a range for the largest growth rate for a given wave steepness ϵ. Tulin and Waseda [21] used this range to plan their experiment to address the full evolution of the nonlinear waves. The major outcomes of the experiment: *an increase of the energy in the lower sideband relative to the upper sideband as the peak modulational is approached, followed by the disappearance of that difference in energies as recurrence progresses.*

As mentioned in chapter 3, in the experiments presented in this thesis, no perturbations were introduced in the wave generation on the wavemaker, so that the sidebands grew from initially small background perturbations. Following the nomenclature used by Tulin and Waseda [21], it can be called an *unseeded* experiment.

In the following section, it will be shown quantitatively that the growth of the sidebands are related with some wave parameters, such as wave steepness. The evolution of the sidebands along the tank was quantified from a spectral analysis of the time series of η obtained from the wave probes along the main direction of wave propagation. Figure 5.13 summarizes the spatial analysis: Figure 5.13a shows the space distribution of the wave probes on the tank; Figure 5.13b shows the time series of the surface elevation at different wave probes along the tank indicated by the red ovals on 5.13a; the red part of the time series (Figure 5.13b) indicates the range where the spectral analysis was carried out.

This chunk of the time series was selected to avoid the wave front transients. In order to take approximately the same wave train (energy) in elevation time series measured in different wave probes along the tank (different distances from the wavemaker), the group velocity was estimated from linear wave theory ($C_g = c_0/2$, where c_0 is the phase velocity in deep water, $c_0 = gT_0/(2\pi)$ and T_0 the initial wave period). The right bottom panel (Figure 5.13c) shows the energy spectrum of the time series on Figure 5.13b using only the η time series in red.

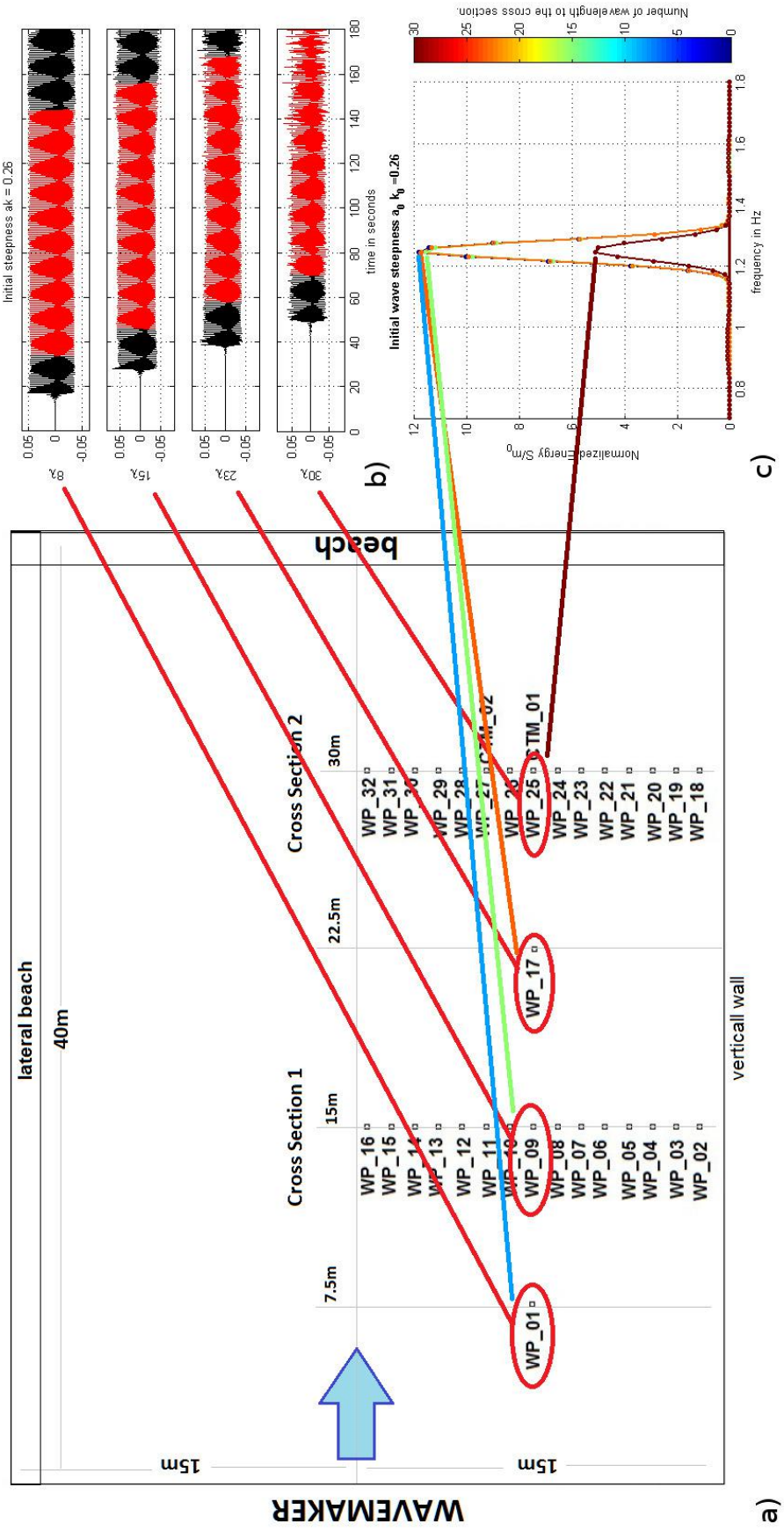

Figure 5.13: Time series point (WP) of measurement and wave spectra.

Sidebands Growth: Data analysis

The growth of the sideband perturbations was estimated by calculating spectrum of surface elevation time series along the wave tank, in the direction of the carrier wave propagation, by using the waveprobes WP1, WP9, WP17 and WP25 (Figure 5.13). The two dimensions were defined as following: y is the along crest dimension (axis) and by x the wave propagation direction axis, so that the initial wavenumber vector, $\mathbf{k_0}$, points in the x direction.

For each case, the water surface elevation was measured for three minutes (or 180 seconds), at each wave probe in order to avoid the transient wave front caused when the wave train is generated in a still water environment [34].

The spectral analysis was made taking the mean of all wave probes on the CS1 (WP2-WP16) and CS2 (WP18-WP32) (see Figure 5.1) and measurements on WP1 and WP17. The reason for taking the mean of all wave probes along the sets of 15 wave probes of CS1 and CS2 (instead of using the measurements on the central wave probes of the cross sections, WP8 and WP25) will be discussed in the next section.

Sideband Growth: Measurements

In the next sessions it will be presented the evolution of the sidebands in terms of growth rate of energy and frequency shift along the wave tank and its dependence on the wave steepness. To illustrate some specific features presented in the next sessions, it was decided to focus on 14 representative cases out of the total of 84 cases, where the initial wave steepness and distance traveled from the wavemaker were sufficient to make the sidebands grow enough to allow a quantitative study. Its wave steepness were in the range $0.22 < \epsilon < 0.34$ and, as seen in the previous sections, high nonlinear effects and significant sidebands growth was expected in this range of wave steepness.

The general description and graphical representation are presented in Appendix B. Notice that, as discussed in the previous section, Su and Green [8] pointed out that the usual range of wave steepness at sea is $0.12 < \epsilon < 0.20$. So, the range we adopted is larger and the relevance of our analysis for real ocean waves could be argued [35].

The methodology for spectral and wavelet analysis, as well as the wave parameters defined in the temporal analysis, are described in section 3. The initial wave steepness, measured at WP1, is defined as $\epsilon_0 = a_0 k_0$, with a_0 defined in 3.3.1. The frequency of the sidebands will be presented both as ordinary frequency measured in Hz as well as angular frequency $\omega = 2\pi f$ in radians/seconds, which is a scalar measure of rotation rate. Note that the nondimensional frequency referred next,

and used very often in the next sessions and figures, is defined as $\delta\omega/\epsilon\omega_0 = \delta f/\epsilon f_0$

Representative case of sideband growth measurement

The initial wave steepness (calculated at WP1) is $\epsilon_0 = 0.22$, with wave period $T_0 = 0.6\,\mathrm{s}$ and $a_0 \approx 0.021\,\mathrm{m}$. The time series with duration of 100 s is shown in Figure 5.14:

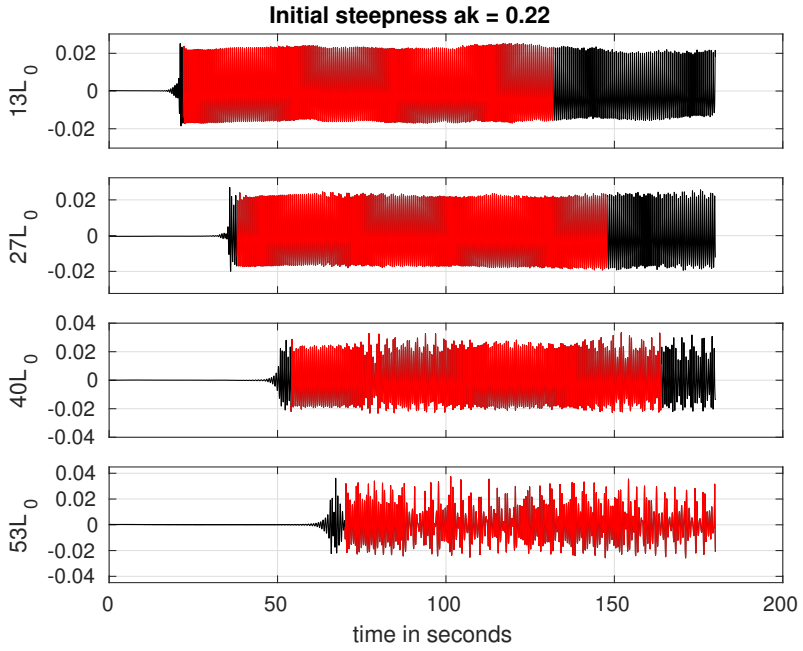

Figure 5.14: Time series of the wave elevation at wave probes: WP1 (13 L_0 from the wavemaker), WP9 (27 L_0 from the wavemaker), WP17 (40L_0 from the wavemaker) and WP25 (53 L_0 from the wavemaker), where L_0 is the wavelength of the carrier wave. Only the red part of the time series was used on the calculations in order to avoid the transients.

From Figure 5.14 it is clear that at the waveprobe 1 at a distance of 13 initial wavelengths (L_0), the time series looks still very regular, with wave amplitude varying from $-0.02m$ at the troughs to $+0.02m$ at the crests. The regular profile remains at $27L_0$, but at $40L_0$ the irregular behavior starts to be very apparent and wave amplitudes reach now values from $A_t \approx -0.02$, where A_t refer to the wave amplitude at the trough, to $Ac \approx 0.04$, almost twice the initial crest amplitude. Finally at $53L_0$ the initially regular wave is now completely irregular and wave groups are more clearly defined showing in the time series plot the Benjamin-Feir instability (which Benjamin referred to as the "wave train breaking up into groups" [36]).

The spectral analysis is performed as described in subsection 5.5.1. In Figure 5.15, we present the evolution of the wave spectrum along the tank. The peak of energy is the spectrum calculated at CS2 (WP18-32) located at about 39 wavelengths of the wavemaker (see Figure 5.14). It can be seen the growth of the sidebands until

the wave reaches CS2. At this location, the frequencies of the carrier wave and sidebands were $f_0 = 1/0.6\,\mathrm{s} = 1.667\,\mathrm{Hz}$, $f_+ = 2.0\,\mathrm{Hz}$ (0.5 s) and $f_- = 1.33\,\mathrm{Hz}$ (0.75 s), respectively. In this case, the condition $2f_0 = f_+ + f_-$ is satisfied, since $2 * 1.667 = 3.334$ and $f_+ + f_- = 2.0 + 1.33 = 3.33$.

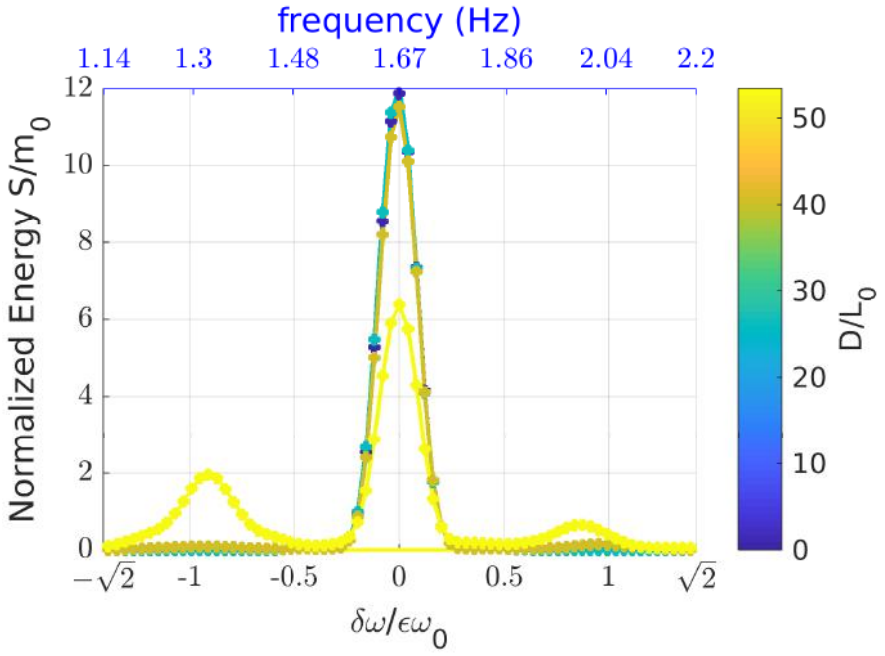

Figure 5.15: Wave spectrum calculated at WP1, WP9, WP17 and WP25 at CS2. Nondimensional frequency $\delta\omega/\epsilon\omega_0$ at the bottom x axis and frequency in Hz at the top.

Considering all the 84 cases and calculating the peak of the sidebands normalized frequencies ($\delta\omega/\epsilon\omega_0$) and comparing with initial wave steepness (Figure 5.17) it is possible to see that the sidebands frequency changes for different wave steepness and there is a clear trend for both low frequency sideband as well as for high frequency, in the range of $0.1 < \epsilon < 0.2$, where $\delta\omega/\epsilon\omega_0$ decreases from $2 > |\delta\omega/\epsilon\omega_0| > 1$, stabilizing in values close to 1 for values of ϵ slightly higher than 0.2. A similar behavior can be seen when comparing sidebands frequencies with distance to wavemaker D/L_0 (Figure 5.18).

Frequencies $\delta\omega/\epsilon\omega_0 \approx 2$ for low values of D/L_0, drop to $\delta\omega/\epsilon\omega_0 \approx 1$ when $D/L_0 \approx 20$, meaning that waves had to propagate at least almost 20 cycles to reach the point of maximum frequency growth since the theory predicts ([21]) the maximum growth of the sidebands occurs for values of the nondimensional frequency $\hat{\delta} \equiv \delta\omega/\epsilon\omega_0$ close to the unit $|\hat{\delta}| \approx 1$.

The normalized energy of the sidebands (S_N = Energy spectrum$/m_0$, where m_0 is the order zero momentum) also grows very rapidly for high values of D/L_0. Figure 5.19 shows the energy of the normalized wave spectrum (S/m_0) at the high

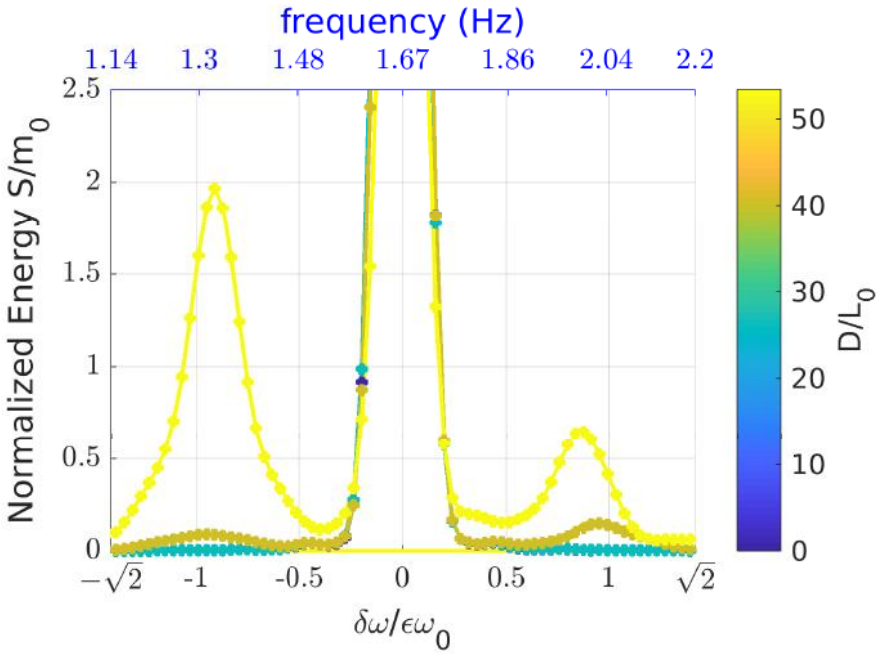

Figure 5.16: Zoom at Figure 5.15 showing the sideband growth.

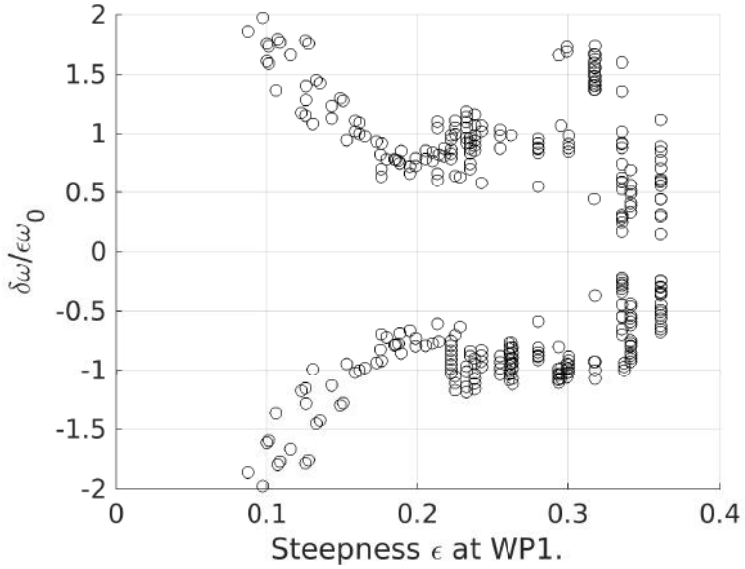

Figure 5.17: Sidebands normalized frequency evolution with initial wave steepness.

frequency sideband (blue circles) and low frequency sideband (red circles).

For more than 20 wave cycles (D/L_0) the low frequency sideband has a much stronger growth than the high frequency one (Figure 5.19). The fact of lower frequency sidebands having higher energy than higher frequency sidebands was also reported by Melville, 1982 ([18]). According to them, the breaking of the higher frequencies components of the spectrum was the main reason the reason for lower

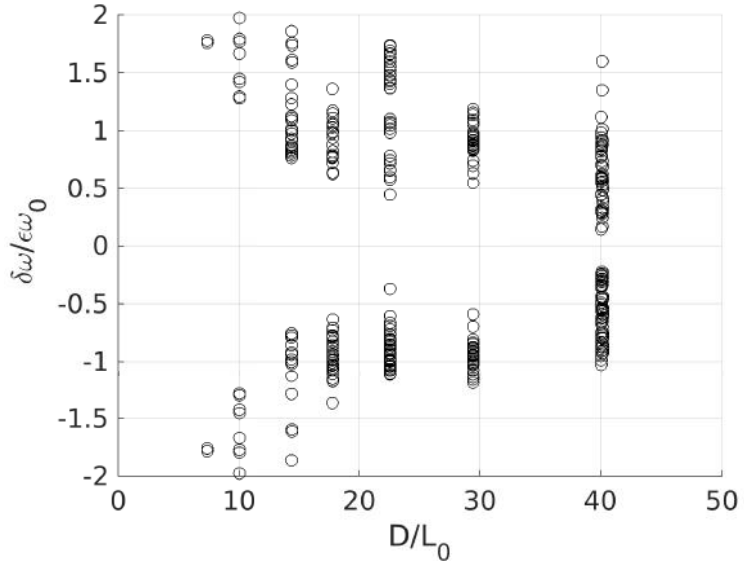

Figure 5.18: Sidebands normalized frequency evolution along the wave tank - D/L_0.

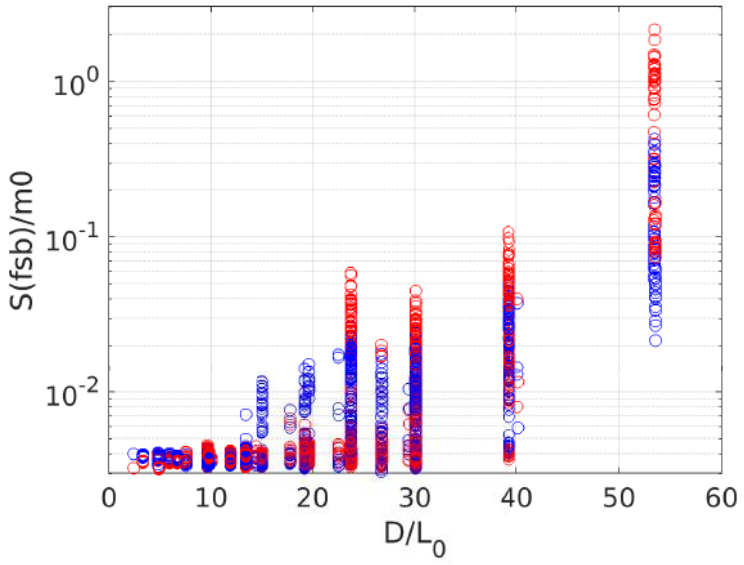

Figure 5.19: Evolution of normalized energy sidebands along the wave tank - D/L_0. Y axis in logarithm scale

energy observed at higher frequencies. It is important to notice that the linear trend on the log scale plot suggest a exponential growth of the sidebands after about 20 wave cycles (D/L_0).

If the energy of the sideband frequency (refereed as fsb) over the frequency of the carrier wave (f_1) is compared with the initial wave steepness, one can see the evolution of the transfer of energy from the main carrier to the sidebands as a function of wave steepness (Figure 5.20).

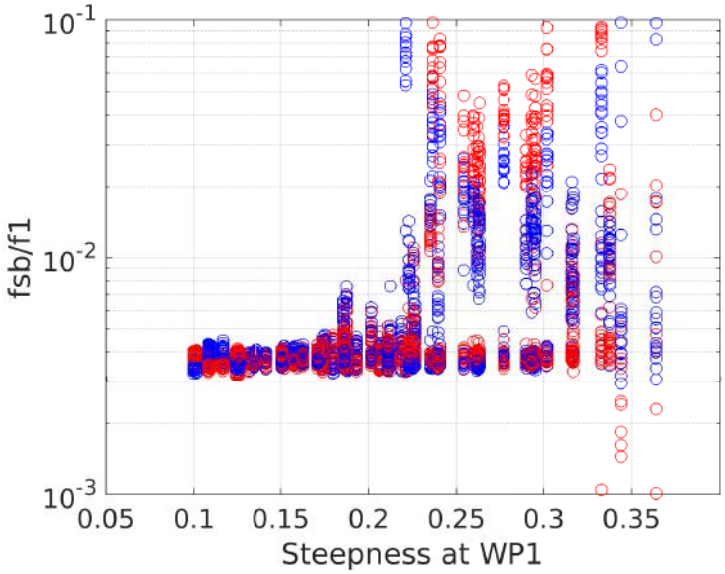

Figure 5.20: Ratio between the energy at sidebands peak frequency and the spectral peak frequency compared to initial wave steepness. Red circles are low frequency sidebands and blue peak of high frequency sidebands.

There were two clear regimes on Figure 5.20: from wave steepness from $\epsilon = 0.05$ to values just above 0.2. This is mostly related to Benjamin-Feir instability modulation and has a linear growth trend of fsb/f_1. For values of wave steepness $\epsilon \approx 0.23$ the first regime is still present but there is a second regime in which the sidebands energy grows much faster up to values of $\epsilon \approx 0.26$ when it starts to decrease. By comparing these results with Figure 5.17, which shows the evolution of the sideband frequencies when varying wave steepness, is possible to see that the higher growth rates are associated with normalized sidebands $|\hat{\delta}| \approx 1$. This fast growth rate is associated with bidimensionality, which seems much more efficient mechanism of energy transfer from the main carrier frequency to the sidebands ([18], [8]).

Proceeding with a spectral analysis of 14 cases with stronger modulation (detailed description on Appendix B) at different spatial locations (wave probes), it was possible to quantify the sideband growth as a function of the initial wave steepness (ϵ_0) and the distance from the wavemaker (Figure 5.21).

As for the representative case described above, on the 14 also shown lower frequency sideband with higher energy $S/m0$ (where S is the spectral energy m^2/Hz and $m0$ is its integral - zero order momentum) than high energy sideband. The explanation for that is also, as described above, being a consequence of higher-frequency sideband breaking and subsequent energy transfer to the lower-frequency sideband.

The dependency of the sidebands' growth on the distance from the wavemaker

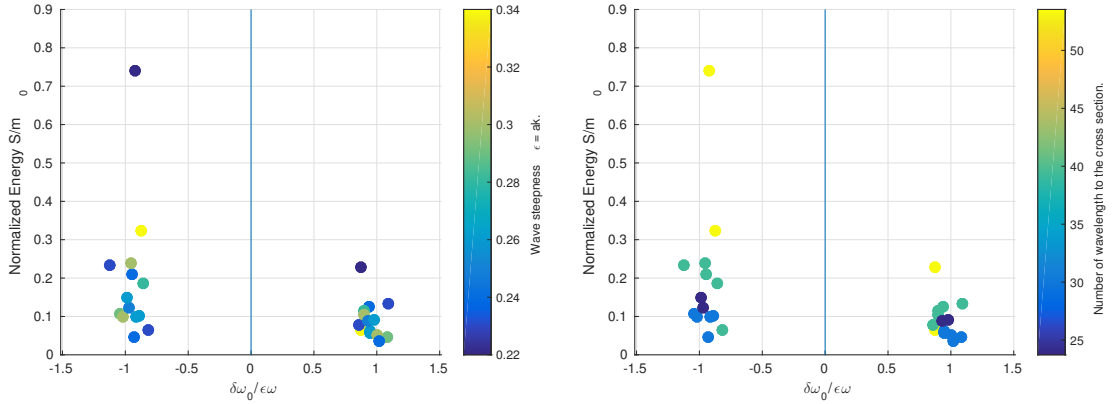

(a) Sideband growth as a function of steepness $\epsilon = ak$ (colorbar).

(b) Sideband growth as a function of number of wavelengths λ to the wavemaker (colorbar)

Figure 5.21: Sideband growth as a function of wave steepness (on the left) and number of wavelengths (on the right)

or on the number of wavelength interactions can be seen in Figure 5.21b. The higher the distance traveled, the higher the nondimensional energy.

When the waves propagate from the wavemaker, the nonlinear interactions between the carrier wave and the sidebands evolve. The highest wave amplitudes are significantly larger when reach CS2 than the ones closer to the wavemaker measured at WP1 (just a few wavelengths after the waves were generated).

In Figure 5.22 we show a measure of lateral modulation along CS2 as a function of the initial wave steepness ϵ_0 at WP1. The higher values of the maximum wave crests (Ac_{max}) relative to the initial wave crest (Ac_0) found in all data sets ($Ac_{max}/Ac_0 = 2$) may be related to expressive sideband growth and high wave steepness. After reaching those maxima, the ratio Ac_{max}/Ac_0 decreased to values close to the initial ones found for low steepness values (see Figure 5.6).

As have been pointed out above, this could be a consequence of wave breaking. In fact, from videos captured simultaneously with the experiments, we obtain concrete evidence of breaking events on these waves.

5.5.2 Bi-dimensional modulational instability

For the scope of the present work, bi-dimensional instability was considered in the following dimensions: 1) the direction of propagation along the wave tank, which is the main direction of propagation of the initial monochromatic waves at the wavemaker (here denoted as the x axis); and 2) the transversal direction of wave propagation, or along the initial monochromatic crests (here denoted as the y axis).

As shown in the previous chapter, the dimensionless parameter $r_\lambda = \lambda_b/L_0$, where λ_b is the lateral wavelength of the modulation and L_0 is the wavelength of

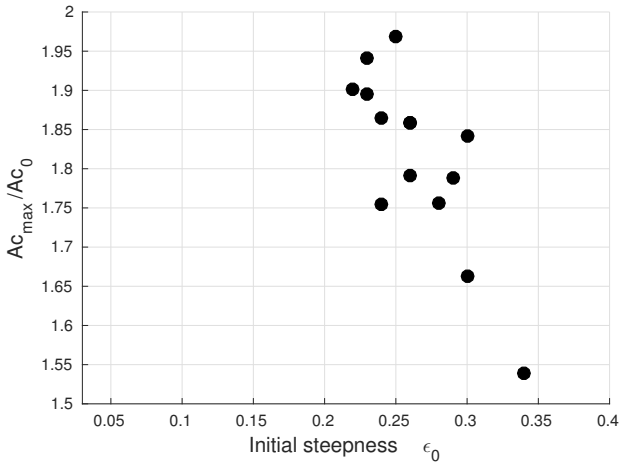

Figure 5.22: Ratio between maximum wave amplitude (Ac_{max}) on WP25 (CS2) and average wave amplitude at WP1 Ac_0 as a function of the initial wave steepness ϵ_0 at WP1. Only the 14 waves presented in Appendix B are shown.

the initial monochromatic wave, measured at the WP1, is the main parameter to measure lateral perturbation in the y direction. Regarding the main direction of wave propagation (x-axis), characteristic parameter is nondimensional frequency $\hat{\delta} \equiv \delta\omega/\epsilon\omega_0$ where $\delta\omega = \omega_{sb} - \omega_0$, ω_{sb} is the frequency of the sideband and ω_0 the frequency of the main carrier.

McLean *et al.* ([13], [15] and [31]) presented theoretical and numerical studies on the 2D instability of finite amplitude waves. They also provided a graphical representation of regions of maximum instabilities for perturbations with wavenumber p and cross-tank wavenumber q. The basic equations followed by them, as many others, for a surface gravity wave on an inviscid, irrotational, incompressible fluid in deep water and in a frame of reference moving with constant speed C (taken as the speed of the unperturbed wave), can be summarized as:

$$\eta = \bar{\eta} = \sum_{n=1}^{\infty} A_n \cos(nx), \tag{5.1}$$

Then they considered the stability of these two-dimensional steady waves to an infinitesimal three-dimensional disturbance, as follows:

$$\eta = \bar{\eta} + \eta', \tag{5.2}$$

assuming $\eta' \ll \bar{\eta}$ and to the first order, they obtained:

$$\eta' = e^{-i\sigma t} e^{i(px+qy)} \sum_{-\infty}^{\infty} a_j e^{ijx}, \tag{5.3}$$

where p and q are arbitrary real numbers and the physical disturbance corresponds to the real part of 5.3. In Chapter 4, the results of the first experiment is compared with McLean *et al.*. In the present section, our attempt is to find a relationship between the parameters r_λ and $\hat{\delta}$.

Figure 5.23 shows the comparison between x component ($\hat{\delta}$) and y component (λ_b/L_0) of instabilities. The sidebands are represented as black circles as low (normalized) frequencies sidebands and blue stars as high frequencies sidebands. Values of λ_b/L_0 becomes high for values of $\hat{\delta} \approx 1$

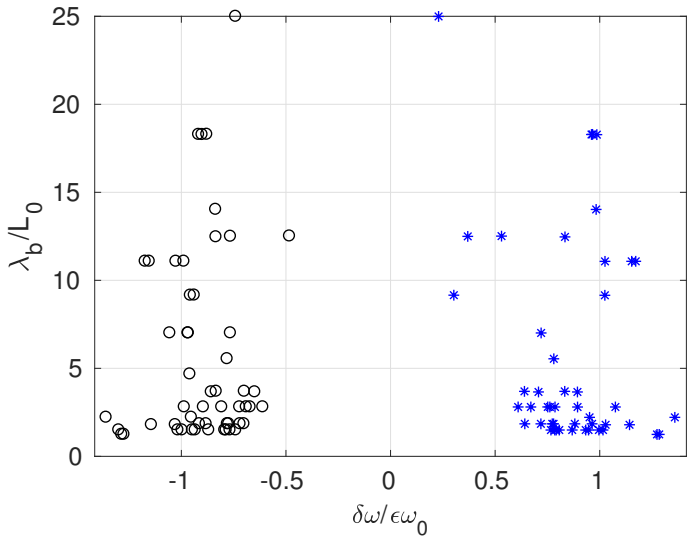

Figure 5.23: Comparison between $\hat{\delta} \equiv \delta\omega/\epsilon\omega_0$ and $r_\lambda = \lambda_b/L_0$. Black circles showing low frequency sidebands and blue star showing high frequency sidebands.

5.6 Summary of the results

The results from the analysis of the data set generated in the second experiment and presented in this chapter can be summarized as follows.

Relationship: R and ϵ_0

In chapter 4 the maximum value for R was about 4, in this new test, measuring the water surface elevation with considerably more wave probes, the resulting maximum values were found to reach very high values $R > 100$. The reason for such high values was the short-crestedness effects at CS2 that, in some cases, at the same phase, at the crest for instance, the minimum crest values could reach very small values, just above zero and the higher crests being of the order of the initial wave crest measured close to the wavemaker (WP1) (see Figure 5.5). The author chose then to consider values of ratio R only lower than 5, since for a small number of individual waves (40

individual waves out of 1260 waves analyzed in this section, or 3% of the total) were so modulated that they become short-crested and the minimum crest was close to zero and the ratio R was higher than 100. It was possible to see that the ratio R remained in the range $1.2 < R < 1.5$ for wave steepness $\epsilon < 0.24$; and for values of steepness higher than that, R grew exponentially up to 4.5. Even for low steepnesses (order of $\epsilon = 0.1$), the waves were also modulated and reached CS1 with values of R around 1.4 and at CS2, values of $R = 1.6$. For high values of initial wave steepness $\epsilon_0 = 0.3$, the values of R still remained the same, i.e., around $R = 1.4$. However, at CS2, for values of wave steepness above 0.24, the values of R become exponentially high.

Relationship: Ac_{max}/Ac_0 and ϵ_0

By comparing the maximum crest amplitude Ac_{max} (at CS1 and CS2) the ratio Ac_{max}/Ac_0 was found to be also close to 1.4 (as it was for R) for steepness values around $\epsilon_0 = 0.18$ and from $0.2 < \epsilon_0 < 0.26$ the value of this ratio had an exponential growth, reaching its maximum value of $Ac_{max}/Ac_0 = 2$. This meant that the maximum crest measured at CS2 can reach 2 times the initial crest at the wavemaker.

Transversal modulation λ_b

The analysis of the transversal modulation was made by normalizing the lateral wavelength of the perturbation, calculated from the spatial wave spectrum at the cross sections CS1 and CS2, by the initial wavelength of the carrier wave measured at the wave probe WP1 (L_0). The ratio λ_b/L_0 was then compared with initial wave steepness ϵ. It was found that at CS1 the energy of the lateral wave spectrum was at least two orders of magnitude smaller than at CS2 and the relationship between λ_b/L_0 and ϵ was not very clear, possibly because the waves propagated for short distances and the effect of nonlinearity had not become significant and the crests were mostly flat. At CS2, however, it was possible to see that for waves with steepness in the range $0.05 < \epsilon_0 < 0.2$, the ratio λ_0/L_0 grow slowly from a range $0.08 < \lambda_b/L_0 \leq 1.5$ (a few waves reaching 2.5) to a range $1.5 < \lambda_b/L_0 < 2$, and above values of $0.2 \leqslant \epsilon_0$ it grew fast to values up to 30. Meaning that strongly-modulated waves might be related to long lateral (crest) wavelength, as compared to the initial wavelength in direction of the wave propagation L_0. Mellville 1982 [18], was able to identify visually the lateral wavelength of the modulation as two times the main carrier with is in agreement which the results found here.

High values of $R = Ac_{max}/Acmin$ were also related to high values of λ_b/L_0 (and also high values of wave steepness ϵ_0), meaning that for λ_b/L_0 large values of the "*lateral amplitude*" of the perturbation are also expected.

As predicted in theory, when the modulation instability was strong enough to manifest the sideband growth in the wave spectrum, either because of strong nonlinear waves or because of traveling a sufficient number of wave cycles to make it strong, the frequencies in all cases analyzed here followed the theoretical condition: $2f_0 = f_+ + f_-$, where the carrier frequency is f_0, the higher frequency of the sideband is f_+ and the lower frequency is f_-.

The dependency of the sidebands' growth on the distance traveled, or on the number of wavelength interactions, can be seen in Figure 5.21b. The farther the distance is traveled, the higher the nondimensional energy (i.e., the number of wavelengths) is.

In many cases, the lower frequency $\hat{\delta}_-$ showed higher nondimensional energy $S/m0$ (where S is the spectral energy m^2/Hz and $m0$ is its integral - zero order momentum). This could be a result of wave breaking at a high frequency and this phenomena could lead to an effective energy transfer at the lower frequency sideband.

Theoretically ([3]), the maximum growth of the sidebands happened for values of the nondimensional frequency $\hat{\delta} \equiv \delta\omega/\epsilon\omega_0$ close to the unity $|\hat{\delta}| \approx 1$. The lower frequency $\hat{\delta}_-$ shown higher nondimensional energy $S/m0$ (where S is the spectral energy m^2/Hz and $m0$ is its integral - zero order momentum). It could be a result of wave breaking at high frequencies and this phenomena could lead to effective energy transfer to the lower frequency sideband.

High values of the maximum wave crests (Ac_{max}), relative to the initial wave crest (Ac_0) found in all data sets ($Ac_{max}/Ac_0 = 2$), were all related to expressive sideband growth and high wave steepness. After reaching this maxima, the ratio Ac_{max}/Ac_0 decreased to values close to the initial ones (see Figure 5.6) relative to low steepness. It could be related to the wave breaking. In fact, videos provide evidence of breaking events on these waves.

Chapter 6

Non-stationarity of nonlinear steep waves - Chaotic behavior

6.1 Introduction

Newton's idea that the motion of a system of particles could be predicted forever into the future by knowing the external forces acting on the system, the particles position, and their velocities, was left behind when scientists recognized that motion of very simple dynamic systems could not be predicted far into the future due to its strong dependencies on initial conditions. It is important, however, to distinguish between random and chaotic motions. The former is related to systems in which either the input forces are unknown or only some statistical measures of its parameters are known. Chaotic motions are those related to deterministic problems for which there are no random or unpredictables inputs or parameters. As quoted by Poincaré [37]:

> It may happen that small differences in initial conditions produce very great ones in the final phenomena. A small error in the former will produce an enormous in the latter. Prediction becomes impossible.

and the current literature assigns the term *chaotic* to the class of motions in deterministic physical and mathematical systems whose time history has a sensitive dependence on initial conditions [38].

In the case of mechanically generated monochromatic water waves in a wave tank, there is no random force being introduced in the system. However, as mentioned before, nonlinear waves are sensible to random perturbations in specific frequencies, or sidebands, where resonance occurs and energy is transfered from the main initial frequency to the sidebands.

6.2 Analysis

In the present research it is shown that weak nonlinear waves can become a chaotic system beyond certain critical initial wave steepness. In order to demonstrate this assertion the following steps were carried out ([38]):

6.2.1 Identification on nonlinear element in the system

Chaotic systems must have nonlinear elements or properties. Finite amplitude Stokes waves are inherently nonlinear and nonlinear effects become stronger as wave steepness $\epsilon = ak$ increases.

6.2.2 Check for sources of random input in the system

There was no source of random input in this system. All the waves were generated as long-crested waves and were allowed to propagate freely along the deep water wave tank, with no external forces acting as wind and currents.

6.2.3 Time history of the measured signal

Often, checking the time series of the wave amplitude provides a good indication of chaos. Here, the time series at different distances from the wavemaker can lead to a substantial change in the system pattern (Figure 6.1).

The water surface elevation time series measured close to the wavemaker (distant $13L_0$ and $27L_0$) are very regular and its periodicity is clear. At $40L_0$ the time series become weakly modulated and the initial regular pattern starts to be disturbed. On the bottom panel of Figure 6.1, however, the time series is very irregular and the periodicity is not clear the length of the wave groups seems to vary and the main wave period is distorted.

A good tool to verify short term variations on the water surface time series is the wavelet. Figure 6.2 shows the time series with 100 seconds of water elevation at the central wave probe of CS2. The carrier frequency is represented by the black line in Figure 6.2 and blue and red line line represents high frequency low frequency sidebands respectively. The modulated nonlinear wave shows a non-stationary behavior and the peak of energy changes every wave cycle. It is not possible to discern the sideband frequencies, but is clear that they are not stationary in time.

By analyzing the wavelet graphic one can observe that the energy looks randomly changing along the time series and the peaks of frequency of the carrier wave and sidebands are not stationary.

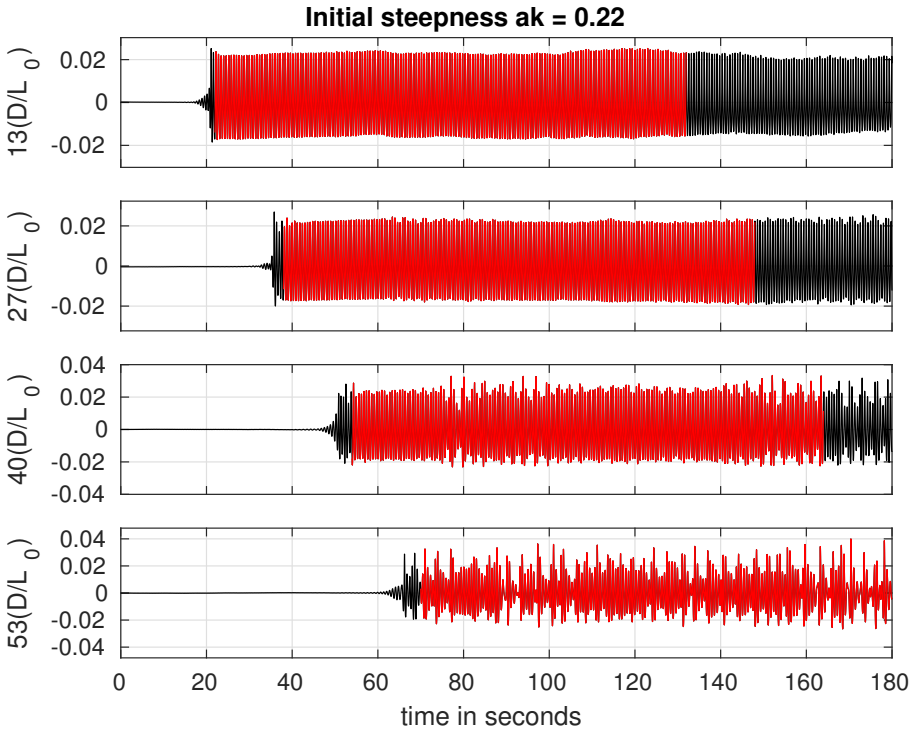

Figure 6.1: Time series of water surface elevation η. Time in seconds in the x axis and water surface elevation in the y axis in meters.

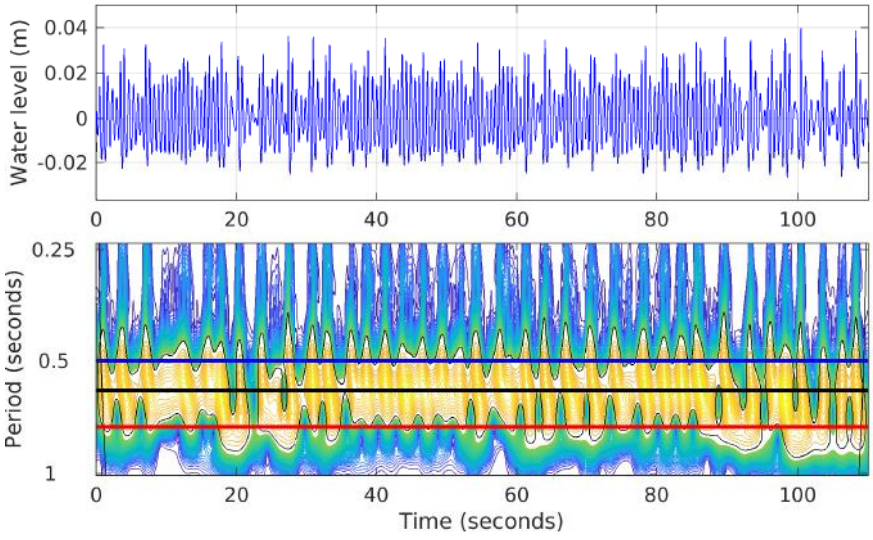

Figure 6.2: Wavelet calculated at the central wave probe at CS2 (WP25) for a time series of 100s. The black line represents the period of the main carrier (peak period on the spectrum), the blue line is the period relative to the higher frequency perturbation ω_- and the red is relative to the lower frequency ω_+.

6.2.4 The phase plan and time-delayed phase plane history

The phase plane is defined as the set of points (x, v) where x is the position of the variable (water surface elevation η in our case) and v its time derivative $d\eta/dt$ or velocity. When the motion is periodic, the phase plane orbit traces out a closed curve. A periodic nonlinear system may show an orbit that crosses itself but is still closed. This could represent a subharmonic oscillation. Chaotic motion, on the other hand, have orbits that never closes or repeat and thus the trajectory of the orbits in the phase plane will tend to fill up a section of the phase space.

Figure 6.3 shows the phase plane relative to the time series shown on Figure 6.1.

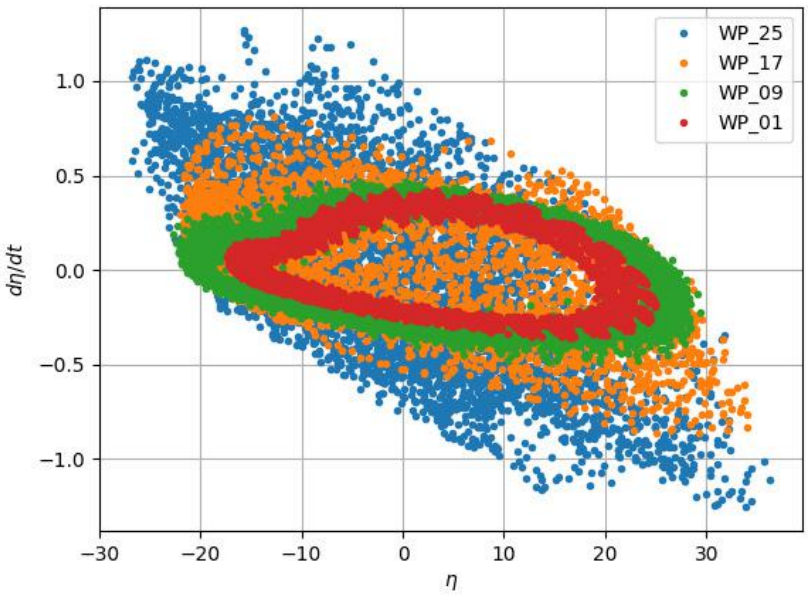

Figure 6.3: Phase plane relative to the time series shown on Figure 6.1 - calculated at WP1, 9, 17 and 25.

Another approach usually applied is to construct the time-delayed phase plane, or pseudo-phase-plane method which, in the case of one degree-of-freedom system with measurements of $\eta(t)$), one plots the signal versus itself, but delayed or advanced by a fixed time constant: $[\eta(t), \eta(t+\tau)]$. The main idea is that the signal $\eta(t+\tau)$ is related to the velocity $d\eta(t)/dt$ and should have properties similar to those in the classic phase plane $[\eta(t), d\eta(t)/dt]$. Figure 6.4 shows the time-delayed phase plane for the waves in 6.1.

In both phase-planes (Figures 6.3 and 6.4), the trajectories of the orbits of the time series measured at WP1 and WP9 are closed and represents the harmonic or periodic motion. However, at WP17 (orange in both figures) the trajectory becomes much more random and crossing itself. At WP25 there is no periodicity at all and

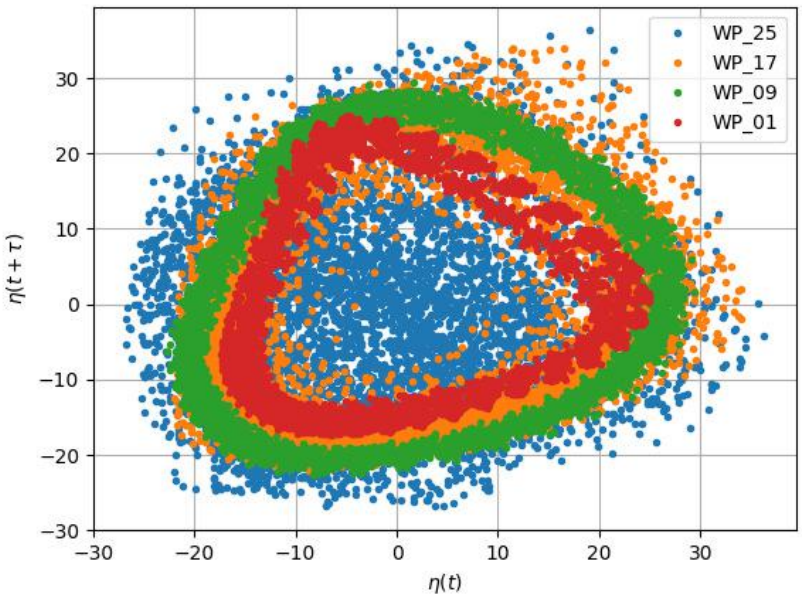

Figure 6.4: Pseudo (or time-delayed) phase plane relative to the time series shown on the Figure 6.1 - calculated at WP1, 9, 17 and 25.

the phase plane shows up as a cloud of dots.

For comparison it was choose a linear small amplitude wave with low wave steepness ($a = 0.05m$, $T = 1.4s$ and $\epsilon = 0.05$. Figure 6.5 shows the time series of this wave measured at WP25 (100s) and its wavelet.

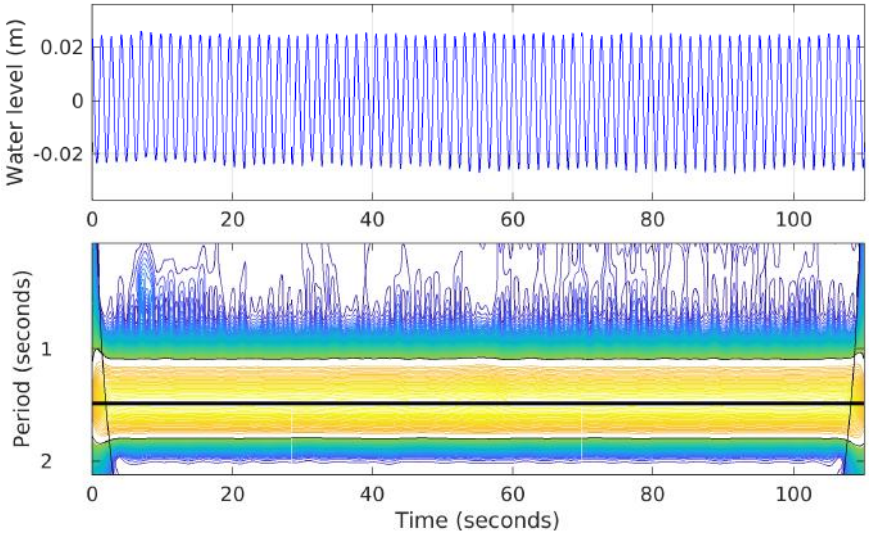

Figure 6.5: Time series and wavelet of a wave with the same amplitude as 6.1, $a = 0.05m$, but with $T = 1.4s$ and $\epsilon = 0.05$

The time series is regular and periodic and waves sinusoids, and wavelet shows clearly the peak period with high frequency (yellow is higher energy, blue is lower) and there is no oscillation of energy among other frequencies. In this case, there is no sideband growth as well.

The phase plane of the linear wave described above is shown on Figure 6.6.

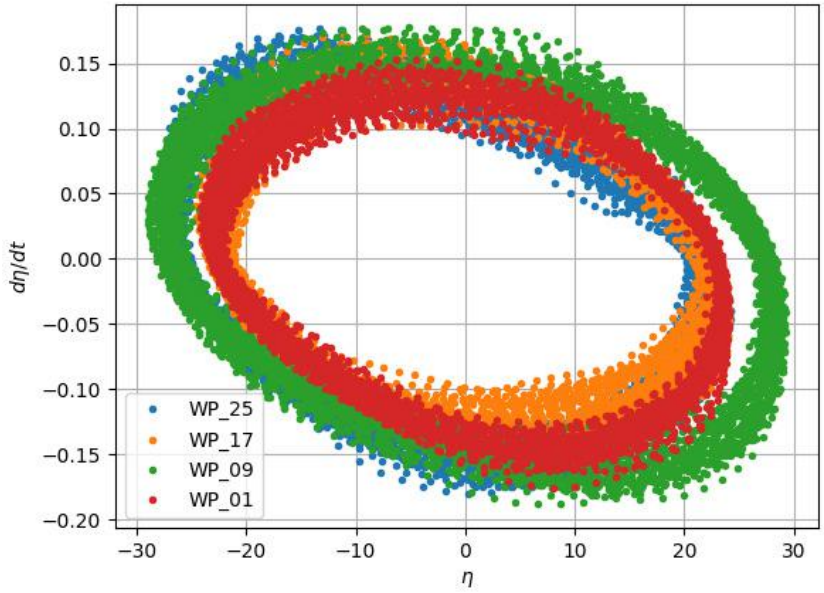

Figure 6.6: Phase plane relative to the time series of a wave with the same amplitude as 6.1, but with T=1.4s and $\epsilon = 0.05$

In all wave probes the phase plane shows closed and regular trajectories as expected for periodic motions in either phase-plane and time-delayed phase plane (Figure 6.6 and 6.7).

6.2.5 Fourier spectrum of the signal

Calculating the Fourier spectrum it is possible to reveal the non-stationary behavior of steep waves. This behavior wasn't expected and wasn't predicted by theory or it is not of knowledge of the author that it was reported previously in the literature despite being observed Fermi-Pasta-Ulam recurrence in such systems ([20]), that could evolve to chaos and, as a Hamiltonian system, is considered as a carrier of chaos ([39]).

The dynamic system was supposed to be stationary, and its spectra should not have evolved or changed when calculated at the same distance D_1/L_0 from the wavemaker. It would be expected for the spectral analysis with different segment sizes of the time series of water surface elevation η (the frequency resolution may change,

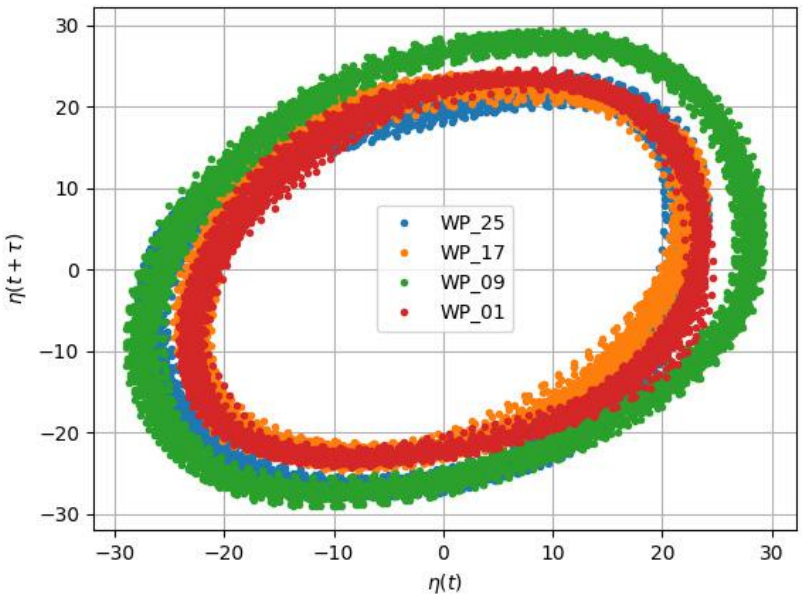

Figure 6.7: Time-delayed phase plane relative to the time series of a wave with the same amplitude as 6.1, but with T=1.4s and $\epsilon = 0.05$

but not the peak frequency), as well as considering the same segments size for spectra calculations in different y coordinates and at the same distance D_1/L_0 from the wavemaker. This characteristic can be detected by taking, for instance, different segments size of the same time series and calculating their spectrum (Fourier transform - fft), or by comparing wave spectrum calculated in different y coordinates (at the same D_1/L_0, at different wave probes at the same cross section, CS1 or CS2).

Figures 6.8 and 6.9 shows the spectrum calculated using different time series segments (red colored), for the same wave at the same wave probe. Both the energy and peak period of the sidebands had changed slightly acoording to the sample size.

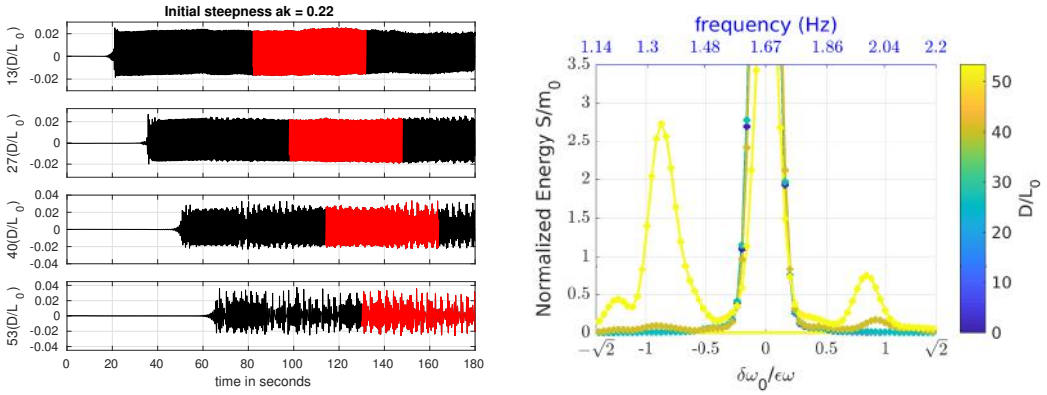

Figure 6.8: Time series of water elevation in meters (y axis) with 100 seconds in red on the left panel; and respective spectrum on the right (WP 26).

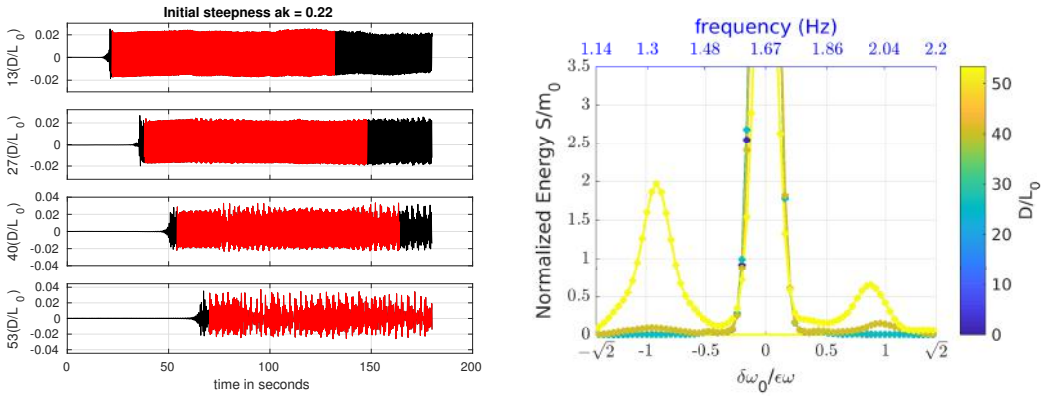

Figure 6.9: Time series of water elevation in meters (y axis) with 50 seconds in red on the left panel; and respective spectrum on the right (WP 26).

Spectral analysis from different wave probes at the same cross section (CS2) lead to very different results (Figure 6.10).

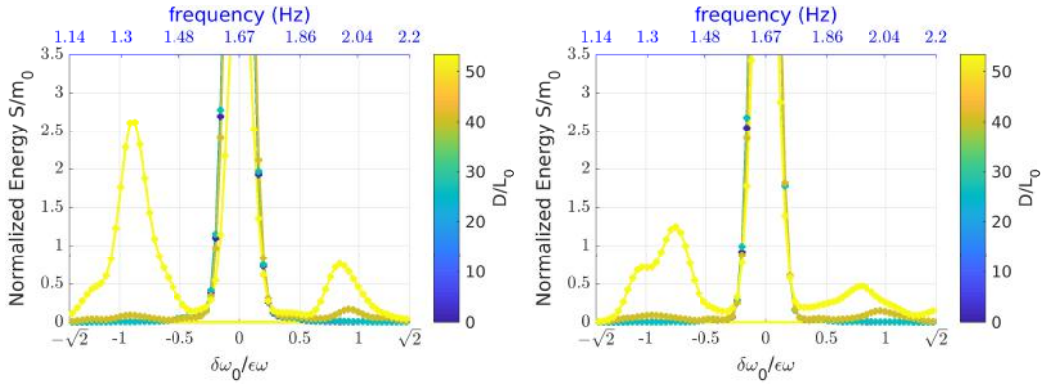

Figure 6.10: Spectrum analysis from WP25 (central) and at extreme left wave probe WP18, both at CS2.

Either energies and peak frequency of the sidebands as well as spectrum profile change substantially just by taking different locations at CS2.

6.3 Summary of the results

In this chapter the chaotic behavior of steep Stokes waves was addressed. Following a simple procedure described in the literature [38] it was possible to identify chaotic regime for steep waves cases of the data set.

The first step was to identify the source of nonlinearity in the system; finite amplitude Stokes waves nonlinear unstable for small amplitude perturbations in specific frequencies/wave-number, waves with steepness $\epsilon > 0.26$ have shown strong modulation and nonlinearity.

The plots of water surface elevation $\eta(t)$ at CS2 was very irregular. The wavelets

also shown random oscillations of the energy peak along the time series. Both results are strong indications of chaotic behavior.

Phase plan and time-delayed phase-plan are usual techniques to identify chaotic motion. Both were calculated and plotted and the expected pattern in chaotic motion was found in both diagrams. A counter example was also shown to illustrate the usual behavior of linear small amplitude waves, and its phase plan showing regular and periodic motion compatible with linear theory.

The Fourier analysis shows that the wave spectrum, calculated at different wave probes at the same distance from the wavemaker (at CS2), are significantly different, while it was expected to be very similar instead. Both energy and sideband frequency changed from wave spectra calculated on different wave probes at WS2. Another important result was differences on wave spectrum when selecting different segments in the same time series. This result shows the non-stationary regime of the motion.

Chapter 7

Wave parameters transformations due to modulation instability

7.1 Wave parameter distributions

Wave parameters as wave crests, wavelength and period change significantly when initially monochromatic nonlinear waves, generated mechanically in a wave tank, propagates away from the generation area. The higher the wave steepness (nonlinearity) and the more cycles the waves travel (shorter wavelengths) the more the waves will change from their initial form. In this chapter we will present an attempt to quantify these changes and to correlate with characteristic wave parameters.

Wave crest and period distributions

As the initial monochromatic steep waves travel enough wave cycles along the wave tank, they can become strongly modulated and, eventually, short-crested despite of its initially long-crested generation. Close to the wavemaker, it is expected that values of individual wave crest and period are mostly clustered close enough to the unidirectional wave parameters programmed to be generated by the mechanical flat plungers (see Chapter 3). When the waves propagate from the wavemaker, they become progressively modulated and their distribution will become more spread. To illustrate, Figure 7.1 shows the distribution of a wave with $\epsilon \approx 0.22$ and period $T_0 = 0.6s$ measured in both CS1 and CS2. The initial wave height was $H_0 = 0.48$, i.e., the crest values plotted as dark blue dots shown in Figure 7.1, are about half of initial wave height ($H = 2a$). The colorbar indicate that these dark blue dots propagated less wavelengths from the wavemaker, therefore, were less subjected to modulational instability.

Figure 7.1 can also be presented by normalized wave parameters. The normalized wave parameters can be obtained by dividing by its mean value and subtracting the

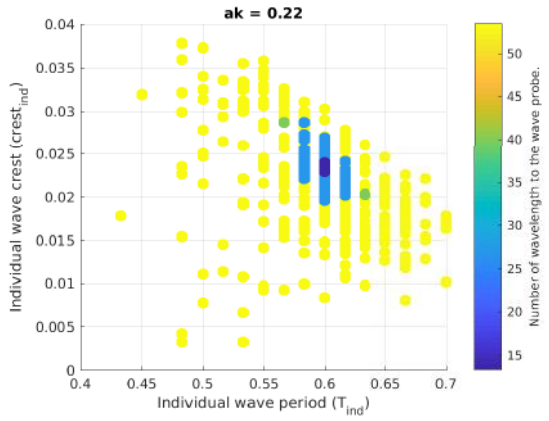

Figure 7.1: Individual wave crest vs. wave period distribution. Colorbar indicates the distance in wavelengths from the wavemaker. Individual wave periods in seconds are shown in the x axis and individual wave crests in meters shown in the y axis.

value 1 to make it be around zero, i.e., normalized wave period $T_{norm} = T_{ind}/T_{mean} - 1$ and normalized wave crest $T_{norm} = Ac_{ind}/Ac_{mean} - 1$. The normalized form is shown in Figure 7.2.

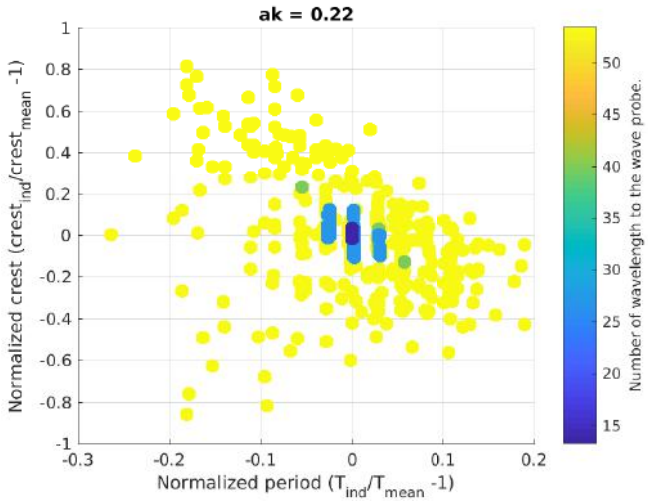

Figure 7.2: Normalized Individual wave crest vs. wave period distribution, special case $\epsilon = 0.22$. Colorbar indicates the distance in wavelengths from the wavemaker.

It is possible to notice that at a short distance from the wavemaker, the values of individual crests and periods are more concentrated around the values relative to the main carrier initially generated. Once the waves travel along the wave tank, they are subjected to transformation in shape and the wave period, and the wave crests are no longer the same as the initial conditions. It is also important to notice that the higher wave crests in the distribution, after being affected by nonlinear effects, have lower periods and they have also higher steepnesses and therefore are more subjected to nonlinear wave interaction and stronger modulation.

The previous Figures were taken from a specific case to illustrate the transformation effects in which the nonlinear waves are subjected. Figure 7.3, on the other hand, includes all 84 cases generated for this test, and for each case, all individual wave parameters are shown in these figures. It was decided, however, to present only the normalized form in order to have all waves in the same graphic limits in the x and y axes.

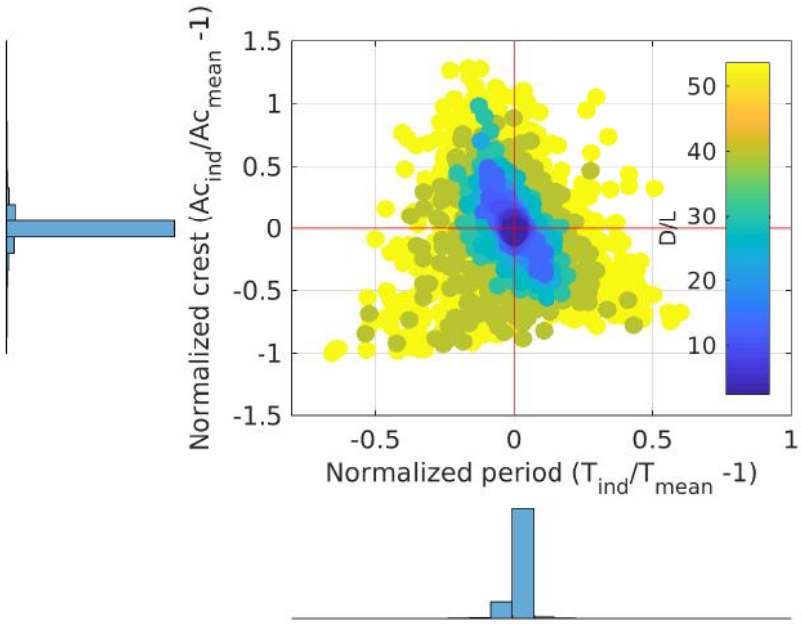

Figure 7.3: Normalized Individual wave crest vs. wave period distribution - **All waves**. Colorbar indicates the distance in wavelengths to the wavemaker.

The higher crests reach now up to twice the mean crests, and the trough limit will be in this case the value 1, since 1 was subtracted from the normalized crest, and the minimum crest height would be close to zero (below zero level,, by definition they would be defined as troughs instead of crests). Wave periods can vary up to 50%, and as seen in the example above (Figure 7.2), there is a trend for higher waves to have shorter periods (wavelengths), and in this way to become more unstable and subject to stronger nonlinear effects.

In order to analyze the wave crest distribution of waves that propagated for longer distances (more cycles), only the waves that propagated 30 cycles or more are shown in the Figure 7.4, as well as the Probability Density Function histogram and the probability distribution in Figure 5.10.

The number of individual waves that traveled for more than 30 wavelengths was 7280. From those, 258 were greater than 1.5 times the mean wave crest; this value represents 3.5% of the waves. The mean value of the normalized wave crests was 0.16 and -0.15 for the wave trough, and the mean of the 5% highest normalized

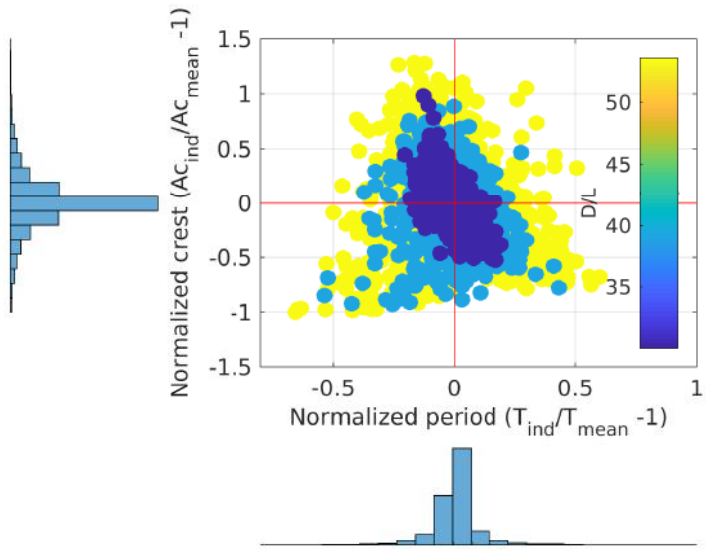

Figure 7.4: Normalized Individual wave crest vs. wave period distribution - **Only the waves propagating no less than 30 cycles/wavelengths**. The colorbar indicates the distance in wavelengths to the wavemaker.

crest was 1.05, i.e., double the mean wave crest. Most of the individual crests had values higher than the mean wave crest (i.e., the normalized wave crest has a value equal to zero). The individual wave periods have also changed considerably after 30 cycles.

By comparing the wave crest vs. the period on the scatter distribution and the initial wave steepnesses ϵ_0 (Figure 7.5), it is possible to see that for small wave steepnesses ($0.05 < \epsilon < 0.1$), the parameters remain almost unchanged (dark blue in the center of the figure). However, for wave steepnesses from about 0.15, the normalized period and crests start to change, and longer normalized period results in smaller crests, while a shorter period results in higher crests. This latest effect makes the waves steeper and nonlinear effects more expected. For waves with a steepness higher than 0.25, however, the distribution starts to be much more scattered, and this dispersion keeps enlarging up to the steepness values of $\epsilon_0 > 0.35$ (yellow dots). The final configuration of the scattering points have three vertices:

- lowest period (length) with half value of the mean period and individual crests as low as the mean water level (zero);
- higher crests with double of the mean wave crests and periods slightly lower than the mean period;
- longer periods with 1.5 times the initial wave period (length) and crests half of the size of the mean wave crests.

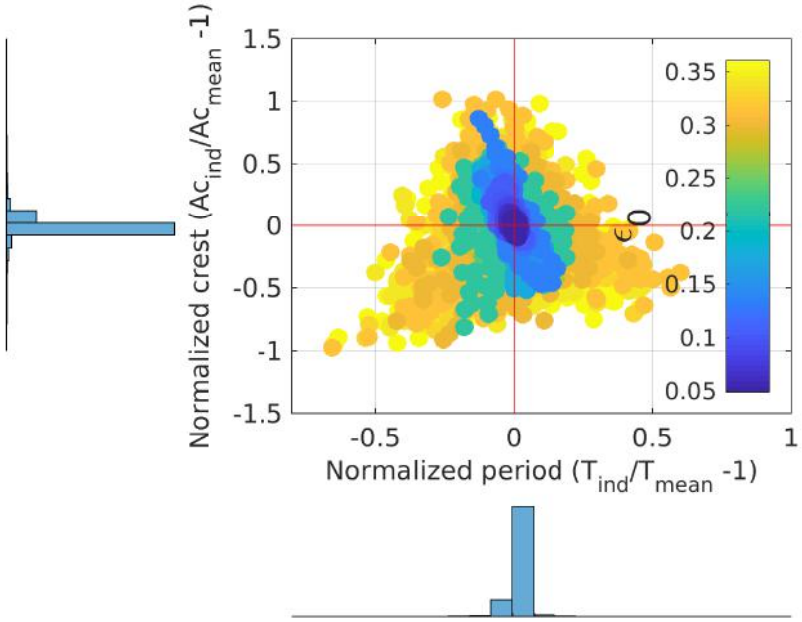

Figure 7.5: Normalized Individual wave crests vs. wave period distribution. The colorbar indicates the initial wave steepness ϵ_0.

7.1.1 Wave height and period distributions and breaking limit

When waves become too steep, breaking events start to take place. In many cases during the experimental tests, it was possible to notice such events, especially when the wavelengths were short, so the waves propagated for many wave cycles before reaching the beach at the end of the tank, and with high initial wave steepness. By observing waves propagating in the laboratory or in the ocean, it is natural to assume that as the wave heights of the individual waves become too large when compared to the wavelength, a natural limit where the shape can no longer be sustained and the waves start to break. The breaking of waves is known as one of the main factors responsible for dissipation of energy in the wave field. During the experiments, where the waves were long-crested monochromatic and deep water steep waves, the wave breaking seems to be also directly responsible for triggering the short cresteness and directionality of the waves, as perceived in the videos taken during the tests.

A theoretical study carried out by Stokes (1847 [1]) predicted that a regular, progressive one-dimensional wave would become unstable and break only if the particle velocity at the crest exceeded the phase velocity. This limit of shape stability of steep waves seems to be reached in deep water when the wave height (H) is about 1.4 times the wavelength of the waves (L), i.e., $H/L = 0.14$, or wave steepness

$\epsilon \approx 0.44$. It happens when the water surface at the crest of the wave reaches an angle of 120°. Toffoli *et al.* [40] presented a statistical analysis of waves, collected from measurements of surface waves in laboratory and open sea, and found a limit for wave breaking at $ak = 0.55$, which was considerably higher than the literature.

The analyses of the present data set were divided in two sets of waves, taking into consideration how the individual waves can be defined, i.e. zero up-crossing (crest first followed by trough) and zero down-crossing (trough first followed by crest). Figure 3.2 shows an schematic of the wave definition where the waves are propagating from right to left. The zero down-crossing and up-crossing wave height (Hd and Hu) are shown in this figure. It is clear that the crest (Ac) is common for both wave definitions, but the period and the wavelengths, therefore the wave steepness, have different values. By plotting these two sets of waves we obtain Figure 7.6 for zero down-crossing and 7.7 for zero up-crossing waves.

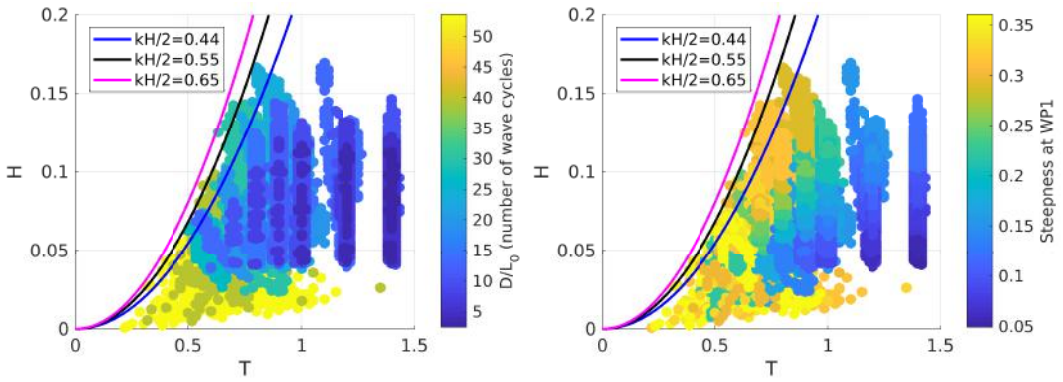

Figure 7.6: Wave height and period distribution for down-crossing waves definition.

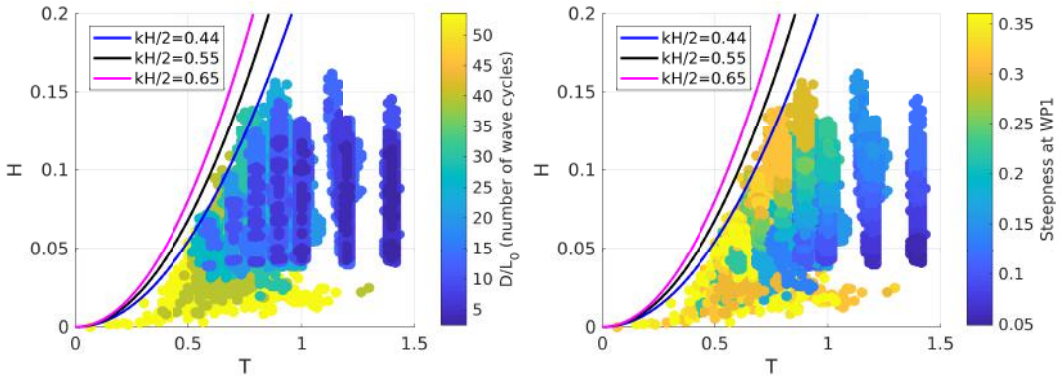

Figure 7.7: Wave height and period distribution for up-crossing waves definition.

The left side sub-figures of 7.6 and 7.7 show in the colorbar the distance D/L_0 (the same as number of wave cycles); on the right side the initial steepness ($\epsilon = ak$) is represented in the colorbar. The first important finding regarding the difference between zero up-crossing (crest-trough) waves to zero down-crossing (trough-crest) is

that down-crossing have a higher limit of steepness. In all four panels the purple line represents the line of steepness $kH/2 = 0.65$ ($\epsilon_0 = kH/2$), and this curve limits for down-crossing waves. On the other hand, up-crossing waves (crest-trough) have its limit bounded by the black curve on the panels, representing the value of steepness $kH/2 = 0.55$, which is the same value found by Toffoli *et al.* [40]. So, the values found here for down-crossing waves are almost 48% higher than the ones based on Stokes (1847) $kH/2 = 0.44$, and about 18% higher than the values by Toffoli *et al.* [40], $kH/2 = 0.55$. In the case of up-crossing waves, the values were in agreement with Toffoli *et al.* [40].

It is also possible to notice, mainly on the right side of all panels, that waves with low steepness or larger periods (wavelengths) that travel for shorter distances to the wave probes, spread less, and are shown as straight vertical lines of blue dots. On the other hand, and shorter waves with high wave steepness spread much more, as can be seen on the right-hand figures, as yellow dots spread on the figures, close to the outer limit of value 0.65.

One of the reasons for finding higher values in these tests than in the literature ([40]) can be explained by the fact that these very steep waves found here are not usually found for deep water water waves in the ocean, which was taken in account in Toffoli *et al.* [40].

7.2 Summary of the results

In this chapter the main wave parameters; namely wave height, crest, period and correspondent wave steepness are quantified and an attempt to correlate them to the emergence of directionality and shortcrestedness in initially long-crested and nonlinear waves is made. The first feature analyzed was the transformation along the wave of initially flat and long crests.

Distribution of normalized crest (Ac) and period (T)

The modifications driven by nonlinear effects along its propagation path in the wave shape (or wave profile) can be quantified by evaluating the changes in the wave period (and wavelength, since the waves are in deep water) and wave crests. The cross distribution of these two parameters can be a good indication, as shown in Figure 7.3. It can be seen that the longer the waves propagate, the more affected by nonlinear effects they become, but it is also expected to be related to the initial wave steepness, since nonlinear effects produce changes in the wave shape that are a direct function of wave steepness, as seen before. So it makes sense to reproduce this graphic of cross distribution, albeit comparing initial wave steepnesses instead

of the number of wave cycles propagated (D/L_0).

By comparing the wave crest vs. period and the initial wave steepness ϵ_0 (Figure 7.5), it is possible to see that for small wave steepnesses ($0.05 < \epsilon < 0.1$), the wave parameters remain almost unchanged. However, for wave steepness from about 0.15, the normalized period and crests start to change, and longer normalized period start to have smaller crests while short period start to have higher crests. This latest effect makes the waves steeper, making more nonlinear effects expected. For waves with steepness higher than 0.25, however, the distribution starts to be much more scattered, and this dispersion keeps enlarging up to the steepness values of $\epsilon_0 > 0.35$ (see the yellow dots). The final configuration of the scattering points have three vertices:

- lowest period (length) with half the value of the mean period, and individual crests, as low as the mean water level (zero);
- higher crests with double the mean wave crests and periods slightly lower than the mean period;
- longer periods with 1.5 times the initial wave period (length), and crests half of the size of the mean wave crests.

Wave height and period distributions and breaking limit

The analyses of the present data set were divided into two sets of waves, taking into consideration the definition of individual waves: zero up-crossing (crest first and trough in the back) and zero down-crossing (trough first and crest in the back). The main conclusion, taken from the analysis of the cross distribution of wave heights and wave period according to the definitions of zero down-crossing and up-crossing waves, was that for zero down-crossing (trough followed by crest), the limit of wave breaking reached values of 0.65, as compared with the traditional 0.44 derived from Stokes theory and recently published in the literature 0.55 ([40]). This value for wave breaking limit was not reported before for either waves found in laboratory or ocean conditions.

Chapter 8

Conclusions

This work is a contribution to the study of nonlinear water waves and the effect of modulational instability caused by infinitesimal perturbations in the media of propagation. An experimental investigation was conducted by generating long-crested waves in deep water in a large wave tank with different wave steepnesses. The first experiment, presented in chapter 4, aims to quantify properties of the lateral wave modulation, to investigate spectral sideband growth and the emergence of directionality on initially long-crested waves. Based on the results of this experiment, it was possible to elaborate a new experiment, which is addressed from chapter 5 onward, allowing to investigate the subject with more detail by proceeding with analysis in the frequency, time and spatial domains.

While it is customary to attribute short-crestedness of waves observed in the ocean to the superposition of long-crested waves coming from different directions, this research argues that the short-crestedness is a natural feature of nonlinear waves. Unlike the well-known McLean instability of two-dimensional wave fields, this research indicates that the initially long crests become modulated even at a relatively low steepness. The strength of this modulation, however, depends on the wave steepness of the carrier waves. This dependence relates both to the mean steepness of the carrier wave train and to an instantaneous steepness of individual waves within wave groups, as the latter is driven by the Benjamin-Feir mechanism in the direction of wave propagation. It should be noted that modulational instability is a possible mechanism responsible for the observed short-crestedness, but is not necessarily the only one.

In order to evaluate and quantify the short-crestedness effects observed in the present experimental study, the ratio between the highest crest observed over the lowest crest at the same wave cycle was calculated. The relationship between $R = Ac_{max}/Ac_{min}$ and ϵ_0 was also examined based on the data set of the second experiment (Chapter 5). While in chapter 4 the minimal ratio of the maxima and minima wave crests across the modulated long wave crests was found to be 1.1 and

the maximum value for R was about 4, by analyzing the data set generated in the second experiment (measuring the water surface elevation with considerably more wave probes) the resulting maximum values reached much higher values ($R > 100$). The reason for such high values was the short crestedness' effects at CS2, making the crest values vary from just above zero at the same wave phase (time) to higher crests of the order of the initial wave crest measured close to the wavemaker (WP1). Analyzing only the cases where R was lower than 5 (only 40 individual waves out of 1260 waves analyzed in this section, or 3% of the total), it was possible to see that the ratio R remained in the range $1.2 < R < 1.5$ for wave steepness $\epsilon < 0.24$; and for values of steepness higher than that, R had grown exponentially up to 4.5. Even for low steepnesses (i.e., order of $\epsilon = 0.1$), waves were also modulated and reached CS1 with values of R around 1.4, and at CS2 values reached of 1.6. It is not of our knowledge previous works on modulational instabilities that have analyzed and quantified the lateral wave deformation by calculating the ratio R. The large dimensions of LabOceano wave tank and the sufficient quantity of wave probes positioned in the transversal sections CS1 and CS2 were of fundamental importance for the calculation of this ratio.

The analysis of the data set collected in the first experiment showed that the length of the lateral modulation ranged from being comparable with the wavelength to four times the wavelength of the carrier wave, depending on the steepness. The results from the second experiment were in agreement with the first test, however, due to many more spatial measurement points (32 wave probes instead of 12 in the first experiment) meaning more spatial resolution, and also due to a much broader range of wave steepness, it was possible to distinguish two main lateral modulation regimes, namely: 1) First regime, as reported in the first experiment, the lateral wavelength of the order of the wavelength of the main carrier up to two times the main carrier wavelength ($\lambda_b/L_0 \approx 1-2$), which was also found by Melville, 1982 ([18]) and also by Brandini 2002 [30], who found in his computational numerical model simulations $\lambda_b/L_0 = 2$ using Higher Order Spectral (HOS) model and a three-dimensional (3D) fully nonlinear Numerical Wave Tank (NWT). This regime is found for values of wave steepness in the range $\epsilon = 0.05 - 0.25$ and the energy of the lateral spectrum is two to three order of magnitude lower than the total energy of the second regime; 2) Second regime; lateral wave length in the range $\lambda_b/L_0 \approx 3-25$, is associated with the emergence of short-crestedness and directionality and values of λ_b/L_0 as high as 20 were not reported in the literature. As mentioned above, the total energy of the lateral spectra is much higher than for the first regime, which can be also indicated for the values of the ratio R, described above. The range of initial wave steepnesses in which the second regime was found was mainly in the range of $\epsilon = 0.25 - 0.4$.

Regarding the comparison from λ_b/L_0 and D/L_0, despite the fact of the values found at CS1 for λ_b/L_0 being of the order of the main carrier to twice its values, the relationship is not very clear at this point of the length of the wave tank, possibly because the waves propagated only for short distance and the effect of nonlinearity did not become significant to see changes with a clear pattern. The lateral modulation is not yet strong for values of R close to 1, and the energy of the lateral spectra is very low, as mentioned. By analyzing the relationship among these two parameters at CS2, however, the regimes cited above are more evident.

The comparison between the maximum crest amplitude Ac_{max} at the cross sections of wave probes with the initial mean wave crest Ac_0 measured at WP1 ($S = Ac_{max}/Ac_0$), it is possible to quantify the growth ratio of the crests along the wave train propagation. Two remarkable regions were found within the range of wave steepnesses in the second experiment, namely:

1. For the range $0.05 \leq \epsilon \leq 0.2$ where it can be noticed the growth of S up to a maximum at $\epsilon \approx 0.14$ and a decrease to values of $\epsilon < 0.2$. This range of wave steepnesses was also studied by Su and Green (1984) [8] and a comparable figure to 5.2 can be seen on their Figure 5 ([8]) where they compare the sideband amplitude a_m with the initial wave crest Ac_0. The parameter S reaches its maximum value, close to 1.4, for steepness values around $\epsilon = 0.13$ while for Su and Green (1984) [8], there was also a maximum value of a_m/Ac_0 at values of $\epsilon_0 = 0.14$. The results, therefore, presented here are in fair agreement with the literature;

2. For $\epsilon > 0.2$: a fast grow of S is found for the range $0.2 < \epsilon < 0.26$, reaching a maximum value at $S = 2$. So, the maximum crest measured at CS2 can reach 2 times the initial crest at the wavemaker because of nonlinear interaction.

The features described above are related to the wave group emergence composed by the carrier wave and the two sidebands. As the nonlinearity becomes strong enough and the sidebands are already well developed, groups of waves can be formed, this wavetrain characteristics was referred by T. Brooke Benjamin as the "wave train breaking up into groups". Because of wave group (or wave packets) generation and short-crestedness, the highest waves observed were over twice the wave height measured in the wave probe closest to the wavemaker, also in accordance with theory [22]. By applying the usual definition for freak waves, it could be thought as a freak wave event generated exclusively by nonlinear effects of modulational instability on initially monochromatic steep waves.

As the long crested nonlinear waves traveled enough wave cycles, it was possible to measure the sideband growth in the wave spectrum. One important result found

was that the frequencies in all cases analyzed here followed the theoretical condition: $2f_0 = f_+ + f_-$, where the carrier frequency is f_0, the higher frequency of the sideband is f_+ and the lower f_-, which is closely related to the fact of theoretically [3], the maximum growth of the sidebands happened for values of the nondimensional frequency $\hat{\delta} \equiv \delta\omega/\epsilon\omega_0$ ($\hat{\delta} \equiv \delta f/\epsilon f_0$) close to the unity $|\hat{\delta}| \approx 1$, where $\delta\omega = \omega_{sb} - \omega_0$, or $\delta f = f_{sb} - f_0$, where f_{sb} is the frequency of the sideband.

It is also expected theoretically an exponential growth of the sidebands when the distance traveled, or number of interactions (cycles), reaches a certain value. The higher the distance traveled, the higher the nondimensional energy, as shown in Figure 5.19. When the number of wave cycles (or D/L_0) reaches values $D/L_0 \approx 20$ the energy of the sidebands grow exponentially.

It was also observed that, in many cases, the sidebands at lower frequency f_- have higher nondimensional energy $S/m0$ (where S is the spectral energy, in m^2/s^2Hz, and $m0$ is its integral - zero order momentum) than the sideband with higher frequency f_+. It could be a result of wave breaking on high frequencies sidebands f_+, and this phenomena could lead to effective energy transfer at the lower frequency sideband and energy dissipation at high frequency sidebands. These two phenomena were also pointed out by Melville, 1982 ([18]).

High values of normalized maximum wave crests (Ac_{max}/Ac_0) were related to a significant sideband growth rate and high wave steepness. After reaching the highest values on the distribution, the ratio Ac_{max}/Ac_0 decreased to values close to the initial ones on its distribution (see Figure 5.6), which were relative to lower steepness. This fact can be related to the wave breaking dissipating energy and making Ac_{max} smaller when reaching breaking limit of wave steepness, and in fact the videos provide concrete evidence of breaking events on these waves.

Another important result is that sidebands growth rates were also function of time series lengths and also of spatially dependent. This means that wave spectra estimated from time series with different lengths are also different, and also spectra calculated in different wave probes located parallel one to the other, at the same distance to the wavemaker (wave probes located at the same cross sections), can show also different growth rates and frequencies. This behavior is related to the chaotic state that the system eventually reaches. By applying usual techniques described in the literature, namely: time series analysis; phase plan and time-delayed phase plane and Fourier analysis, it was possible to qualitatively evaluate the time series of steep nonlinear waves and classify the motion non-stationary and chaotic.

Apparently, if the typical Fourier-based or adaptive methods of directional analysis are applied to the wave data measured in our wave basin, they will all indicate the presence of some directional distribution of wave energy, even though all the waves were initially unidirectional. Thus, an understanding of nonlinear properties

of wave short-crestedness is important both from the point of view of nonlinear dynamics of the ocean waves and for the interpretation of measured data and wave observations.

The modifications in the wave shape (or wave profile) driven by nonlinear effects along propagation direction were quantified by evaluating the changes in the wave period (wavelength) and the wave crests. The cross-distribution of these two parameters can be a good indication of these changes and they are shown in Figure 7.3. In this Figure one can see that the further the waves propagate, the more they are affected by nonlinear effects; but it is also expected to be related to the initial wave steepness, since the nonlinear effects that make the wave shape change are a direct function of wave steepness (as seen in this thesis).

By comparing the wave crest vs. period and the initial wave steepness ϵ_0 on the scatter distribution graphic (Figure 7.5), it is possible to see that for small wave steepness ($0.05 < \epsilon < 0.1$) the wave parameters remain almost unchanged (refer to the dark blue in the center of the Figure); but for wave steepnesses from about 0.15, the normalized period and crests start to change: longer normalized periods have smaller crests and short periods have higher crests. This effect makes the waves steeper, and more nonlinear effects are expected. For waves with steepnesses higher than 0.25, however, the distribution starts to be much more scattered, and this dispersion keeps enlarging up to the steepness values of $\epsilon_0 > 0.35$ (refer to the yellow dots). The final configuration of the scattering points have three vertices:

- lowest period (length) with half the value of the mean period, and individual crest as low as the mean water level (zero);
- higher crests with double the value of the mean wave crests, and periods slightly lower than the mean period;
- longer periods with 1.5 times the initial wave period (length), and crests half of the size of the mean wave crests.

The analyses of the present data set were divided into two sets of waves, taking into consideration the definition of individual waves: zero up-crossing and zero down-crossing. The main conclusion taken from the analysis of the cross distribution of wave heights and wave period accordingly (with the definitions of zero down-crossing and up-crossing waves) was that for zero down-crossing (trough followed by crest) the limit of wave breaking reached values of 0.65, compared with the traditional 0.44 derived from Stokes theory and recently published value of 0.55 [40]. This value for wave breaking limit was not reported before for either waves generated in laboratory or ocean conditions.

Suggestions for future research

Most of experimental studies on modulation instabilities were published from the 1960's to 1980's ([3], [20], [8], [18]) and by the end of 1990's ([29] and [21]) and more recently Hwung et al., 2005 [34] and Pinho and Babanin, 2015 [26]. New technologies and more precise sensors as the ones available at LabOceano and applied here, are essential tools for detailed and accurate studies in such sensible phenomena as modulational instability. The author, thus, encourage new efforts on experimental studies in this field aiming to improve our understanding in such a complex and broad theme.

Bibliography

[1] STOKES, G. "On the theory of oscillatory waves. Appendix B: Considerations relative to the greatest height of oscillatory irrotational waves which can be propagated without change of form." *Transactions of the Cambridge Philosophical Society.*, v. 8, pp. 197–237, 1847.

[2] ZAKHAROV, V. "The instability of waves in nonlinear dispersive media (in Russian)." *Zh. Eksp.Teor. Fiz. Pisma Red.*, v. 51, pp. 1107–1114, 1966.

[3] BENJAMIN, T. B., FEIR, J. F. "The disintegration of wave trains on deep water. Part 1. Theory", *Journal of Fluid Mechanics*, v. 27, pp. 417–430, 1967.

[4] ZAKHAROV, V. "Stability of periodic waves of finite amplitude on the surface of a deep fluid", *J. Appl. Mech. Tech. Phys. USSR*, v. 2, pp. 86–94, 1968.

[5] PHILLIPS, O. *The Dynamics of the Upper Ocean*. Cambridge monographs on mechanics and applied mathematics. Cambridge, UK, Cambridge U.P., 1966.

[6] HASSELMANN, K. "On the non-linear energy transfer in a gravity wave spectrum. Part 1. General theory", *Journal of Fluid Mechanics*, v. 12, pp. 481–500, 1962.

[7] ZAKHAROV, V. E., OSTROVSKY, L. A. "Modulation instability: The beginning", *Physica D: Nonlinear Phenomena*, v. 238(5), pp. 540–548, 2009.

[8] SU, M. Y., GREEN, A. W. "Coupled two and three-dimensional instabilities of surface gravity waves", *Phys. Fluids*, v. 27(11), pp. 2595–2597, 1984.

[9] SEGUR, H., HENDERSON, D., CARTER, J., LI, C., PHEIFF, D., SOCHA, K. "Stabilizing the Benjamin Feir instability", *Journal of Fluid Mechanics*, v. 539, pp. 229–271, 2005.

[10] PHILLIPS, O. "On the dynamics of unsteady gravity waves of finite amplitude. Part 1. The elementary interactions." *Journal of Fluid Mechanics*, v. 9, pp. 193–217, 1960.

[11] WHITMAN, G. "Non-linear dispersion of water waves." *Journal of Fluid Mechanics*, v. 27, pp. 399–412, 1966.

[12] SU, M. "Three-dimensional deep-water waves, Part 1: Experimental measurements of skew and symmetric wave pattern", *Journal of Fluid Mechanics*, v. 124, pp. 73–108, 1982.

[13] MCLEAN, J. W., MA, Y. C., MARTIN, D. U., YUEN, H. C. "Three-Dimensional Instability of Finite-Amplitude Water Waves", *Physical Review Letters*, v. 46, pp. 817–820, 1981.

[14] LONGUET-HIGGINS, M. S. "The instabilities of gravity waves of finite amplitude in deep water. I. Superharmonics", *Proc. Roy. Soc. Lond. Ser. A*, v. 360, pp. 471–488, 1978.

[15] MCLEAN, J. W. "Instabilities of finite-amplitude gravity waves", *Journal of Fluid Mechanics*, v. 114, pp. 315–330, 1982.

[16] YUEN, H. C., LAKE, B. M. "Nonlinear dynamics of deep-water gravity waves", *Advances in Applied Mechanics*, v. 22, pp. 67–229, 1982.

[17] LONGUET-HIGGINS, M. S. "The instabilities of gravity waves of finite amplitude in deep water. II. Subharmonics", *Proc. Roy. Soc. Lond. Ser. A*, v. 360, pp. 489–505, 1978.

[18] MELVILLE, W. K. "The instability and breaking of deep-water waves", *Journal of Fluid Mechanics*, v. 115, pp. 163–185, 1982.

[19] BENJAMIN, T. B. "Instability of periodic wavetrains in nonlinear dispersive systems", *Proc. Roy. Soc. A*, v. 299, pp. 59–75, 1967.

[20] LAKE, B. R., YUEN, H. "A note on some nonlinear water-wave experiments and the comparison of data with theory", *Journal of Fluid Mechanics*, v. 83, pp. 75–81, 1977.

[21] TULIN, M. P., WASEDA, T. "Laboratory observations of wave group evolution, including breaking effects", *Journal of Fluid Mechanics*, v. 378, pp. 197–232, 1999.

[22] OSBORNE, A. R. *Nonlinear ocean Waves and the inverse scattering transform.* 1 ed. London, UK, Academic Press, Elsevier, 2010.

[23] MEI, C. C., STIASSNIE, M., YUE, D. K.-P. *Theory and Applications of Ocean Surface Waves.* 2 ed. Singapore, World Scientific Publishing Co, 2006.

[24] KHARIF, C., PELINOVSKY, E., SLUNYAEV, A. *Rogue Waves in the Ocean*. Advances in Geophysical and Environmental Mechanics and Mathematics. 1 ed. London, UK, Springer-Verlag Berlin Heidelberg, 2009.

[25] YUEN, H. C., LAKE, B. M. "Nonlinear deep water waves: Theory and experiment", *Phys. Fluids*, v. 18, pp. 956–960, 1975.

[26] PINHO, U. F., BABANIN, A. V. "Emergence of short crestedness in originally unidirectional nonlinear waves", *Geophysical Research Letters*, v. 42, pp. 1–6, 2015.

[27] SHEMER, L., KIT, E. "Long-time evolution and regions of existence of parametrically excited nonlinear cross-waves in a tank", *Journal of Fluid Mechanics*, v. 209, pp. 249–263, 1989.

[28] BABANIN, A. V., CHALIKOV, D., YOUNG, I. R. "Numerical and laboratory investigation of breaking of steep two-dimentional waves in deep water", *Journal of Fluid Mechanics*, v. 644, pp. 433–463, 2010.

[29] TRULSEN, K., STANSBERG, C. T., VELARDE, M. G. "Laboratory evidence of three-dimensional frequency downshift of waves in a long tank", *Physics of Fluids*, v. 37, pp. 235–237, 2010.

[30] BRANDINI, C., S., G. "Instability of periodic wavetrains in nonlinear dispersive systems", 2002. Disponível em: <https://personal.egr.uri.edu/grilli/brest.pdf>.

[31] MCLEAN, J. W. "Instabilities of finite-amplitude gravity waves on water of finite depth", *Journal of Fluid Mechanics*, v. 114, pp. 331–341, 1982.

[32] KRASITSKII, V. P. "On reduced equations in the Hamiltonian theory of weakly nonlinear surface waves", *Journal of Fluid Mechanics*, v. 272, pp. 1–20, 1994.

[33] DYSTHE, K., TRULSEN, K. "Note on breather type solutions of the NLS as a model for freakwaves", *Physica Scripta*, v. T82, pp. 48–52, 1999.

[34] HWUNG, H.-H., CHIANG, W.-S. "Measurements of wave modulation and breaking", *Measurement Science and Technology*, v. 16, n. 10, pp. 1921, 2005. Disponível em: <http://stacks.iop.org/0957-0233/16/i=10/a=006>.

[35] FEDELE, F., BRENNAN, J., LEON, S. P., DIAS, F. "Real world ocean rogue waves explained without the modulational instability", *Sci. Rep.*, v. 6, pp. 27715, 2016.

[36] HUNT, J. C. R. "Nonlinear and Wave Theory Contributions of T. Brooke Benjamin (1929–1995)", *Annu. Rev. Fluid Mech.*, v. 38, pp. 1–25, 2006.

[37] POINCARÉ, H. *Science et méthode*. Bibliothèque de philosophie scientifique. Flammarion, 1908.

[38] MOON, F. *Chaotic vibrations: an introduction for applied scientists and engineers*. A Wiley-Interscience publication. Wiley, 1987. ISBN: 9780471856856. Disponível em: <https://books.google.com/books?id=yUbvAAAAMAAJ>.

[39] ZASLAVSKY, G. *The Physics of Chaos in Hamiltonian Systems*. Imperial College Press, 2007. ISBN: 9781860947957.

[40] TOFFOLI, A., BABANIN, A., ONORATO, M. "Maximum steepness of oceanic waves: Field and laboratory experiments", *Geophysical Research Letters*, v. 37, n. 5, pp. n/a–n/a, 2010. ISSN: 1944-8007. doi: 10.1029/2009GL041771. Disponível em: <http://dx.doi.org/10.1029/2009GL041771>.

[41] MACKAY, R. S., SAFFMAN, P. G. "Stability of Water Waves", *Proc. Roy. Soc. Lond. Ser. A*, v. 406, pp. 115–125, 1986.

[42] KREIN, M. G. "Foundations of the theory of λ -zones of stability of a canonical system of linear differential equations with periodic coefficients", *Am. Math. Soc. Trans. Ser. 2*, v. 120, pp. 1–70, 1955.

Appendix A

Note on Benjamin-Feir 1967 and McLean 1982

Notes based on Wilton Arruda's class notes on Nonlinear Waves.

A.1 Perturbation Equations

The equations of free wave motion in a deep ocean are:

$$\nabla^2\phi = 0 \quad , \quad -\infty < z \leq \eta \tag{A.1}$$

$$\nabla\phi \to 0 \quad , \quad z \to -\infty \tag{A.2}$$

$$\eta_t + \eta_x\phi_x + \eta_y\phi_y - \phi_z = 0 \quad , \quad z = \eta \tag{A.3}$$

$$g\eta + \phi_t + \frac{1}{2}\left(\phi_x^2 + \phi_y^2 + \phi_z^2\right) = 0 \quad , \quad z = \eta \tag{A.4}$$

Let' s assume a perturbation of the basic Stokes solution $(\Phi, \overline{\eta})$

$$\phi(x,y,z) = \Phi(x,z) + \epsilon\phi'(x,y,z), \text{ and } \eta(x,y) = \overline{\eta}(x,y) + \epsilon\eta'(x,y). \tag{A.5}$$

If $F(x,y,z)$ is a differentiable function its Taylor series expansion about $z = 0$ for $\epsilon \ll 1$ is

$$F(x,y,\eta) = F(x,y,0) + \epsilon\eta' F_z(x,y,0) + O(\epsilon^2).$$

It follows from A.3 and A.5 that

$$\left(\overline{\eta} + \epsilon\eta'\right)_t + \left(\overline{\eta} + \epsilon\eta'\right)_x \left(\Phi + \epsilon\phi'\right)_x + \left(\overline{\eta} + \epsilon\eta'\right)_y \left(\Phi + \epsilon\phi'\right)_y - \left(\Phi + \epsilon\phi'\right)_z = 0, \ z = \eta.$$

$$[\Phi_\alpha + \epsilon\phi'_\alpha]_{z=\eta} = [\Phi_\alpha + \epsilon\phi'_\alpha]_{z=h} + \epsilon\eta' [\Phi_{\alpha z} + \epsilon\phi'_{\alpha z}]_{z=h} + O(\epsilon^2) = [\Phi_\alpha]_{z=h} + \epsilon [\phi'_\alpha + \eta'\Phi_{\alpha z}]_{z=h} + O(\epsilon^2),$$

where $\alpha = x, y, z$ $O(\epsilon)$, A.3 becomes

$$\eta'_t + \overline{\eta}_x (\phi'_x + \eta'\Phi_{xz}) + \eta'_x \Phi_x + \overline{\eta}_y \left(\phi'_y + \eta'\Phi_{yz}\right) + \eta'_y \Phi_y - (\phi'_z + \eta'\Phi_{zz}) = 0, \ z = \overline{\eta}.$$

Since Φ, h are not functions of y, we have

$$\eta'_t + \overline{\eta}_x \phi'_x + \Phi_x \eta'_x + \eta' (\overline{\eta}_x \Phi_{xz} - \Phi_{zz}) - \phi'_z = 0, \ z = \overline{\eta}.$$

Since

$$[\Phi_\alpha + \epsilon\phi'_\alpha]^2_{z=\eta} = \left[\Phi^2_\alpha + 2\epsilon (\Phi_\alpha \phi'_\alpha + \eta'\Phi_\alpha \Phi_{\alpha z}) + O(\epsilon^2)\right]_{z=h},$$

where $\alpha = x, y, z$, it follows that at $O(\epsilon)$ A.4 becomes

$$\phi'_t + g\eta' + \Phi_x \phi'_x + \Phi_z \phi'_z + \eta' (\Phi_x \Phi_{xz} + \Phi_z \Phi_{zz} + \Phi_{tz}) = 0, \ z = \overline{\eta}.$$

So, the first order perturbations satisfy

$$\nabla^2 \phi' = 0 \quad , \quad -\infty < z \leq \overline{\eta} \tag{A.6}$$

$$\nabla \phi' \to 0 \quad , \quad z \to -\infty \tag{A.7}$$

$$\eta'_t + \overline{\eta}_x \phi'_x + \Phi_x \eta'_x + \eta' (\overline{\eta}_x \Phi_{xz} - \Phi_{zz}) - \phi'_z = 0 \quad , \quad z = \overline{\eta} \tag{A.8}$$

$$\phi'_t + g\eta' + \Phi_x \phi'_x + \Phi_z \phi'_z + \eta' (\Phi_x \Phi_{xz} + \Phi_z \Phi_{zz} + \Phi_{tz}) = 0 \quad , \quad z = \overline{\eta}. \tag{A.9}$$

According to McLean [15], the system A.1 - A.4 can be put in a frame of reference moving with constant speed C (which is the phase speed of the undisturbed solution).

Let (x, y, z) be the moving coordinate system and (X, Y, Z) the fixed coordinate system, so that

$$x = X - Ct, \ y = Y, \ z = Z, \ t = T,$$

and $u = \frac{Dx}{Dt} = \frac{DX}{Dt} - C = U - C$, where u, U are the velocity components at the directions of x, X, respectively.

Let $F(X, Y, Z, T) = f(x, y, z, t)$. So,

$$\frac{\partial f}{\partial x} = \frac{\partial F}{\partial X}\frac{\partial X}{\partial x} = \frac{\partial F}{\partial X},$$

$$\frac{\partial F}{\partial T} = \frac{\partial f}{\partial x}\frac{\partial x}{\partial T} + \frac{\partial f}{\partial t}\frac{\partial t}{\partial T} = \frac{\partial f}{\partial t} - C\frac{\partial f}{\partial x}.$$

In this case, $\eta_T = \eta_t - C\eta_x$, and $\eta = \eta_x$. Also, $\phi_X = U = \phi_x + C = (\phi + Cx)_x$, and consequently $\phi(X, Z, T) = \phi(x, z, t) + Cx$, and

$$\phi_T = (\phi + Cx)_T = \phi_t - C\phi_x + C\frac{\partial x}{\partial T} = \phi_t - C\phi_x - C^2$$

So, from A.3

$$\begin{aligned} \eta_T + \eta_X\phi_X + \eta_Y\phi_Y - \phi_Z &= (\eta_t - C\eta_x) + \eta_x(\phi_x + C) + \eta_y\phi_y - \phi_z \\ &= \eta_t + \eta_x\phi_x + \eta_y\phi_y - \phi_z = 0,\ z = \eta. \end{aligned}$$

Also, from A.4

$$\begin{aligned} g\eta + \phi_T + \frac{1}{2}\left(\phi_X^2 + \phi_Y^2 + \phi_Z^2\right) &= g\eta + (\phi_t - C\phi_x) + \frac{1}{2}\left(\left(\phi_x^2 + 2C\phi_x + C^2\right) + \phi_y^2 + \phi_z^2\right) \\ &= g\eta + \phi_t + \frac{1}{2}\left(\phi_x^2 + \phi_y^2 + \phi_z^2\right) - \frac{C^2}{2} = 0,\ z = \eta, \end{aligned}$$

so that

$$g\eta + \phi_t + \frac{1}{2}\left(\phi_x^2 + \phi_y^2 + \phi_z^2\right) = \frac{C^2}{2},\ z = \eta.$$

Finally, in a frame of reference moving with constant speed C, the system A.1 - A.4 takes the form (McLean [15]):

$$\nabla^2\phi = 0 \quad , \quad -\infty < z \leq \eta \tag{A.10}$$

$$\nabla\phi \to 0 \quad , \quad z \to -\infty \tag{A.11}$$

$$\eta_t + \eta_x\phi_x + \eta_y\phi_y - \phi_z = 0 \quad , \quad z = \eta \tag{A.12}$$

$$g\eta + \phi_t + \frac{1}{2}\left(\phi_x^2 + \phi_y^2 + \phi_z^2\right) = \frac{C^2}{2} \quad , \quad z = \eta. \tag{A.13}$$

Now, let's split the variables η and ϕ as the sum of the Stokes solutions $\overline{\eta}$ and Φ and perturbations η' and ϕ', that is

$$\eta = \overline{\eta} + \eta',\ \text{and}\ \phi = \Phi + \phi'.$$

In the moving reference frame $\Phi_t = 0$, so the perturbations satisfy (assuming $g = 1$):

$$\nabla^2 \phi' = 0 \quad , \quad -\infty < z \leq \overline{\eta} \tag{A.14}$$

$$\nabla \phi' \to 0 \quad , \quad z \to -\infty \tag{A.15}$$

$$\eta'_t + \overline{\eta}_x \phi'_x + \Phi_x \eta'_x + \eta' \left(\overline{\eta}_x \Phi_{xz} - \Phi_{zz} \right) - \phi'_z = 0 \quad , \quad z = \overline{\eta} \tag{A.16}$$

$$\phi'_t + \eta' + \Phi_x \phi'_x + \Phi_z \phi'_z + \eta' \left(\Phi_x \Phi_{xz} + \Phi_z \Phi_{zz} \right) = 0 \quad , \quad z = \overline{\eta}, \tag{A.17}$$

where (taking $\lambda = 2\pi$, we have $k = 1$, and $\omega = \sqrt{gk} = 1$)

$$\overline{\eta}(x) = \sum_{n=1}^{\infty} A_n \cos(nx), \tag{A.18}$$

$$\Phi(x, z) = -Cx + \sum_{n=1}^{\infty} B_n \sin(nx)\, e^{nz}, \tag{A.19}$$

where A_n, B_n, and C are functions of ka. McLean (1982) [15] looks for solutions of the form

$$\eta'(x, t) = e^{i(px - qy - \sigma t)} \sum_{j=-\infty}^{\infty} a_j\, e^{ijx}, \tag{A.20}$$

$$\phi'(x, y, z, t) \quad = \quad e^{i(px - qy - \sigma t)} \sum_{j=-\infty}^{\infty} b_j\, e^{ijx} \exp\left\{ \left[(p + j)^2 + q^2 \right]^{\frac{1}{2}} z \right\}, \tag{A.21}$$

where p and q are arbitrary real numbers. Note that the perturbations A.20 and A.21 are periodic in the y direction with period $2\pi/q$, but they are periodic on the x direction only if p is rational. The expression of ϕ' in A.21 is taken so that it satisfies A.14 and A.15. If we do not assume $\lambda = 2\pi$

$$\eta'(x, t) = e^{i(pk_0 x - qk_0 y - \sigma t)} \sum_{j=-\infty}^{\infty} a_j\, e^{ijk_0 x},$$

$$\phi'(x, y, z, t) = e^{i(pk_0 x - qk_0 y - \sigma t)} \sum_{j=-\infty}^{\infty} b_j\, e^{ijk_0 x} \exp\left\{ \left[(p + j)^2 + q^2 \right]^{\frac{1}{2}} k_0 z \right\},$$

where k_0 is the wavenumber of the basic Stokes wave.

Note that the physical disturbance is the real part of the above expressions and pk_0 and qk_0 are the longitudinal and transverse wavenumbers of the perturbation

(with respective periods $2\pi/pk_0$ and $2\pi/qk_0$).

The terms in the sums have the spacial periodicity of the basic Stokes wave. So, the perturbations A.20 and A.21 feel the presence of the basic Stokes wave. Instability corresponds to $\Im(\sigma) \neq 0$ (the imaginary part of σ is nonzero).

Substituting A.20 and A.21 into A.16-A.17, we get

$$\begin{aligned}(1+\Phi_x\Phi_{xz}+\Phi_z\Phi_{zz})\sum_{-\infty}^{\infty} a_j\, e^{ijx} + \sum_{-\infty}^{\infty}\left(i(p+j)\Phi_x + [(p+j)^2+q^2]^{\frac{1}{2}}\,\Phi_z\right) b_j\, e^{ijx}e^{\alpha_j\overline{\eta}} \\ = i\sigma\sum_{j=-\infty}^{\infty} b_j\, e^{ijx}e^{\alpha_j\overline{\eta}} \\ \sum_{-\infty}^{\infty}\left[\Phi_{xz}\overline{\eta}_x - \Phi_{zz} + i\,(p+j)\,\Phi_x\right] a_j\, e^{ijx} + \sum_{-\infty}^{\infty}\left(i(p+j)\overline{\eta}_x - [(p+j)^2+q^2]^{\frac{1}{2}}\right) b_j\, e^{ijx}e^{\alpha_j\overline{\eta}} \\ = i\sigma\sum_{j=-\infty}^{\infty} a_j\, e^{ijx},\end{aligned} \tag{A.22}$$

for $0 \leq x \leq 2\pi$, where $\alpha_j = [(p+j)^2+q^2]^{\frac{1}{2}}$.

This is a system where σ is the eigenvalue and $\mathbf{u} = [a_j, b_j]^T$, $-\infty < j < \infty$ is the eigenvector. In matrix form we have a system $(\mathbf{A} - \sigma\mathbf{B})\mathbf{u} = 0$, where $\mathbf{A}$ and $\mathbf{B}$ are complex matrices depending on the steepness of the basic wave, p, and q.

If σ is an eigenvalue, σ^* is an eigenvalue

In fact, since $\Phi(-x,y,z) = -\Phi(x,y,z)$ and $\overline{\eta}(-x,y,z) = \overline{\eta}(x,y,z)$, we have $\Phi_x(-x,y,z) = \Phi_x(x,y,z)$ and $\overline{\eta}_x(-x,y,z) = -\overline{\eta}(x,y,z)$.

Calculating A.22 at $-x$, we have

$$\begin{aligned}(1+\Phi_x\Phi_{xz}+\Phi_z\Phi_{zz})\sum_{-\infty}^{\infty} a_j\, e^{-ijx} + \sum_{-\infty}^{\infty}\left(i(p+j)\Phi_x - [(p+j)^2+q^2]^{\frac{1}{2}}\,\Phi_z\right) b_j\, e^{-ijx}e^{\alpha_j\overline{\eta}} \\ = i\sigma\sum_{j=-\infty}^{\infty} b_j\, e^{-ijx}e^{\alpha_j\overline{\eta}} \\ \sum_{-\infty}^{\infty}\left[-\Phi_{xz}\overline{\eta}_x + \Phi_{zz} + i\,(p+j)\,\Phi_x\right] a_j\, e^{-ijx} + \sum_{-\infty}^{\infty}\left(-i(p+j)\overline{\eta}_x - [(p+j)^2+q^2]^{\frac{1}{2}}\right) b_j\, e^{-ijx}e^{\alpha_j\overline{\eta}} \\ = i\sigma\sum_{j=-\infty}^{\infty} a_j\, e^{-ijx},\end{aligned}$$

Taking the conjugate of both equations, we have

$$\begin{aligned}(1+\Phi_x\Phi_{xz}+\Phi_z\Phi_{zz})\sum_{-\infty}^{\infty} a_j^*\, e^{ijx} - \sum_{-\infty}^{\infty}\left(i(p+j)\Phi_x + [(p+j)^2+q^2]^{\frac{1}{2}}\,\Phi_z\right) b_j^*\, e^{ijx}e^{\alpha_j\overline{\eta}} \\ = -i\sigma^*\sum_{j=-\infty}^{\infty} b_j^*\, e^{ijx}e^{\alpha_j\overline{\eta}} \\ -\sum_{-\infty}^{\infty}\left[\Phi_{xz}\overline{\eta}_x - \Phi_{zz} + i\,(p+j)\,\Phi_x\right] a_j^*\, e^{ijx} + \sum_{-\infty}^{\infty}\left(i(p+j)\overline{\eta}_x - [(p+j)^2+q^2]^{\frac{1}{2}}\right) b_j^*\, e^{ijx}e^{\alpha_j\overline{\eta}} \\ = -i\sigma^*\sum a_j^*\, e^{ijx},\end{aligned}$$

Taking $\widetilde{a}_j = -a_j^*$ and $\widetilde{b}_j = b_j^*$ (or vice versa), it follows that A.20 and A.21 with $\widetilde{a}_j$, $\widetilde{b}_j$ in the place of a_j, b_j are eigenfunctions associated with the eigenvalue σ^*. So, the condition for instability is $\Im(\sigma) \neq 0$.

Symmetry of the eigenfunctions

Let us denote $\eta_n'[p,q]$, $\Phi_n[p,q]$ the perturbation solutions associated with n^{th}

eigenvector $\{a_j^{p,q}, b_j^{p,q}\}$, $-\infty < j < \infty$, and $\sigma_n[p,q]$ the n^{th} eigenvalue at the perturbation wave vector (p,q).

$\eta'_n[p,q] = \eta'_n[p+m,q](x,t)$, $\Phi_n[p,q] = \Phi_n[p+m,q](x,t)$,

and in fact,

$$\eta'_n[p,q](x,t) = \sum_{j=-\infty}^{\infty} a_j^{p,q}\, e^{i((p+j)x+qy-\sigma_n t)} = \sum_{j=-\infty}^{\infty} a_{j+m}^{p,q}\, e^{i((p+m+j)x+qy-\sigma_n t)} = \eta'_n[p+m,q](x,t),$$

where the last identity is true since the coefficients $a_{j+m}^{p,q} = a_j^{p+m,q}$ and $b_{j+m}^{p,q} = b_j^{p+m,q}$ satisfy A.22 for $p+m$ in place of p.

$\eta'_n[p,q] = \eta'_n[p,-q]$.

In fact, change y by $-y$ in (20), (21), and (22).

Taking the conjugate of η'_n

$$(\eta'_n)^* = \sum_{j=-\infty}^{\infty} a_j^*\, e^{-i((p+j)x+qy-\sigma_n^*)} =$$

A.1.1 Solution for the undisturbed basic state

For $ak = 0$ (a is the wave amplitude and $k = 2\pi/\lambda = 1$, since McLean assumed $\lambda = 2\pi$) the unperturbed solution is

$$\overline{\eta} = 0,\ \Phi = -x,\ C = 1. \tag{A.23}$$

Note. In fact $C = \left[\frac{g}{k}(1+k^2a^2)\right]^{1/2} = 1$ for $ak = 0$, and $g = 1$.

In this case the system A.22 takes the form

$$\begin{array}{r} \sum_{-\infty}^{\infty} (a_j\, e^{ijx} - i(p+j)b_j)\, e^{ijx} = i\sigma \sum_{j=-\infty}^{\infty} b_j\, e^{ijx} \\ \sum_{-\infty}^{\infty} \left(-i\,(p+j)\,a_j\, e^{ijx} - [(p+j)^2+q^2]^{\frac{1}{2}}\, b_j\right) e^{ijx} = i\sigma \sum_{j=-\infty}^{\infty} a_j\, e^{ijx} \end{array} \tag{A.24}$$

Note that

$$\int_0^{2\pi} e^{ijx} dx = \begin{cases} 0 & ,\ j \in \mathbb{Z} \\ 2\pi & ,\ j = 0 \end{cases}$$

Multiplying (24) by e^{-inx} and integrating from 0 to 2π, we have

$$\begin{array}{r} a_n - i(p+n)b_j = i\sigma_n b_n \\ -i\,(p+j)\,a_n - [(p+n)+q^2]^{\frac{1}{2}}\, b_n = i\sigma_n a_n \end{array} \tag{A.25}$$

From the first equation of (25) $b_n = -ia_n/\left[\sigma_n + (p+n)\right]$ and plugging into the second equation, we get

$$ia_n \left\{ \left[\sigma_n + (p+n)\right]^2 - \left[(p+n)^2 + q^2\right]^{\frac{1}{2}} \right\} = 0.$$

In this case,

$$\sigma_n^{\pm}(p,q) = -(p+n) \pm \left[(p+n)^2 + q^2\right]^{\frac{1}{4}}. \tag{A.26}$$

We can take the eigenvector such that $a_n = 1$, $b_n = -i/\left[\sigma_n + (p+n)\right]$, and $a_j = b_j = 0$ for $j \neq n$.

According to Karif book [24]: "The eigenvalues are real, hence the state corresponding to A.23 is spectrally stable. As the wave steepness of the Stokes wave increases, the eigenvalues move. MacKay and Saffman [41] derived a necessary condition for a Stokes wave to lose spectral stability corresponding to the collision of eigenvalues of opposite Krein signature (Krein 1955 [42]), or a collision of eigenvalues at zero (MacKay and Saffman [41])"

$$\sigma_{n_1}^{\pm} = \sigma_{n_2}^{\pm} \tag{A.27}$$

Note that the choice of signs in A.26 determines the since of the wave propagation.

The dominant wavenumbers associated to the eigenvalues in A.27 are $\mathbf{k}_1 = (p + n_1, q)$ and $\mathbf{k}_2 = (p + n_2, q)$.

According to McLean [15] the solutions of A.27 can be divided in two classes ($m \geq 1$).

Class I:

$$\sigma_m^+ = \sigma_{-m}^-\,,\ \mathbf{k}_1 = (p+m, q)\,,\ \mathbf{k}_2 = (p-m, q),$$

$$\left[(p+m)^2 + q^2\right]^{\frac{1}{4}} + \left[(p-m)^2 + q^2\right]^{\frac{1}{4}} = 2m = N.$$

Class II:

$$\sigma_m^+ = \sigma_{-m-1}^-\,,\ \mathbf{k}_1 = (p+m, q)\,,\ \mathbf{k}_2 = (p-m-1, q),$$

$$\left[(p+m)^2 + q^2\right]^{\frac{1}{4}} + \left[(p-m-1)^2 + q^2\right]^{\frac{1}{4}} = 2m+1 = N.$$

The Class I curves are symmetric about the origin (if we change p by $-p$ and q by $-q$ in equation).

The Class II curves can be rewritten as

$$\left[\left(p-\frac{1}{2}+m+\frac{1}{2}\right)^2+q^2\right]^{\frac{1}{4}}+\left[\left(-p+\frac{1}{2}+m+\frac{1}{2}\right)^2+q^2\right]^{\frac{1}{4}}=2m+1=N,$$

so the curve is symmetric about $p=\frac{1}{2}$, $q=0$ (if we change $p-\frac{1}{2}$ by $-p+\frac{1}{2}$ and q

Appendix B

Sidebands Growth

B.1 Wave 5

The initial wave steepness (calculated on the wave probe 1) $ak = 0.23$, where the wave period $T_0 = 0.7s$, and $a_0 \approx 0.03m$. The time series for the analysis with 100 seconds (from the total of 180s) and is shown in red on the figure B.1:

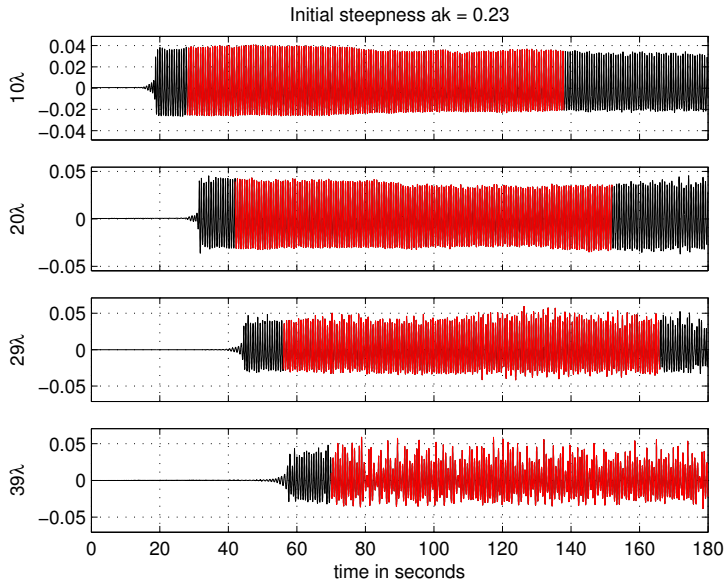

Figure B.1: Time series of the wave elevation at wave probes: 1, 9, 17 and 25. Red segment was used on the calculations.

The spectral analysis was made as described on the subsection 5.5.1. The figure color bar represents the distance from the wavemaker to the wave probe. The red spectra on the figure is relative to the cross section 2 (WP18-32), in this case at about 30 wavelengths of distance to the wavemaker (see figure B.1). The red spectrum shown in the figure is the average spectrum of the 15 spectrum at the cross section (WP18-32).

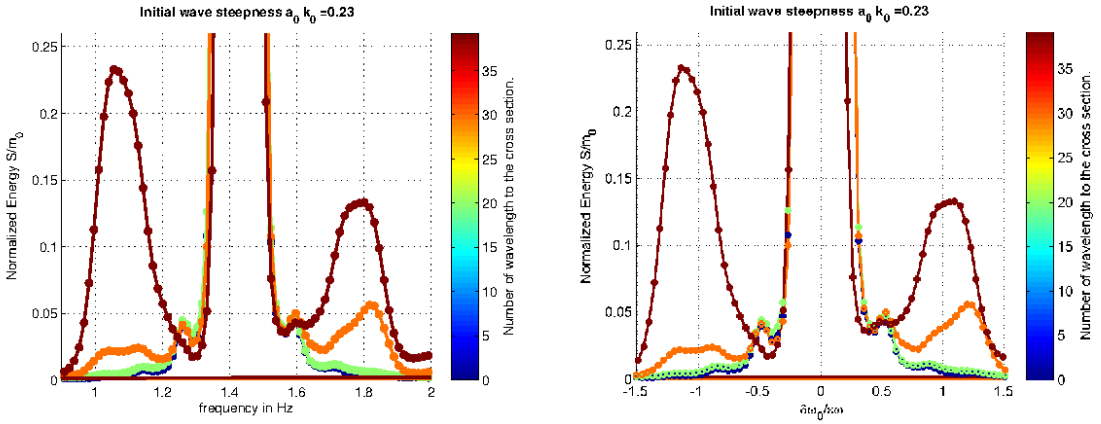

(a) Frequency in Hz. (b) Nondimentional frequency.

Figure B.2: Wave spectrum calculated at WP1, WP9, WP17 and the average of the CS2

The higher frequency of the sideband $f_+ = 1.79Hz(0.56s)$ and lower $f_- = 1.06Hz(0.94s)$. The carrier frequency was $f_0 = 1/0.7s = 1.43Hz$, so the condition $2f_0 = f_+ + f_-$ is satisfied: $2 * 1.43 = 2.86$ and $f_+ + f_- = 1.79 + 1.06 = 2.85$.

The wavelet of the time series of the central wave probe of the CS2 was also calculated and presented in the figure B.3.

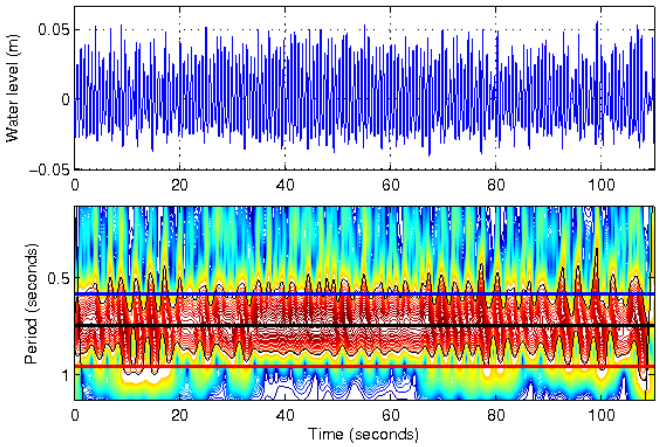

Figure B.3: Wavelet calculated ate the central wave probe at CS2: WP25.

B.2 Wave 6

The initial wave steepness (calculated on the wave probe 1) $ak = 0.27$, where the wave period $T_0 = 0.7s$, and $a_0 \approx 0.035m$.

The spectrum of the wave time series above is shown on figure B.5. The red spectra was averaged on the WPs at the CS2, distant $39L_0$ to the wavemaker, the

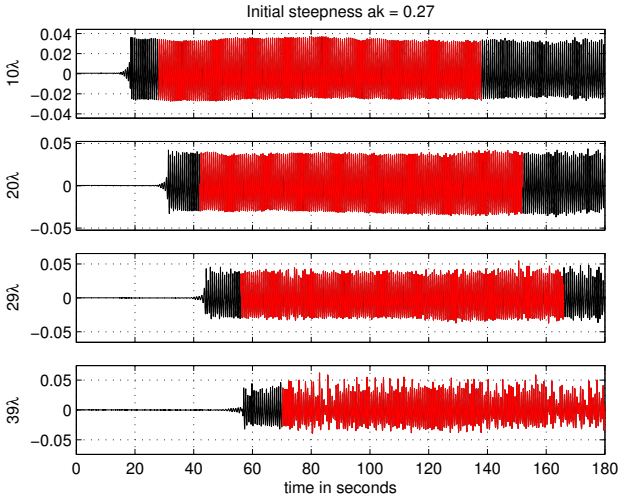

Figure B.4: Time series of the wave elevation at wave probes: 1, 9, 17 and 25. Red segment was used on the calculations.

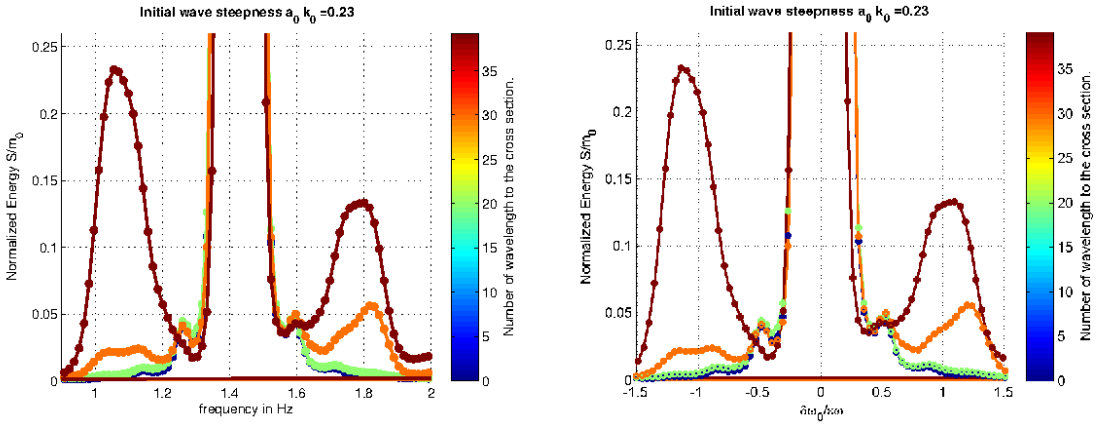

(a) Frequency in Hz.

(b) Nondimentional frequency.

Figure B.5: Wave spectrum calculated at WP1, WP9, WP17 and the average of the CS2

orange was from WP 17, and for this case at $29L_0$ of distance, the light blue at WP9 ($20L_0$) and the dark blue at WP1 ($10L_0$).

The higher frequency of the sideband $f_+ = 1.75Hz(0.57s)$ and lower $f_- = 1.11Hz(0.91s)$. The carrier frequency was $f_0 = 1/0.7s = 1.43Hz$, so the condition $2f_0 = f_+ + f_-$ is satisfied: $2 * 1.43 = 2.86$ and $f_+ + f_- = 1.75 + 1.11 = 2.86$. In nondimentional frequency $\hat{\delta}$, the values of the sidebands frequency are: $\omega_- = -0.84$ and $\omega_+ = 0.80$.

The wavelet of the time series of the central wave probe of the CS2 was also calculated and presented in the figure B.6.

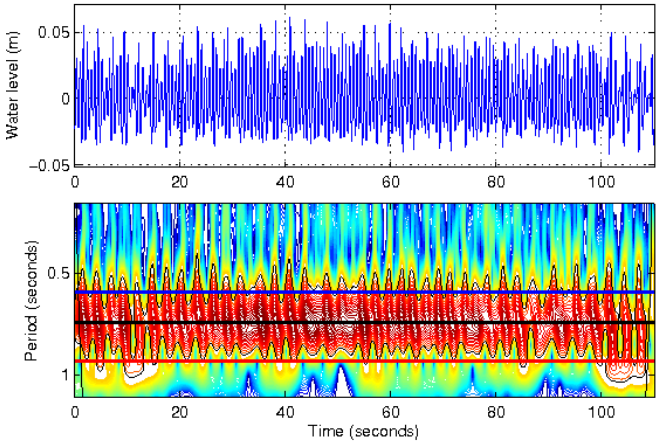

Figure B.6: Wavelet calculated ate the central wave probe at CS2: WP25.

B.3 Wave 22

The initial wave steepness (calculated on the wave probe 1) $ak = 0.34$, where the wave period $T_0 = 0.6s$, and $a_0 \approx 0.03m$.

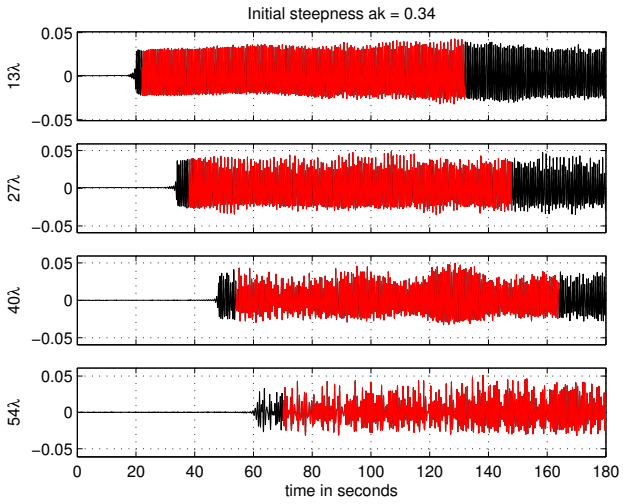

Figure B.7: Time series of the wave elevation at wave probes: 1, 9, 17 and 25. Red segment was used on the calculations.

The spectrum of the wave time series above is shown on figure B.8. The red spactra was relative to $54L_0$ from the wavemaker, the orange at WP 17 ($40L_0$) of distance, the light blue at WP9 ($27L_0$) and the dark blue at WP1 ($13L_0$).

The higher frequency of the sideband $f_+ = 2.14HzHz(0.46s)$ and lower $f_- = 1.20Hz(0.83s)$. The carrier frequency was $f_0 = 1/0.6s = 1.67Hz$, so the condition $2f_0 = f_+ + f_-$ is satisfied: $2 * 1.67 = 3.33$ and $f_+ + f_- = 2.14 + 1.20 = 3.34$. In

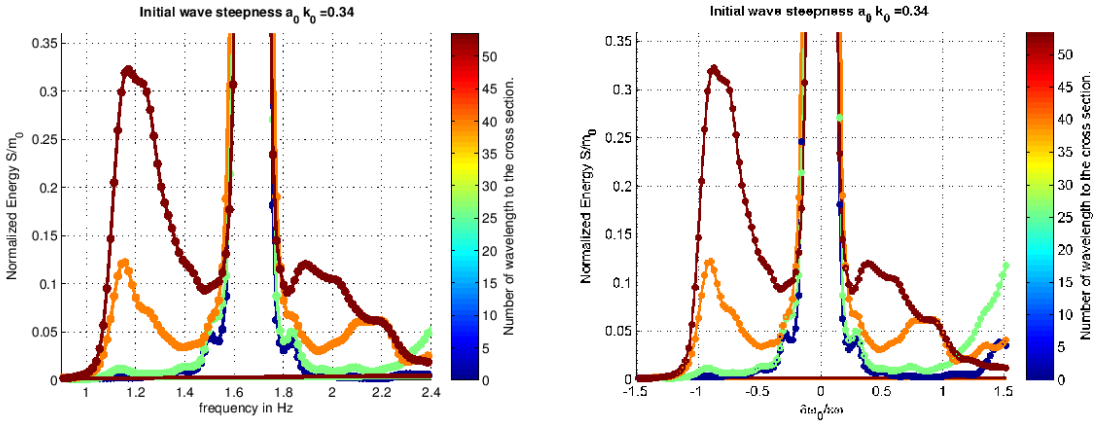

(a) Frequency in Hz. (b) Nondimentional frequency.

Figure B.8: Wave spectrum calculated at WP1, WP9, WP17 and the average of the CS2

nondimentional frequency $\hat{\delta}$, the values of the sidebands frequency are: $\omega_{-} = -0.87$ and $\omega_{+} = 0.91$.

The wavelet of the time series of the central wave probe of the CS2 was also calculated and presented in the figure B.9.

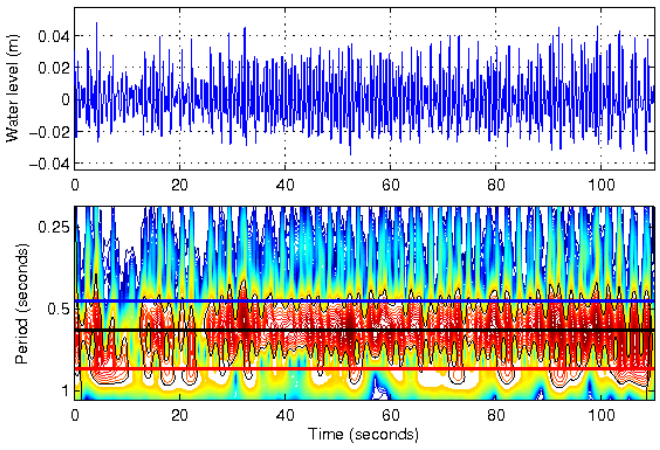

Figure B.9: Wavelet calculated ate the central wave probe at CS2: WP25.

B.4 Wave 23

The initial wave steepness (calculated on the wave probe 1) $ak = 0.23$, where the wave period $T_0 = 0.7s$, and $a_0 \approx 0.029m$. The time series for the analysis with 100 seconds (from the total of 180s):

The spectrum of the wave time series above is shown on figure B.11. The red

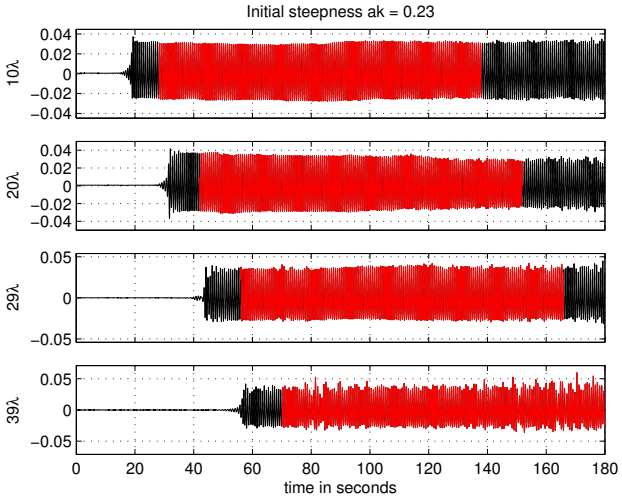

Figure B.10: Time series of the wave elevation at wave probes: 1, 9, 17 and 25. Red segment was used on the calculations.

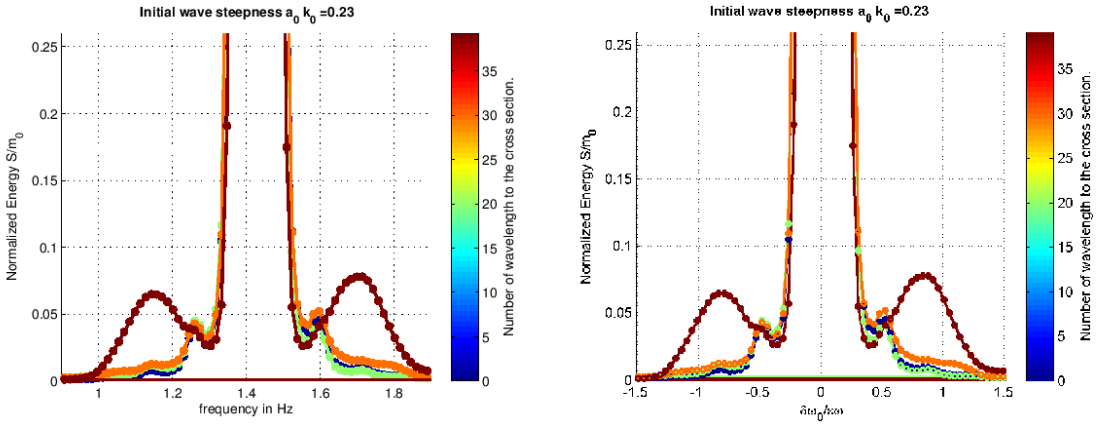

(a) Frequency in Hz.

(b) Nondimentional frequency.

Figure B.11: Wave spectrum calculated at WP1, WP9, WP17 and the average of the CS2

spectra was relative to $39L_0$ from the wavemaker, the orange at WP 17 ($29L_0$) of distance, the light blue at WP9 ($20L_0$) and the dark blue at WP1 ($10L_0$).

The higher frequency of the sideband $f_+ = 1.71Hz(0.57s)$ and lower $f_- = 1.15Hz(0.9s)$. The carrier frequency was $f_0 = 1/0.7s = 1.43Hz$, so the condition $2f_0 = f_+ + f_-$ is satisfied: $2 * 1.43 = 2.86$ and $f_+ + f_- = 1.71 + 1.15 = 2.86$. In nondimentional frequency $\hat{\delta}$, the values of the sidebands frequency are: $\omega_- = -0.74$ and $\omega_+ = 0.75$.

The wavelet of the time series of the central wave probe of the CS2 was also calculated and presented in the figure B.12.

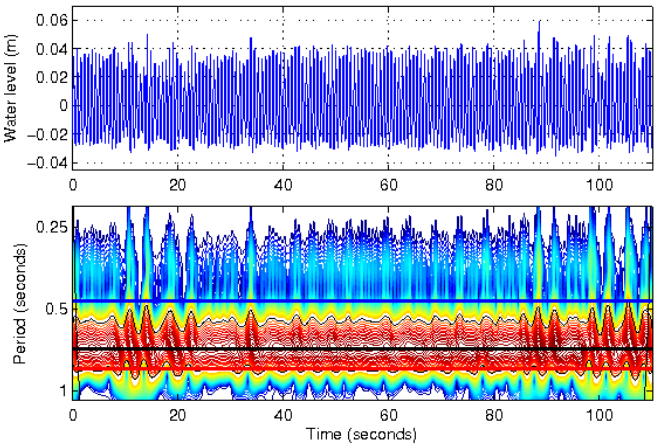

Figure B.12: Wavelet calculated ate the central wave probe at CS2: WP25.

B.5 Wave 25

The initial wave steepness (calculated on the wave probe 1) $ak = 0.26$, where the wave period $T_0 = 0.8s$, and $a_0 \approx 0.042m$.

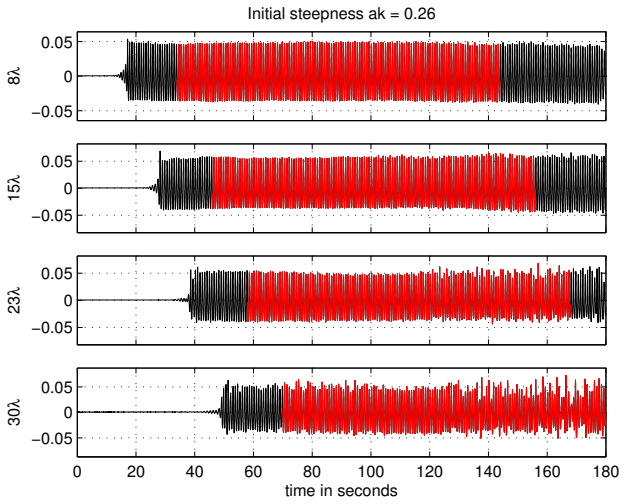

Figure B.13: Time series of the wave elevation at wave probes: 1, 9, 17 and 25. Red segment was used on the calculations.

The spectrum of the wave time series above is shown on figure B.14. The red spectra was relative to $30L_0$ from the wavemaker, the orange at WP 17 ($23L_0$) of distance, the light blue at WP9 ($15L_0$) and the dark blue at WP1 ($8L_0$).

The higher frequency of the sideband $f_+ = 1.55Hz(0.64s)$ and lower $f_- = 0.94Hz(1.06s)$. The carrier frequency was $f_0 = 1/0.8s = 1.25Hz$, so the condition $2f_0 = f_+ + f_-$ is satisfied: $2 * 1.25 = 2.50$ and $f_+ + f_- = 1.55 + 0.94 = 2.49$. In

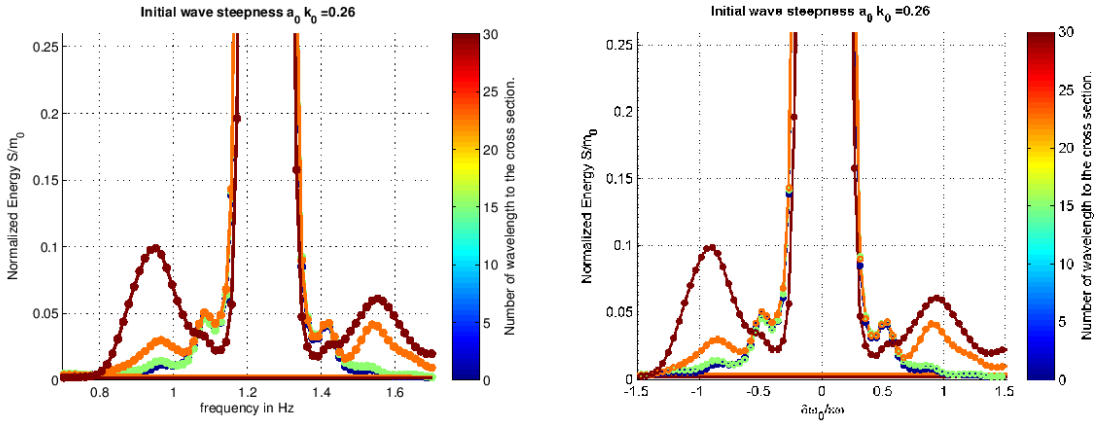

(a) Frequency in Hz. (b) Nondimentional frequency.

Figure B.14: Wave spectrum calculated at WP1, WP9, WP17 and the average of the CS2

nondimentional frequency $\hat{\delta}$, the values of the sidebands frequency are: $\omega_{-} = -0.79$ and $\omega_{+} = 0.80$.

The wavelet of the time series of the central wave probe of the CS2 was also calculated and presented in the figure B.15.

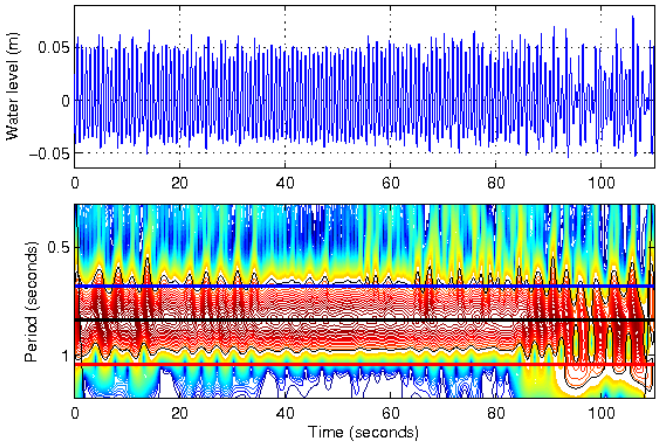

Figure B.15: Wavelet calculated ate the central wave probe at CS2: WP25.

B.6 Wave 26

The initial wave steepness (calculated on the wave probe 1) $ak = 0.26$, where the wave period $T_0 = 0.8s$, and $a_0 \approx 0.042m$.

The spectrum of the wave time series above is shown on figure B.14. The red spectra was relative to $30L_0$ from the wavemaker, the orange at WP 17 ($23L_0$) of distance, the light blue at WP9 ($15L_0$) and the dark blue at WP1 ($8L_0$).

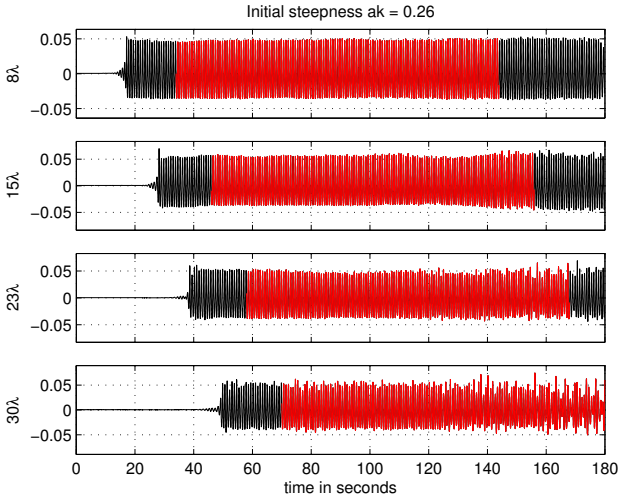

Figure B.16: Time series of the wave elevation at wave probes: 1, 9, 17 and 25. Red segment was used on the calculations.

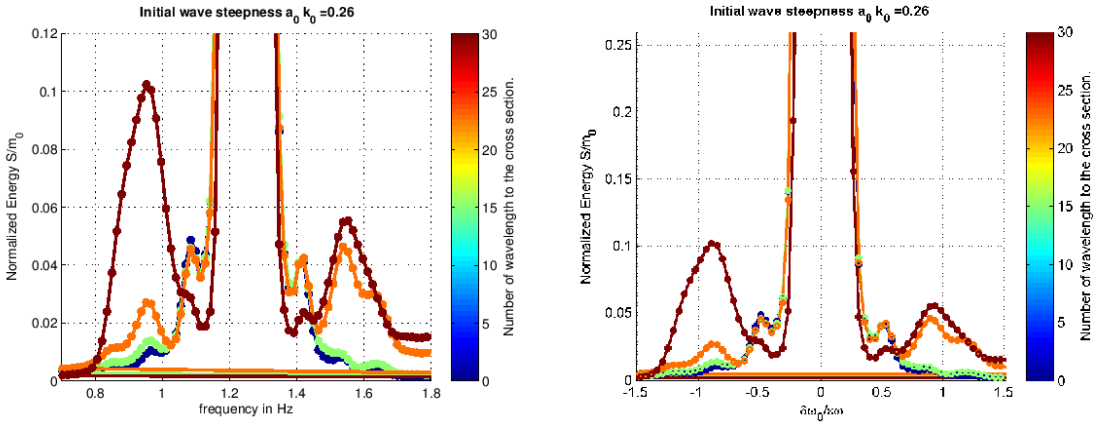

(a) Frequency in Hz.

(b) Nondimentional frequency.

Figure B.17: Wave spectrum calculated at WP1, WP9, WP17 and the average of the CS2

The higher frequency of the sideband $f_+ = 1.55Hz(0.64s)$ and lower $f_- = 0.95Hz(1.06s)$. The carrier frequency was $f_0 = 1/0.8s = 1.25Hz$, so the condition $2f_0 = f_+ + f_-$ is satisfied: $2 * 1.25 = 2.50$ and $f_+ + f_- = 1.55 + 0.95 = 2.50$. In nondimentional frequency $\hat{\delta}$, the values of the sidebands frequency are: $\omega_- = -0.89$ and $\omega_+ = 0.93$.

The wavelet of the time series of the central wave probe of the CS2 was also calculated and presented in the figure B.18.

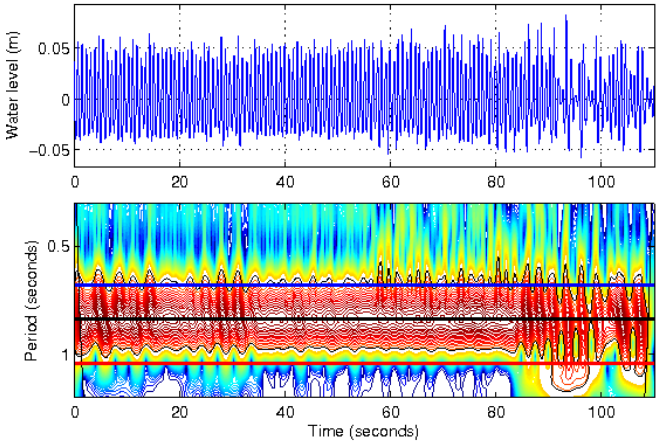

Figure B.18: Wavelet calculated ate the central wave probe at CS2: WP25.

B.7 Wave 39

The initial wave steepness (calculated on the wave probe 1) $ak = 0.28$, where the wave period $T_0 = 0.7s$, and $a_0 \approx 0.034m$.

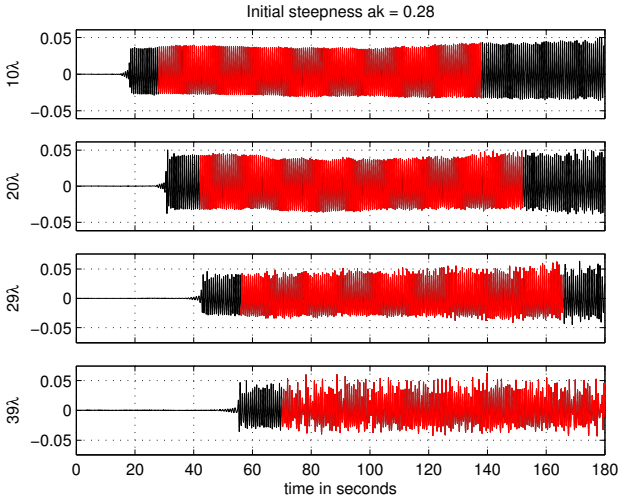

Figure B.19: Time series of the wave elevation at wave probes: 1, 9, 17 and 25. Red segment was used on the calculations.

The spectrum of the wave time series above is shown on figure B.20. The red spectra was relative to $39L_0$ from the wavemaker, the orange at WP 17 ($29L_0$) of distance, the light blue at WP9 ($20L_0$) and the dark blue at WP1 ($10L_0$).

The higher frequency of the sideband $f_+ = 1.77Hz(0.56s)$ and lower $f_- = 1.08Hz(0.93s)$. The carrier frequency was $f_0 = 1/0.7s = 1.43Hz$, so the condition $2f_0 = f_+ + f_-$ is satisfied: $2 * 1.43 = 2.86$ and $f_+ + f_- = 1.77 + 1.08 = 2.85$. In

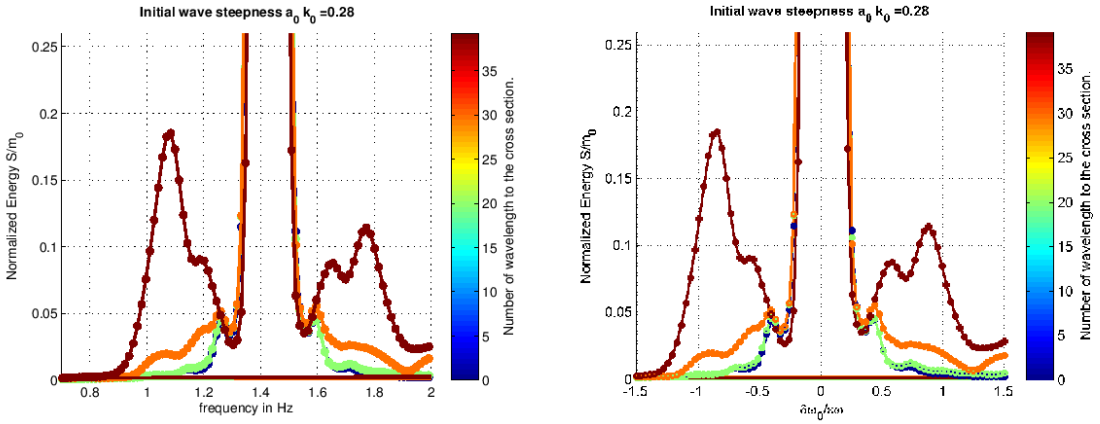

(a) Frequency in Hz. (b) Nondimentional frequency.

Figure B.20: Wave spectrum calculated at WP1, WP9, WP17 and the average of the CS2

nondimentional frequency $\hat{\delta}$, the values of the sidebands frequency are: $\omega_- = -0.78$ and $\omega_+ = 0.79$.

The inside peak are at 1.19Hz and 1.66Hz and also sum 2.85 and also satisfy the condition of $2\omega_0 = \omega_- + \omega_+$.

The wavelet of the time series of the central wave probe of the CS2 was also calculated and presented in the figure B.21.

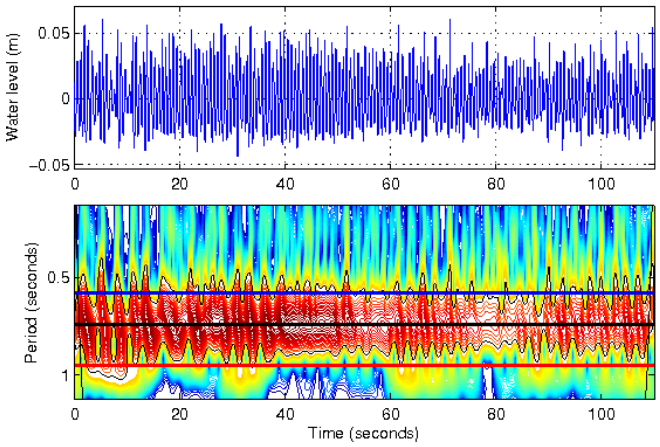

Figure B.21: Wavelet calculated ate the central wave probe at CS2: WP25.

B.8 Wave 41

The initial wave steepness (calculated on the wave probe 1) $ak = 0.29$, where the wave period $T_0 = 0.8s$, and $a_0 \approx 0.047m$.

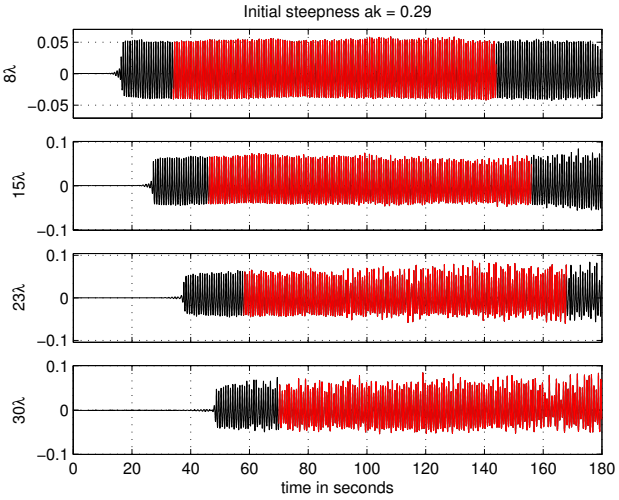

Figure B.22: Time series of the wave elevation at wave probes: 1, 9, 17 and 25. Red segment was used on the calculations.

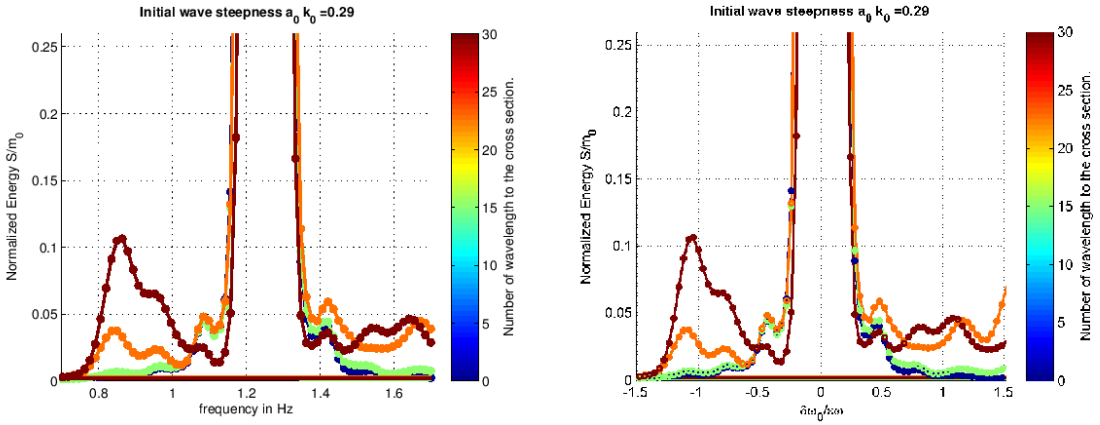

(a) Frequency in Hz.

(b) Nondimentional frequency.

Figure B.23: Wave spectrum calculated at WP1, WP9, WP17 and the average of the CS2

The spectrum of the wave time series above is shown on figure B.23. The red spectra was relative to $30L_0$ from the wavemaker, the orange at WP 17 ($23L_0$) of distance, the light blue at WP9 ($15L_0$) and the dark blue at WP1 ($8L_0$).

The higher frequency of the sideband $f_+ = 1.64Hz(0.61s)$ and lower $f_- = 0.86Hz(1.16s)$. The carrier frequency was $f_0 = 1/0.8s = 1.25Hz$, so the condition $2f_0 = f_+ + f_-$ is satisfied: $2 * 1.25 = 2.50$ and $f_+ + f_- = 1.64 + 0.86 = 2.50$. In nondimentional frequency $\hat{\delta}$, the values of the sidebands frequency are: $\omega_- = -0.91$ and $\omega_+ = 0.92$.

The inside peak are at 0.95Hz + 1.55Hz and also sum 2.85 and also satisfy the condition of $2\omega_0 = \omega_- + \omega_+$. The nondimentional frequencies closer to the carrier peak are -0.68 and +0.68.

The wavelet of the time series of the central wave probe of the CS2 was also calculated and presented in the figure B.24.

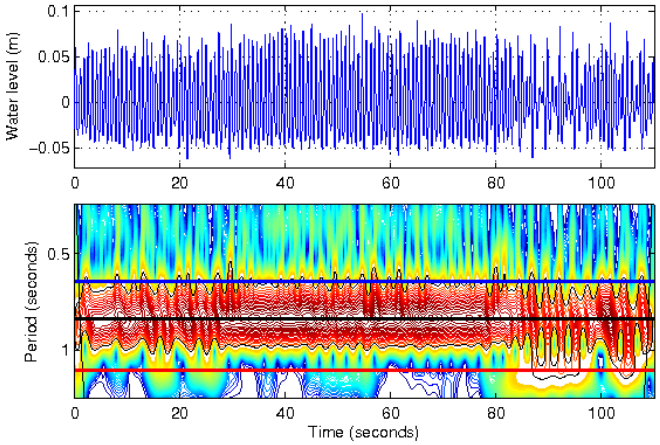

Figure B.24: Wavelet calculated ate the central wave probe at CS2: WP25.

B.9 Wave 42

The initial wave steepness (calculated on the wave probe 1) $ak = 0.29$, where the wave period $T_0 = 0.8s$, and $a_0 \approx 0.047m$.

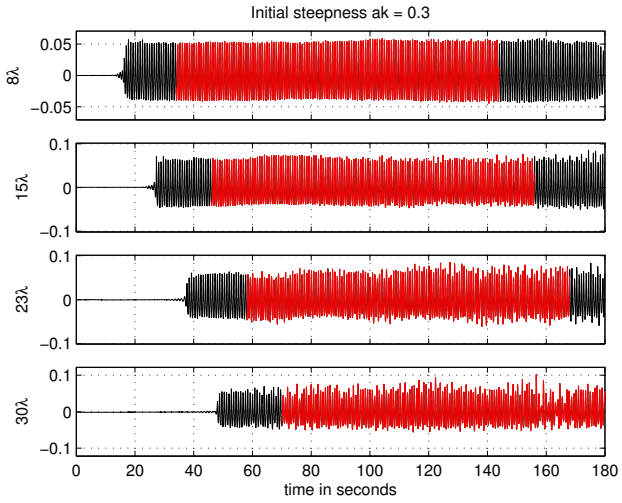

Figure B.25: Time series of the wave elevation at wave probes: 1, 9, 17 and 25. Red segment was used on the calculations.

The spectrum of the wave time series above is shown on figure B.26. The red spectra was relative to $30L_0$ from the wavemaker, the orange at WP 17 ($23L_0$) of distance, the light blue at WP9 ($15L_0$) and the dark blue at WP1 ($8L_0$).

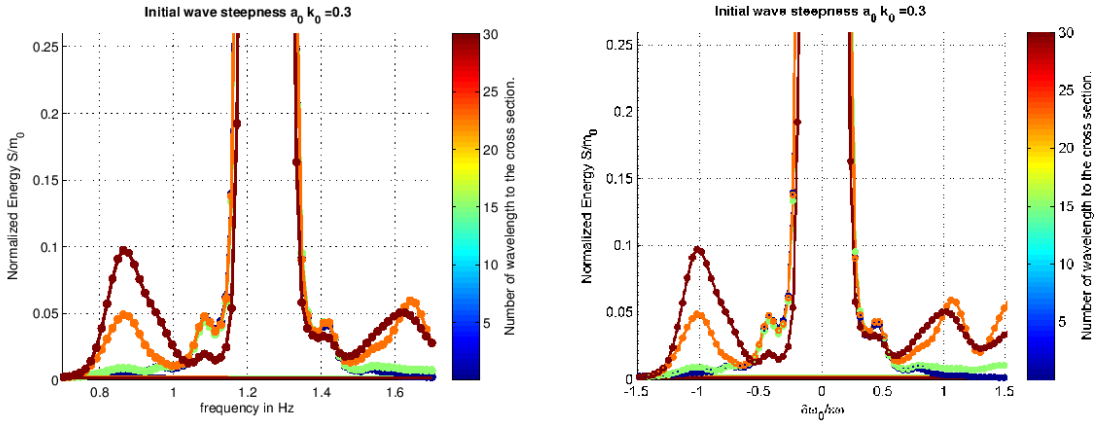

(a) Frequency in Hz. (b) Nondimentional frequency.

Figure B.26: Wave spectrum calculated at WP1, WP9, WP17 and the average of the CS2

The higher frequency of the sideband $f_+ = 1.64Hz(0.61s)$ and lower $f_- = 0.86Hz(1.16s)$. The carrier frequency was $f_0 = 1/0.8s = 1.25Hz$, so the condition $2f_0 = f_+ + f_-$ is satisfied: $2 * 1.25 = 2.50$ and $f_+ + f_- = 1.64 + 0.86 = 2.50$. In nondimentional frequency $\hat{\delta}$, the values of the sidebands frequency are: $\omega_- = -0.91$ and $\omega_+ = 0.92$.

The inside peak are at 0.95Hz + 1.55Hz and also sum 2.85 and also satisfy the condition of $2\omega_0 = \omega_- + \omega_+$. The nondimentional frequencies closer to the carrier peak are -0.68 and +0.68.

The wavelet of the time series of the central wave probe of the CS2 was also calculated and presented in the figure B.27.

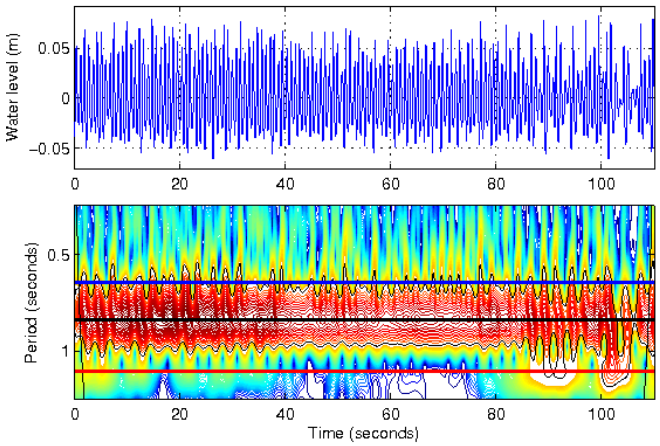

Figure B.27: Wavelet calculated ate the central wave probe at CS2: WP25.

Appendix C

Spatial analysis program: Specf.m

```
function S = Spectf(x,y,dt,Nfa,a0)
%        S = SPECTf(x,dt,Nfa)
%        S = SPECTf(x,y,dt,Nfa)   cross spectrum
%
% Frequency averaged power spectrum estimate,  GEOPHYSICAL ...
    NORMALIZATION
% Trend is removed, Blackman-Harris window is used. K.K.Kahma ...
    1990-05-19
%
%     x , y  = data vectors
%     dt = sampling interval in seconds
%     Nfa = number of elementary frequency bands which are averaged
%
%     S(:,1) = f      (1/second == Hz)
%     S(:,2) = Sxx    (unit*unit*second)
%
% If cross spectrum is calculated
%     S(:,3) = Syy
%     S(:,4) = Sxy
%     S(:,5) = phase angle = 180/pi*atan2(-imag(Sxy),real(Sxy))
%     S(:,6) = coherence   = abs(Sxy./sqrt(Sxx.*Syy))
%
%     positive phase means x leads y

%        S = SPECTF(x,y,dt,Nfa,a0)
% Elementary frequency bands 0:a0-1 (matlab index 1:a0) are ignored.
% Default a0 is 0, i.e. all bands including zero (mean value) ...
    are incuded.
%

x = x(:).';          % Make sure x is a row vector
N  = max(size(x));      % Number of data points
```

```
30 window=Blackhar(N).';
31
32 if max(size(y)) ~= N,
33    if (max(size(y)) == 1) | (nargin < 5)
34
35 % ***************
36    % Spectrum
37 % ***************
38
39    if (nargin < 4), Nfa = 0; end    % default a0
40    if (nargin < 3), dt = 31; end    % default Nfa
41    a0 = Nfa; Nfa = dt; dt = y;
42
43    Nfft=0; maxb=0; C=0; df=0;          % To define these ...
          variables before Xx
44    Xx = fft(window.*detrend(x));
45    Nfft = length(Xx);                  % Number of points in FFT
46    maxb = floor(Nfft/2+1);
47    Xx(maxb+1:Nfft)=[];
48    Xx(maxb) = Xx(maxb)/2;
49
50    C = dt/(Nfa*pi*norm(window)^2);     % Scaling coefficient
51    df = 2*pi/(dt*Nfft);
52
53    if Nfa==1
54       f = [a0:maxb-1]*df;
55       Pxx = (abs(Xx(a0+1:maxb)).^2)*C;
56    else
57       if Nfa > 20
58 %       When Nfa is large enough this is as fast as vectorized
59 %       averaging and it requires far less memory
60          m=0; a=a0+1; b=a0+Nfa;
61          while b <= maxb
62             m=m+1;
63             Pxx(m) = sum(abs(Xx(a:b)).^2)*C;
64             f(m) = df*((a+b-2)/2);
65             a=a+Nfa; b=b+Nfa;
66          end
67       else
68          m=fix((maxb-a0) / Nfa);
69          f=([1:m]*Nfa+(a0-0.5-Nfa/2))*df;
70          b=a0+m*Nfa;
71
72 %         Old bin averaging loop
73 %         sx=zeros(m,Nfa);
74 %         for i=1:Nfa
75 %            sx(:,i) = abs(Xx(a0+i:Nfa:b)).^2;
```

```
76 %         end
77 %         Pxx=(sum(sx.')*C);
78
79          sx=zeros(Nfa,m);
80          sx(:) = abs(Xx(a0+1:b)).^2;
81          Pxx=(sum(sx)*C);
82        end
83        a=a0+1+m*Nfa;
84        if a ≤ maxb
85           m=m+1;
86           c = maxb+1-a;
87           Pxx(m) = sum(abs(Xx(a:maxb)).^2)*C*Nfa/c;
88           f(m) = df*(a+maxb-2)/2;
89        end
90      end
91      clear Xx window
92      S = [f/2/pi;2*pi*Pxx].';
93
94    else
95
96    error('x and y are not of same size'); end
97
98  else
99
100 % **********************
101    % Cross spectrum
102 % **********************
103
104    if (nargin < 5), a0 = 0; end    % default a0
105    if (nargin < 4), Nfa = 31; end  % default Nfa
106
107    y = y(:).';
108    Nfft=0; maxb=0; C=0; df=0;
109    Xx = fft(window.*detrend(x));
110    Nfft = length(Xx);                  % Number of points in FFT
111    maxb = floor(Nfft/2+1);
112
113    Xx(maxb+1:Nfft)=[];
114    Xx(maxb) = Xx(maxb)/2;
115
116    C = dt/(Nfa*pi*norm(window)^2);     % Scaling coefficient
117    df = 2*pi/(dt*Nfft);
118
119    Yy = fft(window.*detrend(y));
120    Yy(maxb) = Yy(maxb)/2;
121    Yy(maxb+1:Nfft)=[];
122
```

```
123     if Nfa==1
124        f = [a0:maxb-1]*df;
125        Pxx = (abs(Xx(a0+1:maxb)).^2)*C;
126        Pyy = (abs(Yy(a0+1:maxb)).^2)*C;
127        Pxy = (conj(Xx(a0+1:maxb)).*Yy(a0+1:maxb))*C;
128     else
129        if Nfa > 20
130           m=0; a=a0+1; b=a0+Nfa;
131           while b ≤ maxb
132              m=m+1;
133              Pxx(m) = sum(abs(Xx(a:b)).^2)*C;
134              Pyy(m) = sum(abs(Yy(a:b)).^2)*C;
135              Pxy(m) = sum(conj(Xx(a:b)).*Yy(a:b))*C;
136              f(m) = df*((a+b-2)/2);
137              a=a+Nfa; b=b+Nfa;
138           end
139        else
140           m=fix((maxb-a0) / Nfa);
141           f=([1:m]*Nfa+(a0-0.5-Nfa/2))*df;
142           b=a0+m*Nfa;
143  %         sx=zeros(m,Nfa);
144  %         for i=1:Nfa
145  %            sx(:,i)  = abs(Xx(a0+i:Nfa:b)).^2;
146  %            sy(:,i)  = abs(Yy(a0+i:Nfa:b)).^2;
147  %            sxy(:,i) = conj(Xx(a0+i:Nfa:b)).*Yy(a0+i:Nfa:b);
148  %         end
149           sx=zeros(Nfa,m);
150           sx(:) = abs(Xx(a0+1:b)).^2;
151           Pxx=(sum(sx)*C);
152           sx(:) = abs(Yy(a0+1:b)).^2;
153           Pyy=(sum(sx)*C);
154           sx(:) = conj(Xx(a0+1:b)).*Yy(a0+1:b);
155           Pxy=(sum(sx)*C);
156           a=a0+1+m*Nfa;
157        end
158
159        if a ≤ maxb
160           m=m+1;
161           c = maxb+1-a;
162           Pxx(m) = sum(abs(Xx(a:maxb)).^2)*C*Nfa/c;
163           Pyy(m) = sum(abs(Yy(a:maxb)).^2)*C*Nfa/c;
164           Pxy(m) = sum(conj(Xx(a:maxb)).*Yy(a:maxb))*C*Nfa/c;
165           f(m) = df*(a+maxb-2)/2;
166        end
167     end
168     phase = 180/pi*atan2(-imag(Pxy),real(Pxy));
169     coh   = abs(Pxy./sqrt(Pxx.*Pyy));
```

```
170     clear Xx Yy window sx sy sxy
171     S = [f/2/pi;2*pi*Pxx;2*pi*Pyy;2*pi*Pxy;phase;coh].';
172 end
```